

9-14-2017

# Luminescence in Lithium Borates

Brant T. Kananen

Follow this and additional works at: <https://scholar.afit.edu/etd>

 Part of the [Atomic, Molecular and Optical Physics Commons](#)

---

## Recommended Citation

Kananen, Brant T., "Luminescence in Lithium Borates" (2017). *Theses and Dissertations*. 773.  
<https://scholar.afit.edu/etd/773>

This Dissertation is brought to you for free and open access by the Student Graduate Works at AFIT Scholar. It has been accepted for inclusion in Theses and Dissertations by an authorized administrator of AFIT Scholar. For more information, please contact [richard.mansfield@afit.edu](mailto:richard.mansfield@afit.edu).



**THREE-DIMENSIONAL IMAGING OF COLD  
ATOMS IN A MAGNETO-OPTICAL TRAP  
WITH A LIGHT FIELD MICROSCOPE**

DISSERTATION

Gordon E. Lott, Captain, USAF

AFIT-ENP-DS-17-S-029

**DEPARTMENT OF THE AIR FORCE  
AIR UNIVERSITY**

**AIR FORCE INSTITUTE OF TECHNOLOGY**

**Wright-Patterson Air Force Base, Ohio**

**DISTRIBUTION STATEMENT A.  
APPROVED FOR PUBLIC RELEASE; DISTRIBUTION UNLIMITED**

The views expressed in this document are those of the author and do not reflect the official policy or position of the United States Air Force, the United States Department of Defense or the United States Government. This material is declared a work of the U.S. Government and is not subject to copyright protection in the United States.

AFIT-ENP-DS-17-S-029

THREE-DIMENSIONAL IMAGING OF COLD ATOMS IN A  
MAGNETO-OPTICAL TRAP WITH A LIGHT FIELD MICROSCOPE

DISSERTATION

Presented to the Faculty  
Graduate School of Engineering and Management  
Air Force Institute of Technology  
Air University  
Air Education and Training Command  
in Partial Fulfillment of the Requirements for the  
Degree of Doctorate of Philosophy

Gordon E. Lott, BS, MS  
Captain, USAF

September 2017

**DISTRIBUTION STATEMENT A.**  
APPROVED FOR PUBLIC RELEASE; DISTRIBUTION UNLIMITED

AFIT-ENP-DS-17-S-029

THREE-DIMENSIONAL IMAGING OF COLD ATOMS IN A  
MAGNETO-OPTICAL TRAP WITH A LIGHT FIELD MICROSCOPE

DISSERTATION

Gordon E. Lott, BS, MS  
Captain, USAF

Committee Membership:

Michael A. Marciniak, PhD  
Chair

John H. Burke, PhD  
Member

Michael R. Hawks, PhD  
Member

Matthew C. Fickus, PhD  
Member

Adedeji B. Badiru, PhD  
Dean, Graduate School of Engineering and Management

## Abstract

Imaging of trapped atoms in three dimensions utilizing a light field microscope is demonstrated in this work. Such a system is of interest in the development of atom interferometer accelerometers in dynamic systems where strictly defined focal planes may be impractical. A light field microscope was constructed utilizing a Lytro® Development Kit micro-lens array and sensor. It was used to image fluorescing rubidium atoms in a magneto-optical trap. The three-dimensional (3D) volume of the atoms is reconstructed using a modeled point spread function (PSF), taking into consideration the low magnification (1.25) of the system which changed typical assumptions in the optics model for the PSF. The 3D reconstruction is analyzed with respect to a standard off-axis fluorescence image. Optical axis separation between two atom clouds is measured to a  $100\mu\text{m}$  accuracy in a 3mm deep volume, with a  $16\mu\text{m}$  in-focus standard resolution and a 3.9mm by 3.9mm field of view. Optical axis spreading is observed in the reconstruction and discussed. Absorption imaging with the light field microscope is analyzed and a method devised to collect the information necessary to create 3D images as in the fluorescing case. This 3D information can be used to determine properties of the atom cloud with a single camera and single atom image, and can be applied anywhere 3D information is needed but optical access may be limited.

## Acknowledgements

I would first of all like to thank Dr. Marciniak for the guidance and wisdom he has imparted over the course of this work, and for taking me on as a student with a project out side of his own work. I must thank Dr. Burke for his own guidance and wisdom while acting effectively as a co-advisor on this dissertation, for taking me on as a student, and providing the basis for this dissertation as well as the resources that made it possible. I want to thank Dr. Hawks and Dr. Fickus for adding their insight and knowledge to this work. I also want to thank Lt Col Franz and Maj Hallada for their lab help.

I have had the privilege of working here at AFIT and at AFRL/RVBY in New Mexico. At AFIT I would like to acknowledge Lt Col Lane, Maj Burley, Maj Emmons, and Capt Haluska. I want to acknowledge all the NM lab folks who made working there great. Ben, Brian, Eric, Gretchen, Jordan, Josh, Kyle, Matt B., Matt S., Maxwell, Mayer, Mike, Nathan, Robbie, Rudy, Spencer, and Stacy. To my excellent roommates in New Mexico, Peter, Seth, and Gerry, thanks for being friends and connecting me to a New Mexico community.

To Daniel, Sam and Mark. I am grateful that you have been good friends, but also good brothers. Thanks.

I thank God for giving me all of the above and the following and continually being with me and loving me in every step of this endeavor.

Gordon E. Lott

# Table of Contents

	Page
Abstract .....	iv
Acknowledgements .....	v
List of Figures .....	viii
List of Tables .....	xi
I. Introduction .....	1
1.1 Motivation .....	2
1.1.1 Atom Interferometry for Inertial Navigation .....	2
1.1.2 Limited Optical Access .....	5
1.2 This Dissertation .....	7
1.2.1 Outline .....	9
II. Trapping and Cooling Atoms .....	10
2.1 Doppler Cooling and Optical Molasses .....	11
2.2 Magneto-Optical Traps .....	14
2.3 The Experiment's Magneto-Optical Trap .....	19
III. Light Field Imaging .....	27
3.1 Previous Work .....	27
3.2 The Plenoptic Function and Light Field Imaging .....	29
3.3 Wave Front Sensing .....	36
3.4 Light Field Microscopy .....	38
3.4.1 Resolution and Axial Resolution .....	39
3.4.2 The Point Spread Function and Deconvolution .....	42
IV. Three Dimensional Fluorescence Imaging of Trapped Cold Atoms with a Light Field Microscope .....	53
4.1 The Light Field Microscope .....	54
4.2 Image Collection and Calibration .....	58
4.3 3D Reconstructions .....	61
4.3.1 Optical Axis Spreading from Back Projection .....	66
4.3.2 Back Projection Spreading Comparison to $NA = 0.14$ Objective and Modeled Ellipse .....	74
4.4 Error .....	75
4.4.1 Impact of Using the Lytro Development Kit Sensor .....	79

	Page
4.5 Phase Term Effects on the 3D Volume .....	80
4.6 Shifting the Focal Plane of the LFM .....	83
4.7 Optical System Trade Offs .....	87
4.8 Atom Number Measurements .....	91
V. Absorption and Off-Resonance Imaging .....	93
5.1 Absorption and Off-Resonance Imaging Theory .....	93
5.1.1 Absorption Imaging with the Light Field Microscope .....	94
5.2 Off-Resonance Imaging .....	97
5.2.1 Off-Resonance Imaging with the Light Field Microscope .....	98
5.3 Toward 3D Absorption Imaging .....	103
VI. Conclusion .....	107
6.1 Future Work .....	108
Appendix A. Tomography and Back Projection .....	111
Appendix B. Bose-Einstein Condensate Distributions .....	115
Appendix C. MOT Image Collection .....	117
3.1 MOT One .....	117
3.2 MOT Two .....	119
3.3 MOT Three .....	121
Bibliography .....	123

## List of Figures

Figure		Page
1	Atom Interferometer Diagram .....	4
2	Example Cold Atom Interferometer System .....	7
3	One-Dimensional Optical Molasses Forces .....	13
4	Magneto-Optical Trap Energy Level Diagram.....	15
5	Magneto-Optical Trap Diagram.....	16
6	Rubidium 87 D <sub>2</sub> Energy Levels .....	21
7	Magneto-Optical Trap Experimental Set-Up.....	24
8	Image of Magneto-Optical Trap.....	25
9	Magneto-Optical Trap Experimental Set-Up Side View .....	26
10	Ray Trace of the Traditional Plenoptic Camera .....	29
11	The Plenoptic Function's Radiance Geometry .....	30
12	Plenoptic Imaging Geometry for Depth Determination .....	34
13	Light Field Microscope Optics Ray Trace .....	39
14	Light Field Microscope Projection Ray Trace .....	40
15	Object, Image, and Lens Coordinates.....	46
16	The 0.26 NA Objective Light Field Microscope .....	55
17	Plenoptic Image of MOT One .....	61
18	Surface Contour of Deconvolved Volume of MOT One .....	62
19	Plenoptic and Reference Camera Orientations .....	63
20	Scaled Projection and Reference Images of MOT One.....	64
21	Reconstruction Artifacts Example.....	67
22	Back Projection Triangle .....	68

Figure	Page
23	Two Dimensional Gaussian Fit Comparison ..... 70
24	MOT Three Gaussian Spreading ..... 71
25	Plenoptic Image with a 0.14 NA Objective Light Field Microscope ..... 72
26	Projected Deconvolution Results for 0.14 NA Objective ..... 73
27	Maximum Optical Axis Spreading With 0.14 NA Objective ..... 75
28	Reconstruction and Axial Spreading of an Ellipse ..... 76
29	Added Point Spread Function Phase Term Affect on Intensity at Sensor Plane ..... 81
30	Deconvolution Comparison of Added Point Spread Function Phase Term ..... 82
31	Shifted Focal Plane Reconstructions ..... 85
32	Shifted Focal Plane Position Plots ..... 86
33	Light Field Microscope Spot Size vs Magnification ..... 88
34	Light Field Microscope Resolution vs Micro-lens Diameter ..... 90
35	MOT Cloud 2D Density Distribution, Phase Shift and Slope ..... 101
36	BEC Cloud 2D Density Distribution, Phase Shift and Slope ..... 102
37	Absorption Imaging “PSF” ..... 105
38	Example of the Radon Transform ..... 112
39	Example of the Fourier Slice Theorem ..... 113
40	Plenoptic Image of MOT One ..... 117
41	Surface Contour of Deconvolved Volume of MOT One ..... 118
42	Scaled Projection and Reference Images of MOT One..... 118

Figure		Page
43	Plenoptic Image of MOT Two . . . . .	119
44	Surface Contour of Deconvolved Volume of MOT Two . . . . .	120
45	Scaled Projection and Reference Images of MOT Two . . . . .	120
46	Plenoptic Image of MOT Three . . . . .	121
47	Surface Contour of Deconvolved Volume of MOT Three . . . . .	122
48	Scaled Projection and Reference Images of MOT Three . . . . .	122

## List of Tables

Table		Page
1	Light Field Microscope Optical System Details .....	54
2	Measured Optical Axis Separation Between Two Atom Clouds .....	66
3	Calculated and Measured Optical Axis Spreading .....	71
4	Numerical Aperture Optical Stretching Factor and Magnification Resulting in $\approx 1\mu\text{m}$ Spot Sizes .....	87

# THREE-DIMENSIONAL IMAGING OF COLD ATOMS IN A MAGNETO-OPTICAL TRAP WITH A LIGHT FIELD MICROSCOPE

## I. Introduction

Laser cooled atoms and ultra-cold Bose-Einstein Condensates (BECs) are very versatile in their scientific uses and applications and continue to show potential for creating excellent sensors of magnetic fields, accelerations, and rotations [73, 17]. For instance, there have been measurements of accelerations better than  $10^{-10} \frac{m}{s^2}$  [29]. Along the same lines, cold atoms can be used for atomic clocks which are accurate to 1 second in over 100 million years [39]. Measuring these properties on a moving system can be used for inertial navigation [7, 62]. This is of interest to the Air Force Research Laboratory Space Vehicles Directorate (AFRL/RV). Improving clocks and inertial navigation systems are both useful in space systems. The Global Positioning System (GPS) constellation requires high accuracy clocks in order to provide accurate positioning information, and inertial navigation can be critical in times and places where GPS may be unavailable. The impressive capabilities of these cold atom systems have been demonstrated using large laboratory systems. Much work has now shifted to providing these capabilities in smaller systems [38, 62], so they can practically be used for inertial navigation and timing on mobile platforms such as satellites or airplanes. Creating such practical systems introduces some challenges at the basic level of observing the cold atom phenomenon of interest, which provide the desired measurement of the sensor. This research looks to solve two of these issues utilizing a light field or plenoptic imaging system.

## 1.1 Motivation

A current issue in making these systems mobile is the limitation on the dynamic range of imaging systems. When imaging atoms at high resolution, there is a very narrow depth of focus. For instance, a  $2\mu\text{m}$  resolution objective has a depth of focus of  $14\mu\text{m}$ . In order for a navigation system based on cold atom interferometry to work, there has to be room for the atoms to move in a small volume. If this volume is on a dynamic platform, the atoms can shift out of the focus of the imaging system. For instance if the atoms are experiencing an acceleration of  $1g$  for over  $1.7\text{ms}$  they will move more than  $14\mu\text{m}$ . Currently this is typically solved by passive detection of the fluorescence of the atoms with a photo-diode to simply count photons [66], despite its inaccuracies [61]. Additionally, the atoms occupy a three-dimensional (3D) space and can have information about the motion of the body in all three dimensions, but when detecting with a photo-diode, most of this information is lost.

### 1.1.1 Atom Interferometry for Inertial Navigation.

An atom interferometer accelerometer on a dynamic platform is the example system motivating this work. As the name implies, an atom interferometer utilizes interference of atom matter waves. De Broglie proposed that particles have a wavelength associated with them and behave as waves at that length scale [25]. Because of this, it is possible to interfere two atom waves, and so make a measurement using atom interferometry. In the case of a group of cold atoms, and particularly BECs, which are a coherent group of atoms, the atoms can be split into two groups, sent down two separate paths, and brought back together to interfere, just as in an optical interferometer. The control of atoms needed to perform this splitting and recombination is called atom optics and is a field of itself [1]. But a typical atom interferometer uses laser pulses at three different points to split, redirect and interfere the atoms,

just as an optical interferometer would use a beam splitter, mirrors and a second beam splitter to interfere the beams. Figure 1 gives a simple schematic of the atom's path. Cronin gives a much more detailed description of atom interferometers and their history in [19].

Having two, area-enclosing, interfering atomic paths, the Sagnac effect is used to measure the rotation of the interferometer [63]. The Sagnac effect gives the change in phase of two waves with respect to the rotation around the normal to the area enclosed by the interfering paths. The phase difference, is given by

$$\phi \approx \frac{4\pi \mathbf{A} \cdot \boldsymbol{\Omega}}{\lambda v}, \quad (1)$$

to first order with respect to  $\boldsymbol{\Omega}$ , where  $\boldsymbol{\Omega}$  is the rotation pseudovector pointing in the direction of the axis of rotation,  $\mathbf{A}$  is the area enclosed by the interferometer,  $\lambda$  is the wavelength and  $v$  is the speed of the wave. Using the de Broglie wavelength,  $\Lambda = h/p$ , which is Planck's constant divided by momentum, the phase difference becomes,

$$\phi \approx 4\pi \mathbf{A} \cdot \boldsymbol{\Omega} \frac{m}{h}, \quad (2)$$

where  $m$  is the mass of the atom being interfered. The significance of using atoms as apposed to photons can be seen if Equation (2) is divided by Equation (1), with Equation (1) describing the phase for an optical interferometer when  $v = c$ . This gives the ratio of an atomic interferometer phase difference to an optical interferometer phase difference. The result is [16]

$$\frac{mc^2}{h\nu} = \frac{c}{v_r} \sim 10^{10}, \quad (3)$$

where  $\nu = c/\lambda$  is the frequency of the light. The atom interferometer is more sensitive,

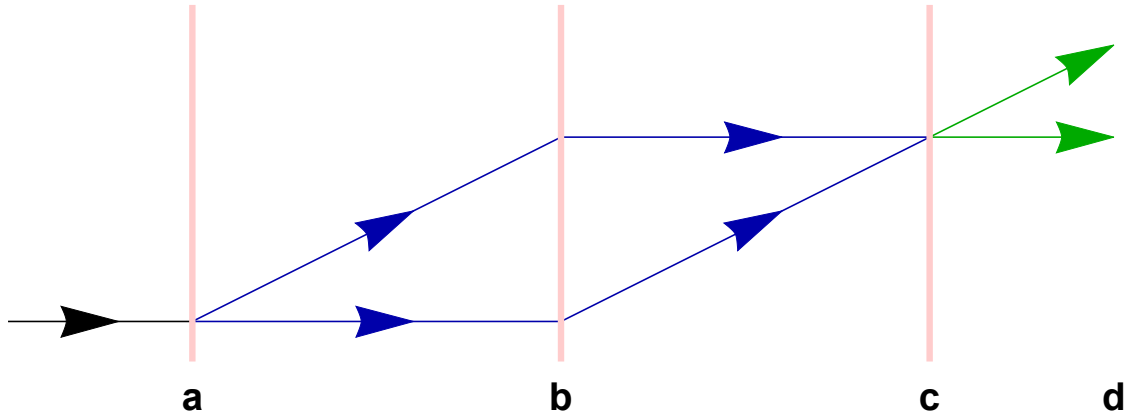


Figure 1. A schematic of the path atoms take in an atom interferometer. The atoms come in from the left with a certain initial velocity. At (a) a laser pulse splits the atoms into two packets by giving a vertical momentum kick to half. At (b) a second pulse directs them back together by applying the same kick to the other half. At (c) there is a recombination pulse. The atoms are measured at (d) by looking at how many atoms are in each packet following each of the green line paths on the far right.

due to the large rest mass of the atoms, and their slower speed,  $v_r$ . The increase in accuracy provided by using an atom interferometer is beneficial to inertial navigation systems (INS).

This research looks specifically at measuring the resulting phase from the interference. As shown in Figure 1, the atomic paths still split after interfering, leaving two packets of atoms which need to be measured, in this case imaged, to find the number of atoms in each group. The intent is that in the future, some of this work will help enable the necessary data measurement capabilities in a situation where the atoms being measured are not in a fully predictable position. There is also the case where the atomic distribution at measurement may have volumetric structure that would need to be observed to produce a useful accelerometer signal. In both [29] and [15], useful interference patterns were only observable when the pattern of interest was in the focal plane of the camera, therefore the whole experiment had to be designed around that constraint. To allow observation of moving and possibly complex structures in the atom clouds, the principle is to measure the entire volume containing

the atoms. This can be done using what is called a plenoptic camera. This type of camera measures the angular direction of the light rays reaching the sensor. This information can be used to extract depth information from the scene with a single picture allowing 3D images to be taken with a single camera in one shot, which is important when imaging cold atoms. Additionally the ability to observe information along the imaging axis as well as the information in the focal plane would be beneficial in extending the use of atom interferometry into more complicated interference geometries.

### 1.1.2 Limited Optical Access.

The second consideration motivating this work is the space needed to observe the atoms. Almost all measurements of cold atoms are optical as any physical probe would not be able to interact with the system, so optical access is necessary for probe beams or for light radiating from the atoms to be imaged or measured. Taking 3D images can be done with multiple cameras but this can take excess space and resources, and optical access (or observation solid angle) can be a constraint, especially for experiments with cold atoms. Utilizing a plenoptic camera allows access to the available 3D information even when the observation solid angle is constrained. Laser cooling experiments require environmental isolation in vacuum and optical access for multiple large laser beams. As will be discussed in the next chapter, in order to cool atoms, laser beams need to be directed at the atoms from six directions; three pairs of counter propagating beams along each of the three primary axes. The laser beams needed to perform the necessary atom optics operations also need to have access. Additionally, the magnetic fields needed to trap and contain the atoms must have a source such that the field surrounds the atoms appropriately. Each of these items uses or blocks part of the surface area surrounding the atoms.

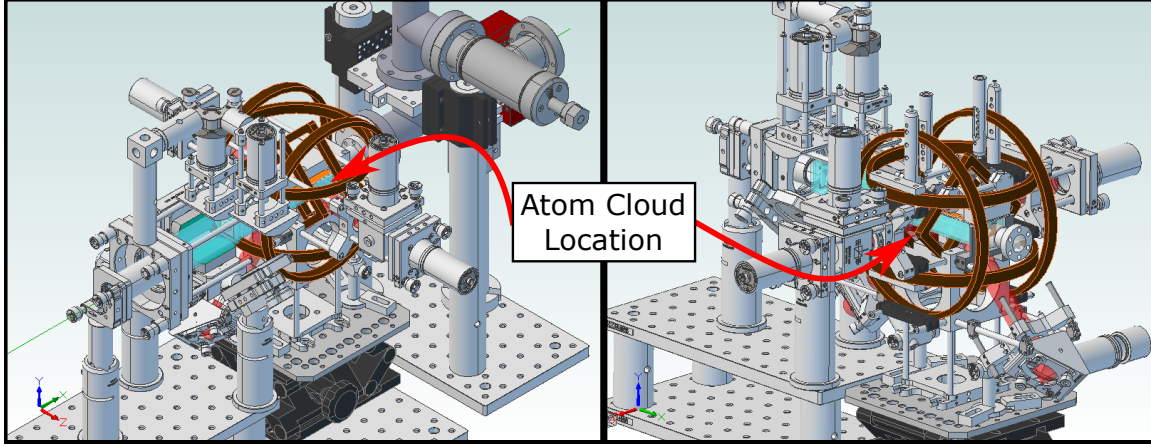
These laser-cooled atom systems are being designed to be small and portable which leads to compact architectures. This means all these laser and atom control elements are near the atomic cloud and surrounding the vacuum chamber. The area around the atoms decreases as the radius squared as the volume is reduced. The system components can easily fill most of the space around the chamber making optical access for an imaging system very limited.

Figure 2 shows two perspectives of an example cold atom interferometer system<sup>1</sup>. It was designed and built by the Cold Atom Laboratory team at the AFRL/RV. It is already implementing techniques to reduce the size of the system. A thin chip is being used to create the primary magnetic fields needed to trap and manipulate the atoms. Additionally, the entire interferometer path of the atoms is contained on the chip, as opposed to older systems that launch the atoms through up to meters of free space. The volume of the system pieces shown is approximately 50cm × 50cm × 30cm. The system is a clear demonstration of the limited optical access to the atom cloud. The parts of the system shown in the image do not include cameras or imaging optics. These still need to be added in such a way that the atoms can be seen through the surrounding optics and structure.

In the case that an atom interferometer needed information about atom cloud at high resolution in 3D, one needs to either install two orthogonal cameras, scan a focal plane through the cloud, or both. A plenoptic camera allows for imaging the perspective views needed for 3D data reconstruction with a single camera, making collecting the desired 3D information about the atom cloud possible while not requiring additional optical access to the atoms.

---

<sup>1</sup>System diagram created by Dr. Brian Kasch, AFRL/RVBY.



**Figure 2.** Two different views of the same cold atom interferometer system created by the team at the Cold Atom Laboratory at the Air Force Research Laboratory Space Vehicles Directorate. The atoms to be observed are inside the light blue vacuum chamber in the center of the brown magnetic field coils. The image demonstrates the limited optical access for a typical atom interferometer system. No imaging optics or cameras are shown. The camera needed to measure the atom distribution would need to be able to see the atoms through a gap in the structure already present. The scale of this system is about  $50\text{cm} \times 50\text{cm} \times 30\text{cm}$ , future systems are being designed to be more compact. System diagram used with permission [42].

## 1.2 This Dissertation

The goal of this dissertation was to develop and build a plenoptic imaging system for a trapped cold atom cloud, capable of 3D imaging. The system would be based on a single camera with high resolution. It would also need to be able to image the cloud from outside the magneto-optical trap (MOT) containing the cloud of atoms. There are primarily two methods of imaging cold atoms, fluorescence imaging and absorption imaging, and both were considered, first fluorescence imaging and then absorption.

Presented in this dissertation are the first three-dimensional fluorescence images of atoms in a MOT using a light field microscope imaging system. The optic system used was built around a Lytro® Development Kit (LDK) micro lens array (MLA) and sensor which provided a cost effective high resolution plenoptic sensor. The 3D reconstruction capability of the system is analyzed and improvements and future

design considerations are presented.

Previous work on light field imaging of fluorescing atoms [64] did not create an imaging system that would work with a functioning cold atom system. In order to capture light field images of atoms in a MOT, the MOT was designed to allow as much optical access as possible (discussed in Chapter II). A light field microscope (LFM) was designed with a long working distance Mitutoyo Plan Apo Near Infrared (NIR) Infinity Corrected microscope objective and necessary optics to image the millimeter-sized cloud of atoms, resulting in a very different optical system than previous LFM systems [64, 46, 14]. The optics and theory of light propagation through the LFM were carefully analyzed in order to properly model the point spread function (PSF) of the system. It was found that assumptions had to be adjusted in order to accurately produce the PSF used to extract three-dimensional images (discussed in Chapter IV). Additionally the necessary processing and modeling of the images and PSFs, which was based on code created by the Stanford LFM group [14], had to be modified to account for both the LDK MLA and sensor as well as the optics of the unique LFM designed in this work (discussed in Chapter IV). The results of this work have been submitted for publication [49].

The LDK sensor and surrounding control package was found to be incapable of collecting absorption images effectively. It is shown in Chapter V that a light field system in general is not able to capture the needed angular data to extract 3D information when performing absorption imaging with a standard plane wave probe beam. An alternate method for 3D absorption imaging is proposed utilizing an incoherent probe beam.

### 1.2.1 Outline.

The background and theory behind magneto-optical traps is presented in Chapter II. An overview of the optics and theory of plenoptic imaging systems, starting with a standard plenoptic camera, then moving to the light field microscope is presented in Chapter III. Chapter IV presents the results and analysis of florescence imaging of atoms in a MOT which is the basis of a submitted paper [49]. Images using a 0.26 numerical aperture (NA) objective system will be presented with the reconstructions and analysis of the performance and comparisons to a 0.14 NA, particularly regarding the optical axis spreading of the reconstructed 3D volumes. Chapter V looks at the application of a plenoptic imaging system to absorption imaging. And Chapter VI will give a brief recap and conclusions.

## II. Trapping and Cooling Atoms

The development of Cold Atom technology and the creation of Bose Einstein Condensates (BECs) has an interesting history. A paper by Einstein and Bose written in 1925 predicted the existence of the state of matter now called a BEC [30]. The theory of BECs was developed at that time, but it was 70 years later that one was experimentally created. In order to condense gaseous atoms into a BEC, atoms must be cooled to near zero Kelvin, and it was not until laser cooling was developed that it became possible to cool the atoms to such temperatures. One of the breakthroughs that lead to the creation of BECs was the magneto-optical trap (MOT) which is used to initially cool and trap the atoms and is the primary system used in this work. Raab at Bell Labs was one of the first to demonstrate a MOT for trapping neutral atoms [57]. This was followed by a race to cool the atoms down to a BEC between the research teams of Eric Cornell and Wolfgang Ketterle. It was an accomplishment which they knew would result in a Nobel Prize. Each produced a BEC in 1995, first Cornell's group and then a few months later, Ketterle's team [5, 24]. The goal of creating a BEC from a gas of dilute atoms spurred the creation of the technology necessary to cool, control, and manipulate atoms in a new way, and the properties of the atoms are now being exploited for improving inertial navigation systems.

Cold atoms is the term used here to describe a dilute gas of atoms which has been laser-cooled down to the milli-Kelvin level. It is a fairly broad category as there are different ways to trap the atoms, different atomic elements that can be used, and a range of different temperatures that can be reached. Here it will refer to atoms that have been laser-cooled in a MOT and in some cases cooled further to a BEC.

## 2.1 Doppler Cooling and Optical Molasses

The basic principle behind using lasers to cool and trap atoms is that photons carry momentum, which they impart to an atom when absorbed. For a simple two-level atom and a photon on resonance with the transition, the momentum kick to the atom from the photon when the photon is absorbed is  $mV = \hbar\vec{k}$  where  $m$  is the mass of the atom, and  $V$  is the velocity imparted by the momentum kick from the photon traveling with wave vector  $\vec{k}$ , and  $\hbar = h/2\pi$  where  $h$  is Plank's constant. When the atom relaxes back to the ground state the photon is emitted in a random direction which also creates a momentum kick opposite the direction of the emitted photon. If many photons are absorbed which are all coming from the same direction, then the momentum kick associated with re-emission will average out and the momentum kick on the atom will simply be the combined momentum of the absorbed photons. This change in momentum is of course a force on the atom which can be used to slow it down, that is cool it.

An atom moving with a velocity  $\vec{v}$  toward a laser beam with a frequency  $\omega_l$  will see a Doppler shifted frequency of

$$\omega = \omega_l - \vec{k}\vec{v}.$$

If frequency  $\omega_l$  is shifted to a frequency lower than the resonant frequency of the atom transition  $\omega_0$ ,  $\omega_l < \omega_0$ , and  $\vec{k}$  is in the opposite direction of  $\vec{v}$ , then  $\omega$ , the Doppler shifted frequency, will be shifted closer to resonance. Atoms moving toward a red detuned laser beam will absorb more photons and feel a greater force than those not moving or moving in the opposite direction given  $\vec{v}$  is not too large. The force felt by

the atom in its reference frame depends on the scattering rate of the photons  $R_s$ ,

$$R_s = \frac{\Gamma}{2} \left( \frac{I/I_{\text{sat}}}{1 + I/I_{\text{sat}} + 4(\Delta + \omega_d)/\Gamma)^2} \right),$$

where  $\Gamma$  is the linewidth of the atomic transition,  $I$  is the intensity of the laser,  $I_{\text{sat}} = \pi\hbar c\Gamma/(3\lambda^3)$  is the saturation intensity where  $c$  is the speed of light, the laser detuning is  $\Delta = \omega_l - \omega_0$ , and  $\omega_d = -\vec{k}\vec{v}$  is the Doppler shift of the frequency [44]. The force is then given by

$$\vec{F} = \hbar\vec{k}R_s.$$

If there are two counter propagating beams then the total force along one dimension is

$$\vec{F}_{\text{OM}} = \vec{F}_+ + \vec{F}_-$$

where

$$\vec{F}_{+,-} = \pm \frac{\hbar\vec{k}\Gamma}{2} \left( \frac{I/I_{\text{sat}}}{1 + I/I_{\text{sat}} + 4(\Delta \mp \omega_d)/\Gamma)^2} \right).$$

These two component forces and their sum are plotted in Figure 3. These forces on a single rubidium atom are on the order of  $10^{-20}\text{N}$ , where the force due to gravity is on the order of  $10^{-24}\text{N}$ . The region near  $\vec{v} = 0$  is linear with respect to velocity and opposite in direction. By arranging six such laser beams, three pairs of counter propagating beams along each axis in space, a 3D slowing force can be applied. This is called an optical molasses (hence the OM in  $\vec{F}_{\text{OM}}$ ), the atoms will still diffuse out of the region, but inside, feel a velocity dependent slowing force acting against them in all directions.

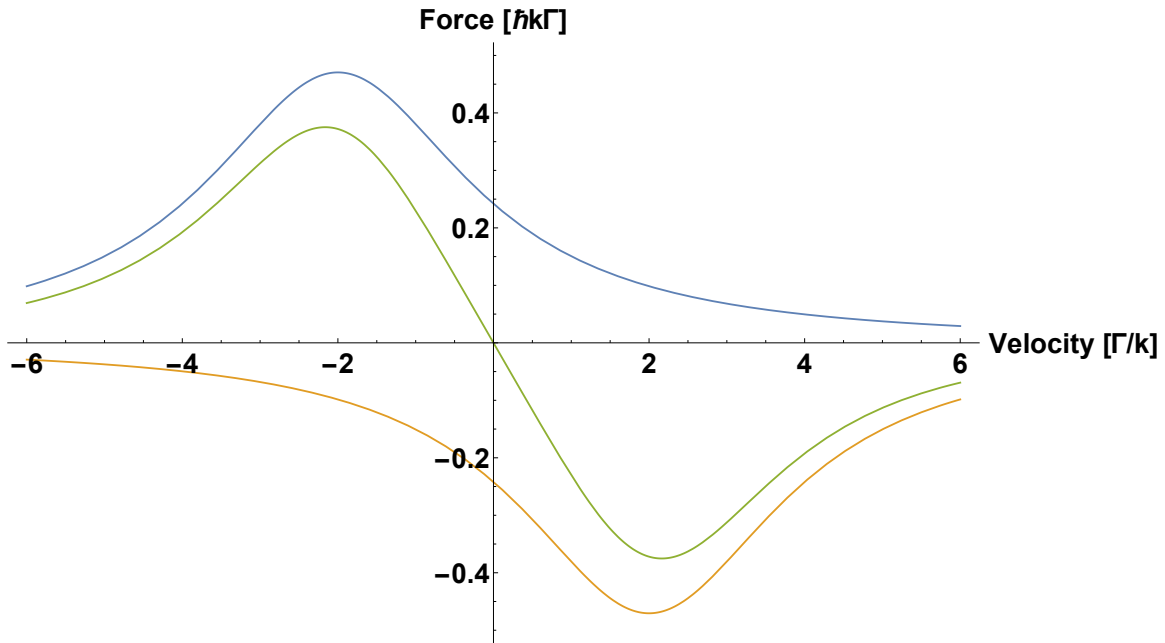


Figure 3. The force felt by a two-level atom in an optical molasses plotted versus atom velocity for a frequency detuning of  $\Delta = -2\Gamma$ . The blue and orange lines show the force contribution from the left and right propagating beams respectively. The green line shows the total force from both. Near zero velocity, the force is close to linear and opposite in direction (sign) to the velocity of the atom, creating an optical molasses where the atoms are slowed by a force proportional and opposite to their velocity. For rubidium atoms being cooled on the  $D_2$  line  $\hbar k\Gamma = 3.2 \times 10^{-20}$  N and  $\Gamma/k = 4.7$  m/s.

## 2.2 Magneto-Optical Traps

A magneto-optical trap (MOT) is formed using both a trapping magnetic field and the optical molasses [44]. The magnetic trap is a linearly varying magnetic field about a zero point created by a magnetic spherical quadrupole. The magnetic field is produced by two rings of current arranged in an Anti-Helmholtz configuration. The magnetic field splits the Zeeman levels of an atom as shown in Figure 4 for a spin-one excited energy level in one dimension. At the zero point of the spherical quadrupole, six lasers are directed in counter-propagating beams along each of the three dimensions. These are polarized with  $\sigma_+$  or  $\sigma_-$  polarization, such that  $\sigma_+$  light is propagating along the positive axis in a given direction and  $\sigma_-$  is propagating along the axis in the negative direction. Figure 5 shows the geometry of the lasers. If the lasers are red-detuned from the resonant  $B = 0$  atom transition frequency, then atoms on the positive side of an axis will absorb more  $\sigma_-$  photons and feel a net force toward the origin. The same will be true for atoms on the negative side of an axis, but now absorbing more  $\sigma_+$  light. This produces a location-dependent force which pushes atoms back toward the center of the trap.

The lasers are red shifted off the resonance for the atomic absorption transition creating an optical molasses at their crossing, cooling the atoms. Near the center of the magnetic quadrupole field the carefully polarized light creates a force pushing them toward the center that is linearly dependent on position. This produces a 3D harmonic potential in which the cooled atoms get trapped [57].

The operation of the MOT describes the atoms as they are being trapped, but it does not well describe how the atoms behave near the center of the trap once they have been trapped there. At this point, the forces on the atom become much more complicated as collisions, light shielding and photons from radiating atoms all come into play, and these will have an effect on the density distribution of the atoms.

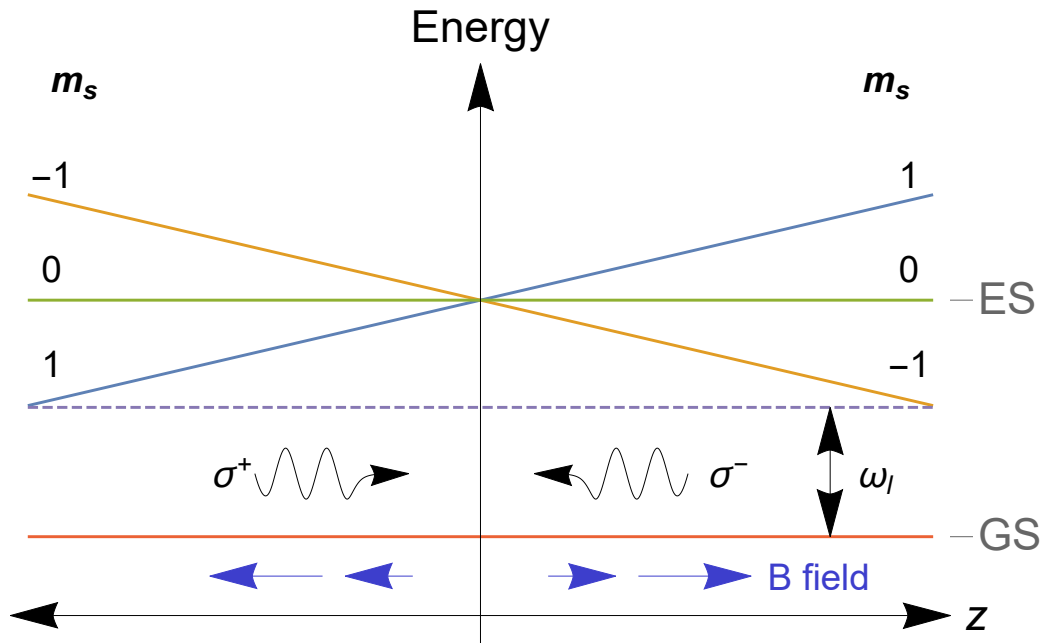


Figure 4. The ground state (GS) and excited state (ES) energy levels of the  $m_s = -1, 0, +1$  spin states of a two level atom in a weak inhomogeneous magnetic field represented at the bottom in blue. Laser light of  $\sigma^+$  and  $\sigma^-$  polarization and frequency  $\omega_l$  is directed toward the center from opposite sides, with an energy corresponding to the lower of the spin states. Atoms at positive  $z$  positions will preferentially absorb  $\sigma^-$  light and feel a force back toward the origin. Similarly, atoms at negative  $z$  positions will feel an opposite force from the  $\sigma^+$  light.

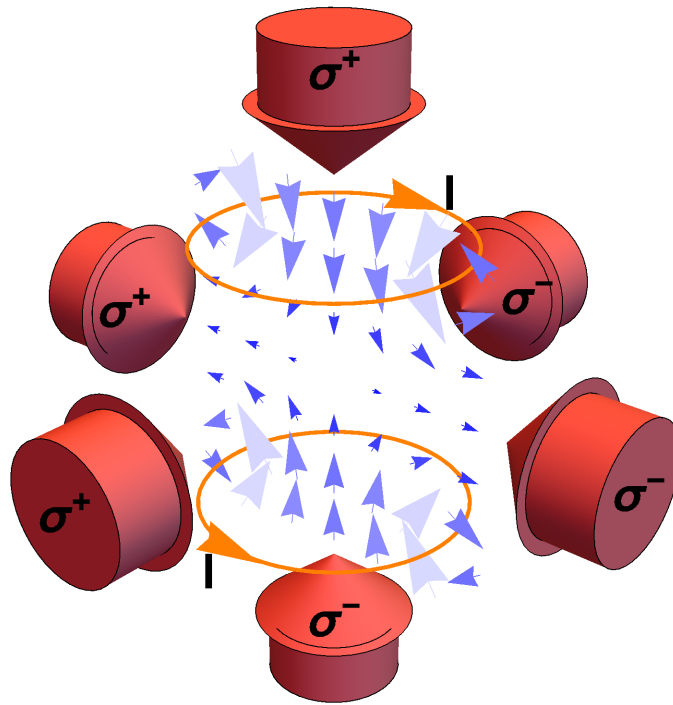


Figure 5. A diagram of a 3D magneto optical trap. A single 2D slice of the magnetic field is shown in shades of blue, demonstrating the field direction and magnitude near the center of the trap. The magnetic field is created by current  $I$  running through coils represented by the orange loops. The cooling laser beams are represented by the large red arrows and the necessary  $\sigma^+$  or  $\sigma^-$  polarization labels each one.

There are some basic models to try to describe the distribution; the models laid out by Townsend [69] are followed closely here. The first is called the temperature-limited regime, the second the multiple-scattering regime, and the third is the two-component regime.

The temperature-limited regime is called such because the volume of the trapped cloud depends on its temperature. In this regime, the density of atoms is low and interactions between atoms can be ignored. In this case, because the trap is a harmonic oscillator potential, the atom's distribution is close to Gaussian. The Gaussian is characterized by three Gaussian widths,  $r_x$ ,  $r_y$ , and  $r_z$ . The radii depend on temperature and are related by

$$\frac{1}{2}\kappa_{ii}r_{i,T}^2 = \frac{1}{2}k_B T,$$

where  $\kappa_{ii}$  is the spring constant tensor,  $k_B$  is the Boltzmann constant and  $T$  is the temperature. The spring constant is the negative of the gradient of the force at the origin, which in this case is determined by the magnetic field gradient and the detuning of the laser

$$\kappa = \kappa_0 \frac{\Gamma}{\delta} \frac{b}{b_0} \quad (\text{for } \delta > 2\Gamma),$$

where  $b$  is the gradient of the magnetic field in the  $z$  direction,  $\kappa_0$  is a proportionality constant, and  $b_0 = 1[G/cm]$ . For a spherical quadrupole magnetic field,  $\kappa_z = 2\kappa_x = 2\kappa_y$ , which from the relation above means  $r_z = \sqrt{2}r_x = \sqrt{2}r_y$ . Defining  $\kappa \equiv \kappa_z$  and  $r \equiv r_z$ , then

$$r_T = \sqrt{\frac{k_B T}{\kappa}}.$$

The peak spatial atomic density at the center of the elliptical Gaussian distribution is

$$n_0 = \frac{N}{2(\sqrt{2\pi}r_T)^3},$$

where  $N$  is the total number of atoms. Hence the density distribution for the MOT

in this regime is

$$n(x, y, z) = n_0 \exp \left\{ - \left( \frac{x^2 + y^2 + 2z^2}{2r_T^2} \right) \right\} \quad (4)$$

The multiple-scatter regime comes into play when the number of atoms  $N$  goes above around  $10^4$ , for typical MOTs. At this point re-emitted photons scattered off the cloud of atoms is an important effect. There is not a simple model for this but simply an empirical scaling law. The distribution is still Gaussian but now the peak density is

$$n_{ms} = C_{ms} \frac{\kappa_0}{\lambda \hbar \Gamma} \frac{b}{b_0} \left( \frac{\delta \Gamma}{\Omega^2} \right)^{1/2} \quad (\delta > 2\Gamma),$$

where  $C_{ms}$  is a dimensionless scaling factor determined by experiment.  $\Omega$  is the Rabi frequency of the atom in a light field of intensity  $I$  given by

$$\Omega = \Gamma \sqrt{\frac{I 6 \lambda^3}{4 \pi \hbar c \Gamma}}.$$

In this regime, the density also becomes independent of number of atoms trapped. In some models, taking this into consideration leads to a uniform density distribution, but this does not appear in experiments except when very small magnetic gradients and laser detunings are used. Typically the density is still Gaussian, but the maximum density no longer depends on  $N$ . The Gaussian is broadened by the multiple-scatter from other atoms. This makes the Gaussian nearly uniform with a radius of

$$r_{ms} = \frac{1}{\sqrt{2\pi}} \left( \frac{N}{n_{ms}} \right)^{1/3}.$$

This radius would replace  $r_T$  in equation (4).

The third regime is the two-component regime. Here, the atoms fill a volume large enough that they go beyond where the force from the radiation and magnetic field is linear. This shape is not well defined but has a denser spot in the center where the

above regimes still hold and a larger surrounding cloud. The boundary between the dense region and the rest of the cloud is given by

$$r_l = C_l \frac{\hbar\Omega^2}{\mu_B b\delta}, \quad (5)$$

where  $C_l$  is a proportionality factor depending on the atomic element and trap and is found such that  $r_l$  is the radius where the restoring force has a local maximum, and  $\mu_B$  is the Bohr magneton.

The MOT created for this work was very flexible and distributions in all of these regions were possible. In practice, the atom clouds were kept small for the purposes of imaging with the light field system, placing the distributions in the first and second regimes. However as discussed next, the MOT created was not as simple as this analysis, and in the end, the atom clouds were not strictly Gaussian distributions in any sense, but this is the basic shape used to analyze the locations of the clouds and this is the motivation for this choice.

### 2.3 The Experiment's Magneto-Optical Trap

The MOT built for this work trapped rubidium 87 atoms in a ultra-high-vacuum chamber. As just discussed the MOT can produce the forces necessary to trap the atoms. However, in practice if there is a thermal distribution of rubidium atoms in a chamber only a subset will be captured, as evident from looking at Figure 3; the rest will have velocities too high for the trap to be effective [55]. If there are too many of these atoms present in a volume then they will continually knock atoms out of the trap. To prevent this, the chamber used (and all such MOT systems) was under ultra high vacuum with a pressure on the order of  $10^{-9}$  Torr.

The two electron energy levels of rubidium used for the MOT cooling are the  $5^2S_{1/2} F = 2$  and the  $5^2P_{3/2} F' = 3$  states of the atom, where  $F$  is the hyperfine spin state of the energy level. The atoms are continuously being pumped up to the  $F' = 3$  state then spontaneously radiating back down to the  $F = 2$  state. Occasionally an atom will be pumped to a different excited state which could decay back to the  $F = 1$  ground state. This atom ceases to be in resonance with the cooling light and falls out of the trap. Because of the continual pumping, this quickly happens to all the atoms in the trap. To prevent the atoms from all falling out, a repump beam is propagated down the same path as the cooling beams. It is tuned to the  $F = 1$  to  $F' = 2$  transition, which moves population out of the  $F = 1$  state and back into the cooling states. The energy levels are shown in Figure 6.

The MOT was created using a simple set-up with the intent of making it easy to access with the imaging system and get as close as needed with the objective. Figure 7 is a diagram of the set-up. The light source was a diode-pumped Ti-Sapphire laser with output powers on the order of a Watt. This light was used for cooling and trapping the atoms. The beam had three pick-off beam splitters, one for monitoring the wavelength, one to provide probe light for absorption imaging and one for creating a frequency lock to a rubidium reference cell. The main beam then went through a 105MHz acousto-optical modulator (AOM). This blue-shifted the frequency of the laser by 105MHz which was adjustable over a bandwidth of 30MHz. This allowed the laser to be locked to the large mixed transition observed by saturation spectroscopy of the reference cell. The mixed transition is halfway between the  $F = 2$  to  $F' = 2$  and the  $F = 2$  to  $F' = 3$  transitions and is 133MHz red of the cooling transition. The splitting is shown in Figure 6. The blue-shift sets the laser to a frequency red-detuned from the primary  $F = 2$  to  $F' = 3$  transition by a few linewidths ( $\Gamma = 2\pi 6.065\text{MHz}$ ), as is needed to create the MOT. The exact detuning could be controlled with the AOM

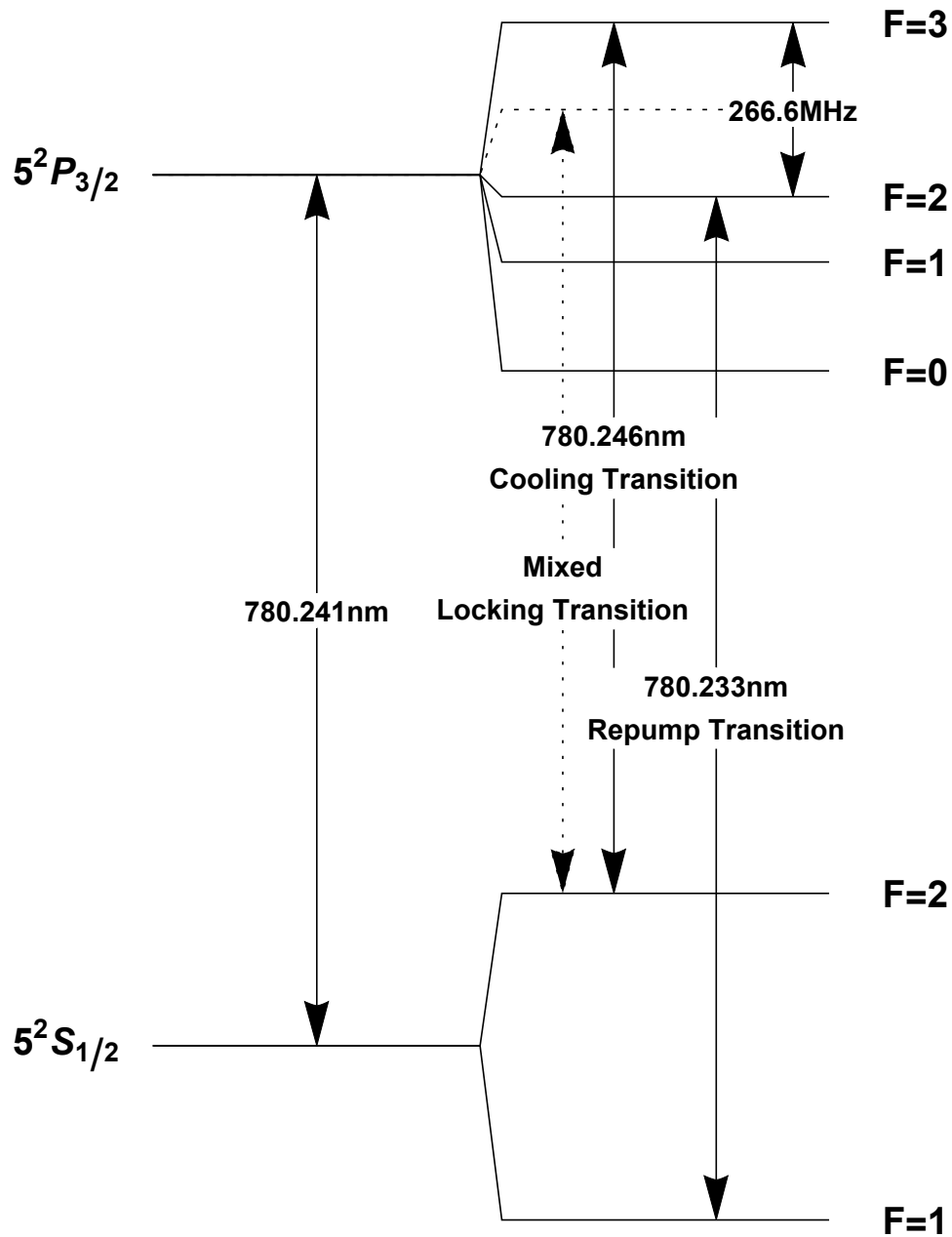


Figure 6. The energy levels of the D<sub>2</sub> transition in rubidium 87. The two levels used for cooling and trapping are labeled along with the repump transition. The splitting of the  $F' = 3$  and  $F' = 2$  is pointed out, the mixed saturation spectroscopy absorption line of these two levels was used as the frequency lock for the cooling laser. A frequency shift of slightly less than half this splitting was used to shift the cooling beam to just red of the cooling transition frequency.

when the laser was locked and directly controlled by the laser when it was not.

The cooling beam, after passing through the AOM, was expanded about 10 times to be over an inch in diameter and re-collimated. The expanded beam was irised to a desirable size depending on how big an atom cloud was desired. It was then sent through two half-wave plates and polarizing beam splitters sets, splitting it into three beams and allowing relative adjustment of each beam's intensity. One beam went through the vacuum chamber at a 45° angle. The second came down the end of the chamber 45 degrees off the first beam, along the  $x$ -axis in Figure 7. The third beam was reflected up above the chamber and then down through the crossing point of the first two beams, along the  $y$ -axis. Each was retro-reflected creating, with the use of six quarter-wave plates along each beam, the six crossing beams with the correct  $\sigma_{\pm}$  polarization needed to form the optical portion of the trap.

Two rectangular copper wire coils were used to create the magnetic quadrupole portion of the trap. They were placed in direct contact with the glass of the vacuum chamber, oriented along the normal axis to the table; the third cooling laser beam coming down through them. The resulting MOT had a magnetic field gradient of approximately 5 Gauss/cm. The typical number of atoms was on the order of  $10^5$ . The temperature of the atom cloud was never measured but is estimated to be on the order of 100 mK.

The vacuum chamber was an approximately 4.3cm by 3.6cm by 20cm glass chamber connected to the rest of the vacuum system. The vacuum system was a basic 'T' shape where the left side of the cross beam was the glass chamber (see Figure 8). The other side of the 'T' cross beam was a window which allowed the cooling laser through to a mirror that reflected it back down the chamber. Mounted just inside the window were two rubidium dispensers that released rubidium when a current was applied, providing the source of rubidium vapor for the trap. Along the leg of the 'T' there

was a Titanium sublimation pump and a large ion pump along with a valved port to attach roughing and turbo pumps. The vacuum system was cleaned by heating the entire chamber to just over 100° Celsius for three days while pumping out released gases with the roughing and turbo pumps. The temperature ensured the ion pump and glass chamber glue did not get too hot. The combination of sublimation pumping and continuous ion pumping resulted in a minimum chamber pressure of  $10^{-10}$  Torr. When dispensing rubidium the pressure would rise to as high as  $10^{-8}$  Torr.

A wire was placed in the beam path of a cooling beam in order to create an atom distribution which could be clearly observed to have density variation along the optical axis of the plenoptic camera. The shadow of the wire was imaged onto the atoms using a 4f optical system. The wire was oriented along the  $y$ -axis and placed in the cooling beam running along the  $x$ -axis. This caused the atoms to split along an  $xy$ -plane creating two clouds of atoms, displaced along the  $z$ -axis, the optical axis of the plenoptic camera. Figures 7, 8 and 9 show diagrams and images of the layout of the MOT system.

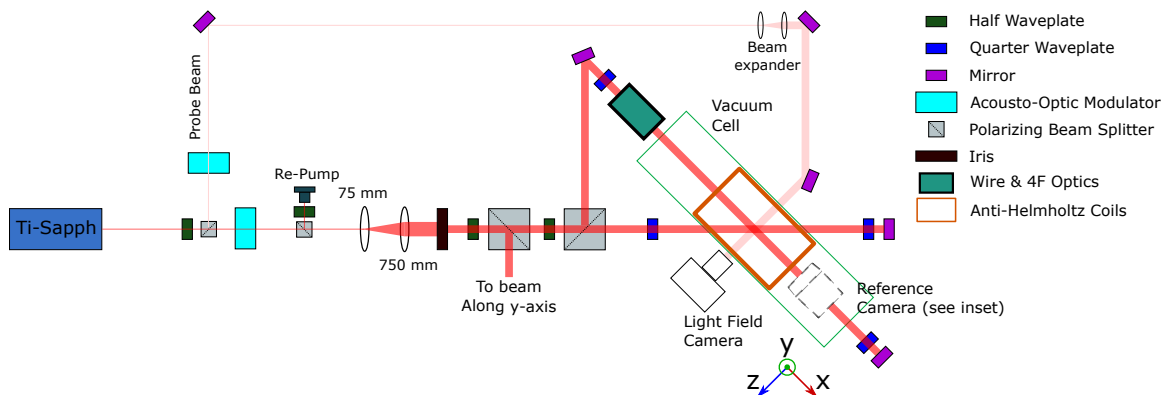


Figure 7. A diagram of the Magneto Optical Trap. A top-down view of the vacuum chamber and corresponding lasers and optics needed to create the MOT. The  $y$ -axis beam is directed up above the chamber and comes down from out of the page through the vacuum chamber, and the reference camera is also out of the page looking down at approximately  $53^\circ$ . The probe beam was only used during absorption imaging attempts and was typically off and could be quickly switched on and off using the AOM. Figure 9 shows a side view of the chamber. The coordinate vectors match the plenoptic camera's reference frame in both images. This is the same reference frame used in the plenoptic images in Chapter IV.

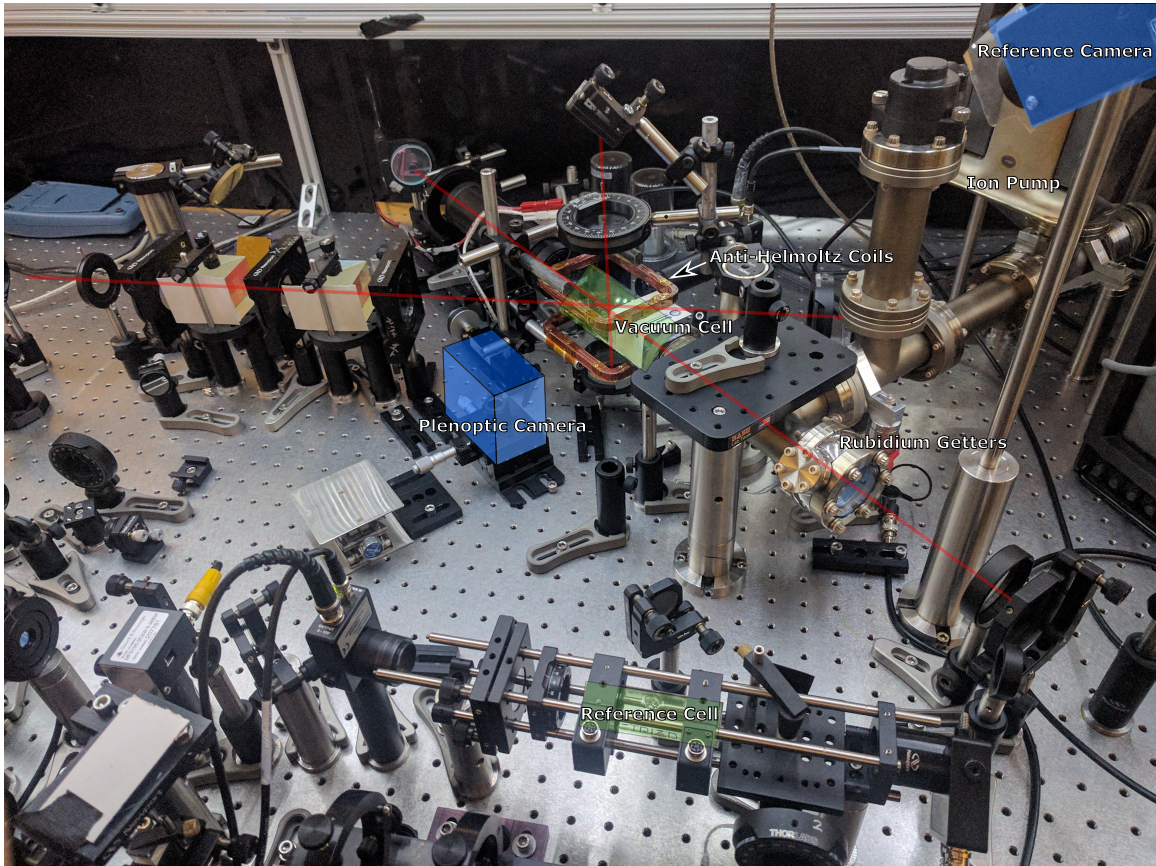


Figure 8. The magneto-optical trap built for this experiment and represented in diagram form in Figure 7.

### Light Field Optic-Axis View

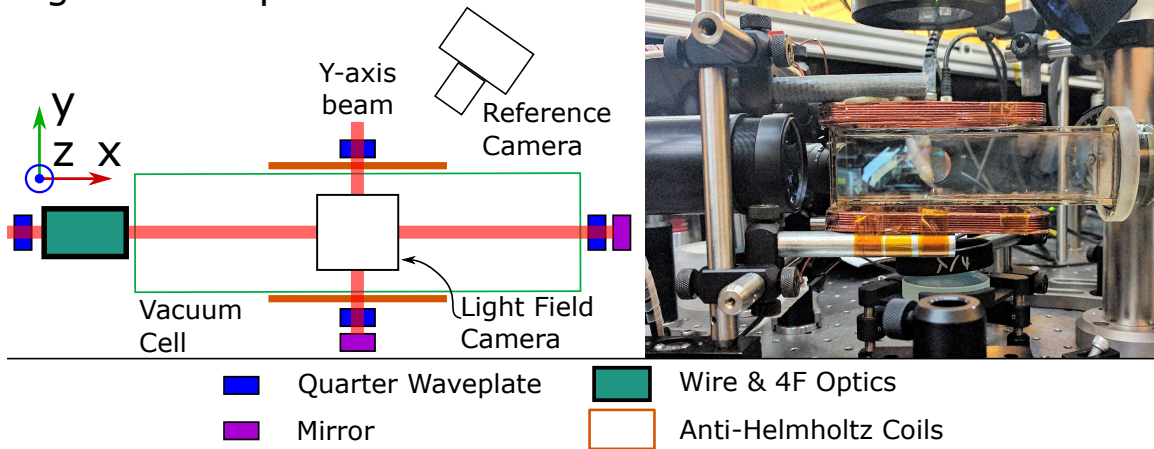


Figure 9. A side view of the Magneto Optical Trap. The left diagram shows the vacuum chamber from the direction of the plenoptic camera, and shows the basic orientation of the reference camera above the chamber. The coordinate vectors match the plenoptic camera's reference frame. The right image is a picture of the vacuum chamber from the same angle. The post in the center bottom is where the LFM camera was mounted. The large tube and optic on the left side of the image is the 4f lens system imaging the shadow of the wire onto the atom cloud.

### III. Light Field Imaging

The previous chapter described the MOT and how it was used to create a cloud of cold atoms. How to image these clouds in three dimensions is the next topic. The plenoptic function is introduced here along with the principles behind plenoptic imaging systems after a brief overview of previous work. Then the theory of light field microscopy will be discussed.

#### 3.1 Previous Work

The concept of the plenoptic function was first laid out by Adelson and Bergen [2] in 1991 at the Massachusetts Institute of Technology (MIT). They define the function as the complete description of the radiance of light in a space. The plenoptic function is a seven-parameter function given by,  $L(x, y, z, \theta, \phi, \lambda, S)$ . It gives the radiance  $[W/(cm^2sr)]$ , for a given point in space  $(x, y, z)$ , in a given direction  $(\theta, \phi)$ , for a given wavelength and polarization  $(\lambda, S)$ . The plenoptic function was developed in the context of trying to understand vision and its properties with the application to computer vision in mind. The term light field used here, was proposed in 1996 by Levoy and Hanrahan at Stanford [45] also as a way to create computer generated images of a scene, though the phrase was first used by Gershun in “The Light Field” [35]. The plenoptic function and the light field describe the same properties of light in a volume and are often interchanged in this paper. Using a light field or the plenoptic function, an image can be generated anywhere within the area the function describes and from any perspective. If there are no occlusions or absorption, it gives all the information needed to create images for any view-point in the volume described.

The concepts of a light field camera can be traced back to as early as 1908 [48], but Adelson and Wang were the first to propose capturing the plenoptic function

with a camera in 1992 [3]. They proposed placing a micro lens array (MLA) where the sensor of a camera typically would be with the sensor moved one micro lens focal length further back. They called this a plenoptic camera. In this geometry, each micro lens in the array acts as a new pixel. The pixels behind the micro lens record from which direction the rays entered that micro lens, Figure 10 shows the basic geometry. The plenoptic camera trades spatial resolution for resolution in the angle at which the light arrives. The principle is, if the light field can be captured directly with this type of camera, then the view can be changed to anything within that plenoptic field. Adelson used this specifically for retrieving depth information from a picture in what they called “single lens stereo.” The idea of the plenoptic camera was then used by Ren Ng *et al.* at Stanford and applied more specifically to refocusing as opposed to depth [54, 53]. There the theory and function of the plenoptic camera were further explored and the design and processing of the images improved to photo quality. The ideas of the plenoptic camera spread and were the focus of research from a few groups, especially with regards to improving the spatial resolution without losing the ability to refocus [33, 9, 11]. Shortly after Ng completed his dissertation [53], he started the company Lytro® which makes commercial light field cameras. These have been specifically studied [34, 10] to understand their limits. Thanks to this work, the foundation for plenoptic imaging for photography is well established (even entering virtual reality). A development kit made by Lytro® is used as the MLA and sensor piece of the light field imaging system used in this work. The details of the Lytro® Development Kit micro lens array and sensor are discussed in Section 4.1.

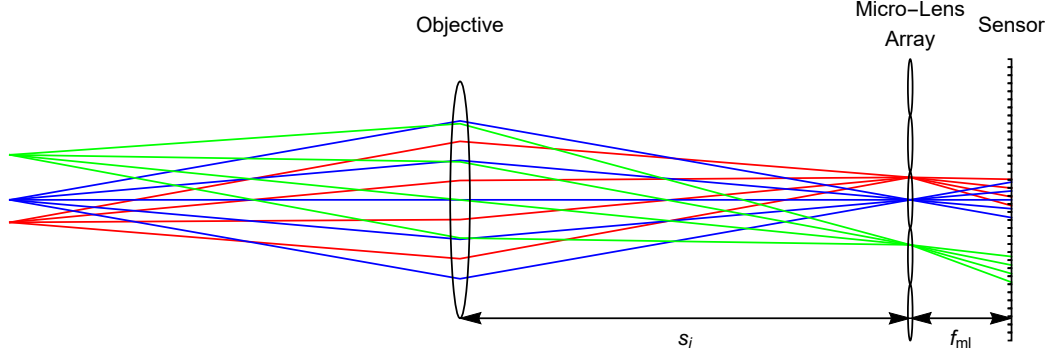


Figure 10. A ray trace and optics of a plenoptic camera. Points in the object plane are imaged to the MLA, and the angle of rays hitting the MLA is recorded by the pixels behind the micro lenses. The MLA is placed at the image plane of the objective  $s_i$  and the sensor is one micro-lens focal length  $f_{ml}$  behind the MLA.

### 3.2 The Plenoptic Function and Light Field Imaging

The seven-parameter plenoptic function can be simplified to five parameters when ignoring wavelength and polarization giving  $L(x, y, z, \theta, \phi)$ , the radiance of a ray described by its starting position and direction. Assuming there is nothing blocking the path of a ray and no absorption or scatter, the radiance will not change along a given ray and you can reduce the function to four dimensions. Then, the plenoptic function can be written as the radiance in a 2D plane [28]

$$L(s, t, \theta, \phi) = \frac{d^2\Phi(\Omega, A_1)}{d\Omega dA_1 \cos\theta}, \quad (6)$$

where  $\Phi$  is the radiant flux going through area  $A_1$  into the solid angle  $\Omega$  as shown in Figure 11, which shows the geometry used for describing the equation.  $L$  can be simplified by using a two-plane parametrization; the elevation angle,  $\theta$ , and azimuthal angle,  $\phi$ , can be defined in terms of  $(u, v)$  given the distance,  $l$ , between two planes; assuming the distance from the  $(s, t)$  plane to the  $(u, v)$  plane is large compared to  $\sqrt{s^2 + t^2}$  and  $\sqrt{u^2 + v^2}$ , then  $\cos(\theta) \approx 1$  and the plenoptic function can be simplified

to

$$L(s, t, u, v) = \frac{l^2 d^4 \Phi(s, t, u, v)}{ds dt du dv}. \quad (7)$$

The two-plane parameterization works well when looking at a plenoptic camera where the planes are the main lens  $(u, v)$  and the image plane  $(s, t)$ . Given these two planes, any ray can be given by a point on each plane, with the function represented by  $L(s, t, u, v)$ . Figure 11 shows both planes and the ray intersecting them that goes from the center of  $A_1$  to the center of  $A_2$ . If this is the case, then given two planes with a known plenoptic function  $L(s, t, u, v)$ , i.e. the radiance along each ray between points on the plane, the radiance at any point in the volume can be found given  $L(s, t, u, v)$ .

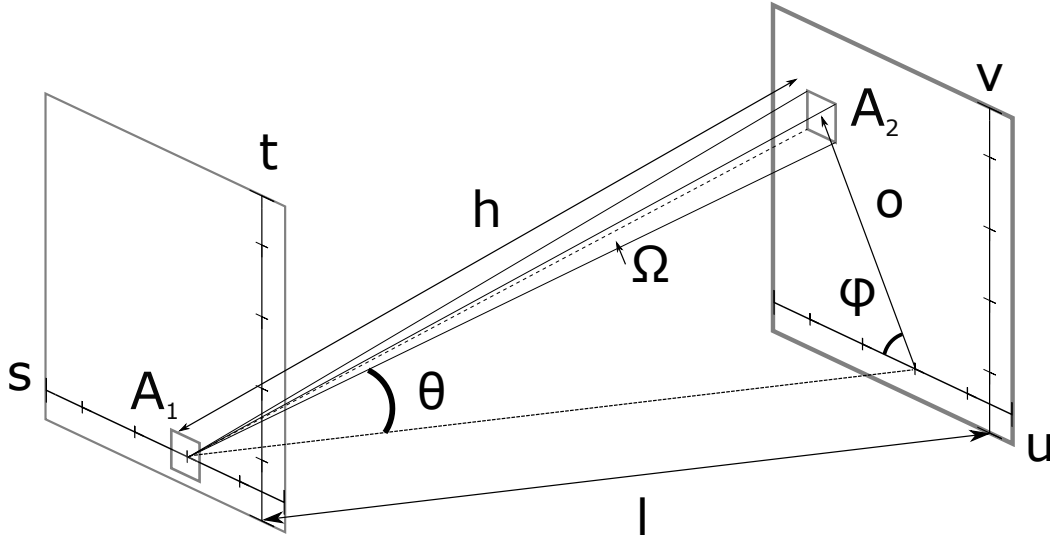


**Figure 11.** The geometry describing the plenoptic function as a radiance distribution along a 2D plane.  $L(s, t, \theta, \phi)$  gives the radiance at position  $(s, t)$  and in direction  $(\theta, \phi)$ .

A standard plenoptic camera assumes the object plane being imaged is imaged to the plane of the MLA, and the sensor is one micro lens focal length from the MLA. This is the design of a plenoptic 1.0 camera. To understand how this plenoptic camera captures the plenoptic function, it can be simplified by looking at only one dimension in each plane,  $s$  and  $u$ . Assuming the objective is creating an image plane

at the micro lens array, there will be a plenoptic function there,  $L(s, u)$ . Using ray propagation matrices, the coordinates can be translated to the sensor plane behind the MLA. Assuming there is no absorption or obstructions, the radiance will not change with the ray propagation, that is  $L(s, u) = L'(s', u')$ , where  $s'$  and  $u'$  are given by the ray propagation transformation of  $s$  and  $u$ . The transformation matrices

$$L_f = \begin{pmatrix} 1 & 0 \\ -\frac{1}{f} & 1 \end{pmatrix} \quad \text{and} \quad P_d = \begin{pmatrix} 1 & d \\ 0 & 1 \end{pmatrix} \quad (8)$$

give the refraction through a lens with a focal length of  $f$  and the propagation a distance  $d$  respectively [40]. Then for propagation through the on axis micro lens and propagation one focal length to the sensor,  $s'$  and  $u'$  will be

$$\begin{pmatrix} s' \\ u' \end{pmatrix} = \begin{pmatrix} 1 & f \\ 0 & 1 \end{pmatrix} \begin{pmatrix} 1 & 0 \\ -\frac{1}{f} & 1 \end{pmatrix} \begin{pmatrix} s \\ u \end{pmatrix} = \begin{pmatrix} fu \\ u - \frac{s}{f} \end{pmatrix}. \quad (9)$$

Inverting this gives  $s$  and  $u$ , light field coordinates at the micro lens, in terms of  $s'$  and  $u'$ , coordinates at the sensor plane,

$$u = s'/f \quad u' = s'/f - s/f \rightarrow s = s' - u'f.$$

Since  $L(s, u) = L'(s', u')$ , then for a specific micro lens,

$$L'(s', u') = L(s' - u'f, s'/f).$$

This means that the light field at the sensor is equal to the light field at the micro lens with the angle,  $u$ , parametrized by the location  $s'$  at the sensor. This is shown specifically for the center micro lens but applies to the full micro lens array by simply

shifting the coordinates to be centered at a given micro lens.

In general, a standard image is created from the plenoptic function by integrating for each point on the  $(s, t)$  plane over all the points in the  $(u, v)$  plane [60]

$$I(s, t) = \frac{1}{l^2} \int_u \int_v L(s, t, u, v) dudv, \quad (10)$$

where  $l$  is the distance between the two planes. Looking at the intensity at the sensor for only the  $(s', u')$  dimensions, the intensity recorded is determined by integrating over  $u'$  for a given  $s'$ . In the case of a single micro lens,  $s = s' - u'f$  ranges over  $d$ , where  $d$  is the diameter of the micro lens. This gives an image by integrating over  $d$ ,

$$I'(s') = \frac{1}{l} \int_{u'} L'(s', u') du' = \frac{1}{l} \int_{s'/f+d/(2f)}^{s'/f-d/(2f)} L(s' - u'f, s'/f) du'$$

The intensity recorded behind a given micro lens is a record of the light field at the micro lens where the position has been integrated over the surface of the micro lens, but  $s'$  behind the micro lens records the  $u$  coordinate. The global  $s$  coordinate, due to the integration, has a resolution the size of the micro lens and is given by which micro lens a given sensor pixel is behind in the full micro lens array.

The MLA can be thought of as the new sensor plane. Each micro lens is a pixel and samples the light field in space,  $(s, t)$ . There are several pixels behind each micro lens which sample the spread of the angles of the rays which hit the micro lens,  $(u, v)$ , which can be mapped to areas on the objective plane, to relate back to the two-plane parametrization. The MLA samples the location and then the pixels behind a given micro lens sample the angle of the light. The result is the sensor, once calibrated based on micro lens center location, collects a 4D block of data, tiled across the 2D sensor. The 4D data block is  $L$  and has coordinates  $(s, t, u, v)$  representing the spatial location and the angle at which the ray hit the sensor.

This is the standard way of recording the light field; Lumsdaine in [50] describes another optical arrangement. It is essentially the same, but the objective now focuses the desired object plane in-front-of or behind the MLA, and the MLA then images that plane to the sensor. This is a plenoptic 2.0 camera and increases the spatial resolution that can be obtained at the loss of angular resolution.

In either case, the sensor records the light field at a given plane behind the objective. To find the light field at another  $(s', t')$  plane, simply apply  $P_d$  to the coordinates. Let  $L(s, u)$  be the light field recorded at the  $s$  plane. It is shifted to another  $s'$  plane resulting in

$$L(s, u) = L'(s', u') = L(s' - zu', u'), \quad (11)$$

where  $z$  is the distance propagated. This is essentially just a shearing in  $(s, u)$  space.

Measuring the distance to a point in object space with a plenoptic camera is related to shifting the plane of the plenoptic function. Take the light field given by a plane  $(s, t)$  and a plane  $(u, v)$ . Limit to only one dimension on each plane,  $s$  and  $u$ . For a plenoptic camera,  $u$  is at the plane of the objective lens, and  $s$  is the plane of the MLA and an imaging system is formed based on the objective lens. The objective lens with focal length  $f$  will image objects according to the thin lens law  $1/f = 1/z_i + 1/z_o$ , where  $z_o$  is the distance from the lens to the object being imaged, and  $z_i$  is the distance behind the lens to which the object is imaged, which may not be the MLA plane. Knowing the focal length of the lens gives a relationship between  $s$  and  $u$ . The geometry is laid out in Figure 12. If the lens is focusing an object point to a point a distance  $z_i$  past  $u$  and  $z$  in front of  $s$  at plane  $x$ , two similar triangles are formed with their dimensions related by

$$\frac{s - x}{z} = \frac{x - u}{z_i},$$

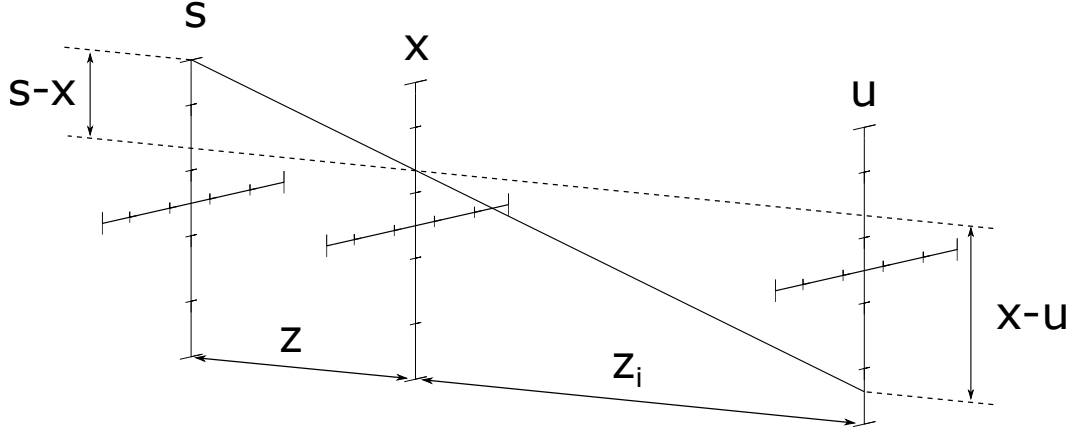


Figure 12. Given that the plane defined along  $u$  is the plane of a lens, then the ray from an imaged point will image to a known location between  $u$  and  $s$  based on the thin lens equation.  $z_i$  is the distance from the lens, and  $z$  is the distance from the sensor. The similar triangles shown, which become fixed based on the thin lens equation, define a relationship for  $u$  and  $s$ , which depends on the imaged point's distance from the objective.

where  $x$  is the location of the image point in the plane of the image. Solving this for  $s$  gives

$$s = x\left(1 + \frac{z}{z_i}\right) - u\frac{z}{z_i} = mu + x(1 - m), \quad (12)$$

where  $m = -\frac{z}{z_i}$ . The value of  $s$  is defined in terms of  $u$  and a position  $x$ . The value of  $x$  can be defined by a unique point on the  $s$  plane if the object point is not identified by  $x$  but by what it would be at plane  $s$  given  $u = 0$ . In two dimensions, this is the center of the circle of confusion on  $(s, t)$  for a point imaged a distance  $z$  in front of it at  $(x, y)$ . When  $u = 0$  then  $s = x(1 - m)$ . A point  $\mathfrak{s}$  on the plane  $s$  can then be defined as a point  $s$  related to the corresponding location in  $x$  and a location in  $u$ ,  $\mathfrak{s} = mu + s$ , where  $s$  and  $\mathfrak{s}$  are both points on the  $s$ -plane. This can all be done for the  $t$  and  $v$  directions as well giving  $\mathfrak{t} = mv + t$ . Hence the plenoptic function can be written as

$$L(\mathfrak{s}, \mathfrak{t}, u, v) = L(s + mu, t + mv, u, v) = L'(x, y, u, v), \quad (13)$$

where  $u$  and  $v$  are the same for both the  $L$  and  $L'$  fields. For a given point in object

space  $m, s$ , and  $t$  will be fixed. As the plenoptic function is varied over  $s$  and  $u$ , a given object will change its location along a line following  $\mathfrak{s} = s + mu$ . The slope will be determined by  $z$  and  $z_i$  which is in turn related to the object distance. This is how depth can be extracted from the plenoptic function. Objects which can be identified will create lines in the  $(\mathfrak{s}, u)$  and  $(\mathfrak{t}, v)$  planes in the data. These slopes can be used to find the distance to imaged objects.

Equation (11) and Equation (13) show the same thing, but in Equation (13), the shear is modified by the imaging system which makes the useful connection to the distance to the plane of the object in object space. Using the  $m$  scale factor also helps in relating images which can be created from the plenoptic function. Equation (10) shows how to create an image at the original  $(s, t)$  plane. The image can also be made at the new  $(s', t')$  plane related to the first by  $m$ . The image at the new plane is

$$I'(s', t') = \frac{1}{l'^2} \int_{u'} \int_{v'} L'(s', t', u', v') du' dv'. \quad (14)$$

In the literature [59] the shift from  $L$  to  $L'$  is related by  $\alpha$ , instead of  $m$ , which lets the distance between  $(s, t)$  and  $(u, v)$ ,  $l$ , be adjusted by a simple scale factor  $l' = \alpha l$ . The scale factor used here,  $m$ , is related to  $\alpha$  by  $m = 1 - 1/\alpha$ . Now the new image can be given in terms of  $L$  as was done in Equation (13) but with  $\alpha$  instead of  $m$ ,

$$I'(s', t') = I_\alpha(s, t) = \frac{1}{(\alpha l)^2} \int_u \int_v L(s + (1 - 1/\alpha)u, t + (1 - 1/\alpha)v, u, v) dudv. \quad (15)$$

With this formulation a light field  $L$  can be taken, and then images focused at different depths can be made by simply changing  $\alpha$  and integrating, creating what will be referred to as a standard image, either refocused or not depending on  $\alpha$ . This is because when the positions  $(u, v)$ , or angles, are integrated over, the resulting value of  $I$  for a given  $(s_0, t_0)$  is the same as if no angular information were present. Stan-

standard imaging systems work this way; all of the rays entering the objective at all the points/angles  $(u, v)$  focus onto a particular pixel  $(s_0, t_0)$  and are added together giving the total intensity. Looking at Figure 10 as an example, the blue and red points image onto the same micro lens and so in the standard image all of both of their rays will be added together for a single spatial value for that micro lens, while the rays from the green point will be part of the next pixel.

A second type of image can be made by selecting a particular  $(u_0, v_0)$ ,

$$\begin{aligned} I(s, t) &= \frac{1}{l^2} \int_u \int_v L(s, t, u, v) \delta(u - u_0, v - v_0) dudv \\ &= \frac{1}{l^2} L(s, t, u_0, v_0). \end{aligned}$$

This is a perspective view or image. It is effectively the image seen by placing an aperture at position  $(u_0, v_0)$  the size of a pixel imaged onto the objective plane. Changing  $(u_0, v_0)$  creates images with different perspectives.

Given ray optics and small enough micro lenses and sensor pixels, arbitrary resolution would be possible with this description, but diffraction is the ultimate limit in the resolution of any optical system. Given an  $f/2$  system, the diffraction-limited spot size of a point in object space is about  $2\mu\text{m}$ . Given a standard  $24\text{mm} \times \text{mm}$  sensor and  $2\mu\text{m}$ -wide pixels, the sensor resolution is 18,000 by 12,000. The trade off now comes in the size of the micro lenses. The size of the micro lens will determine the spatial resolution and the number of pixels which fit behind it will become the angular resolution.

### 3.3 Wave Front Sensing

Wave front sensing has applications when looking at how a plane wave propagates through a cloud of cold atoms, which will be discussed in Section 5.2. Eslami *et al.*

proposed arranging the objective lens and MLA in a third way (this is referred to as a plenoptic 3.0 camera) in order to measure the phase front of a plane wave [31]. In this system a 4f imaging system is set up, the MLA is placed behind the objective lens by their added focal lengths, and the sensor array is placed one focal length behind the MLA. The ability to measure phase front information from the incoming wave using this optical arrangement was demonstrated by Wu *et al.* [75, 74, 76]. Given a scalar wave with some amplitude and phase distribution  $t_1(x, y)$  entering the objective lens, they found the full scalar wave determined by Fourier optics at the sensor plane for this optical set up is given by

$$t_3(s, t) = \frac{1}{jf_2\lambda} \int \int \sum_{M,N} t_2(u, v) \text{rect} \left( \frac{s+u-2dM}{d} \right) \text{rect} \left( \frac{t+v-2dM}{d} \right) \times \exp \left\{ -j \frac{2\pi}{f_2\lambda} ((s-dM)(u-dM) + (t-dN)(v-dN)) \right\} dudv, \quad (16)$$

where  $f_2$  is the focal length of the micro lens,  $t_2$  is the scalar wave at the image side focal plane of the objective,  $d$  is the diameter of the micro lens and  $M$  and  $N$  are the indices for each micro lens. The resolution in phase tilt is determined by the micro lens array; that is, for a plane wave impinging on the objective lens, it will produce a unique signal in a micro lens if its phase is given by

$$t_1(x, y) \propto \exp(j2\pi d \frac{Mx + Ny}{\lambda f_1} + j\phi),$$

where  $f_1$  is the focal length of the objective. Each  $M$  and  $N$  will produce a signal in a different micro lens making the phase tilt distinguishable. The phase  $\phi$  will be lost, but  $\Delta\phi$  can be found if two waves have the same  $M$  and  $N$  values but different  $\phi$  phase shifts. The intensity measured behind a given micro lens for two plane waves with different amplitudes ( $A_1$  and  $A_2$ ) and a phase difference of  $\Delta\phi$  is given by [75]

as

$$I_3^{M,N}(s', t') \propto A_1^2 + A_2^2 + 2A_1A_2 \cos(\Delta u \cdot s' + \Delta v \cdot t' + \Delta\phi),$$

where  $\Delta u = u_2 - u_1$  and  $\Delta v = v_2 - v_1$ . Location  $(u_1, v_1)$  is where the delta function of the  $t_1$  plane wave with amplitude  $A_1$  is imaged on the Fourier plane, similarly for  $(u_2, v_2)$ . The primed coordinates are “local” coordinates associated with the given micro lens and are related to the global coordinates as

$$s' = s - Md, \quad t' = t - Nd. \quad (17)$$

As can be seen, the variation in the intensity depends on  $\Delta\phi$ , so it can be determined, however not past a  $2\pi$  phase shift. This can be exceeded when looking at the phase tilts.

### 3.4 Light Field Microscopy

Cold atom clouds are formed in sizes ranging from tens of microns to a few millimeters. A microscope system is typically used to image them. The use of micro lenses to capture angle as well as locations of light rays was applied to microscopy by a group at Stanford [46] in 2006. They called the modified microscope a light field microscope (LFM) and they developed the methods for recovering a three-dimensional (3D) volume from images taken with the LFM [46, 47, 14, 18]. The desire was to be able to create 3D images of microscopic structures and do so in a single exposure. This would be useful for imaging light-sensitive specimens and for looking at complicated structures such as neuron connections in brain tissue. This is also useful when performing absorption imaging of cold atoms where the cloud dissipates after one image.

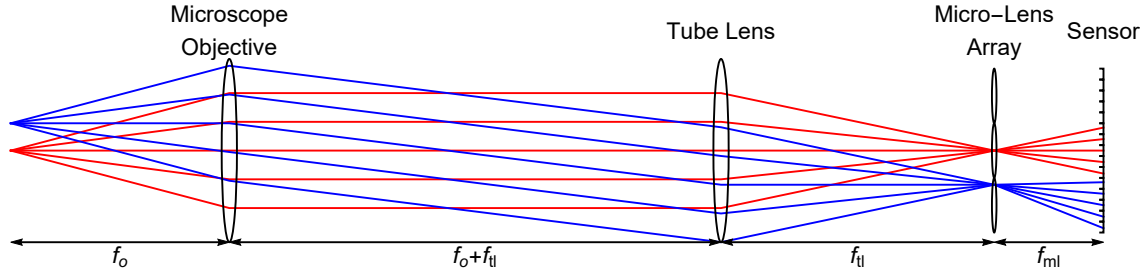


**Figure 13.** A model of a light field microscope's optics. The objective and tube lens are arranged as a typical microscope. The pair of lenses images onto the MLA followed by the sensor.  $f_{\{o,tl,ml\}}$  are the focal lengths of the objective, tube lens, and micro-lenses respectively.

The optics of a LFM are essentially the same as for a plenoptic camera, but there are a few important differences [46]; Figure 13 shows the basic layout for a tube-lens-based microscope. Microscopes are telecentric, wave optics are needed for modeling and resolution calculations, and the depth of field is very narrow. Due to the telecentric optics of the microscope, translating an object does not change the perspective as a standard imaging system would. Because of this the perspective views of a LFM are shifts in angle of orthographic projections, Figure 14 shows how rays at a given angle all image onto the same pixel location behind a micro lens. As far as the manipulation of the light field and how it is recorded, it is essentially the same as for the camera. Here, the focus will be on the resolution of the microscope, which is dependent on the depth of field of the system, and the process of extracting three-dimensional information from the image which depends on the PSF and hence the wave optics of the system.

### 3.4.1 Resolution and Axial Resolution.

The resolution of a LFM is primarily determined by the numerical aperture (NA) of the objective. The Nyquist sampling rate is the fundamental limit to resolution, which for a given objective is given by  $\lambda/(2NA)$ . This limit is closely related to the

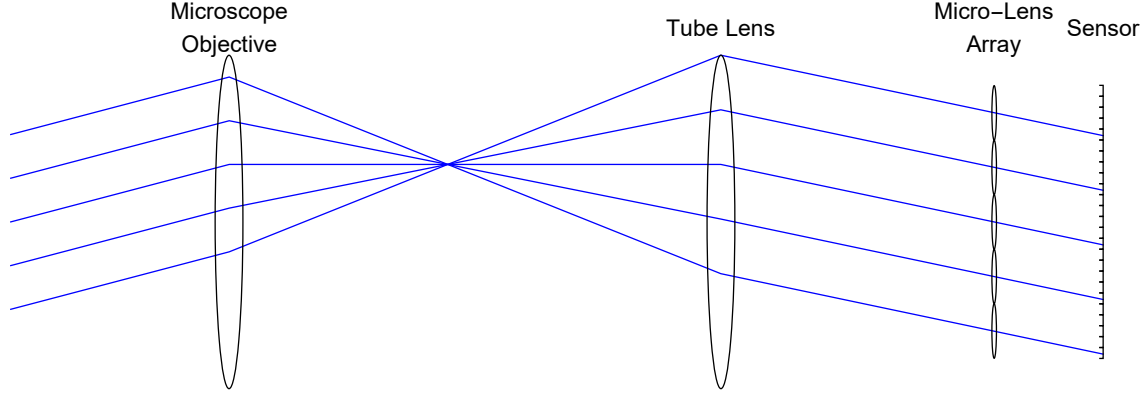


**Figure 14.** A ray trace of all rays entering the objective at the same angle. Each, based on location, image to the same  $(u, v)$  or pixel coordinate.

Sparrow limit, defined as the spacing between two points at which there is barely a measurable dip in image intensity, given by

$$R_{\text{obj}} = \frac{0.47\lambda}{\text{NA}} \mathcal{M}, \quad (18)$$

where  $\mathcal{M}$  is the magnification of the objective system [46].  $R_{\text{obj}}$  is the smallest spot size the optical system is capable of resolving.

The total resolution measurable by a LFM sensor is given by the number of micro lens  $N_s \times N_t$  times the number of pixels behind each lenslet  $N_u \times N_v$ , where each  $N$  represents the number of micro lenses or pixels in the given dimension. The total number of pixels in the 4D space of the plenoptic function is  $N_u \times N_v \times N_s \times N_t$ . The total is equal to the full pixel resolution of the sensor, the 4D data is tiled over the sensor in  $N_u \times N_v$  pixel blocks for each micro lens on the grid. When the f-number of the microscope objective is matched to the f-number of the micro lenses, the spot size of each imaging system will be the same. The number of pixels behind a micro lens should be at least the same as the number of resolvable spots. Using the Sparrow limit as the smallest reasonable size for a pixel,  $N_u \times N_v$  can be found in the following

relation

$$N_u \times N_v = \frac{W \times H}{R_{\text{obj}}^2}, \quad (19)$$

where  $W$  and  $H$  are the width and height of a micro lens, or in the case of a circular micro lens,  $W = H = D_{\text{ml}}$  where  $D_{\text{ml}}$  is the diameter of the micro lens. This gives the angular resolution of the system. Changing the micro lens diameter changes the angular resolution of the system and the spatial resolution, given by  $R_{\text{res}} = D_{\text{ml}}/\mathcal{M}$ . The total number of resolvable spots,  $N_u \times N_v \times N_s \times N_t$ , is fixed by the number of resolvable spots that fit in the area of the sensor, by adjusting the diameter of the micro lenses that resolution can be traded between angular resolution and spatial resolution as needed.

Axial resolution is very important for three-dimensional imaging. It is determined by the depth of field. There are three different depths of field based on which elements of the LFM optical system are considered. First, is the microscope by itself. If the pixels of the sensor are small enough to not limit resolution, the depth of field is given by

$$D_{\text{tot}_1} \approx \frac{\lambda n}{NA^2}, \quad (20)$$

where  $n$  is the index of refraction in the medium before the microscope objective, which is typically air.

In case two, the micro lenses are added, and the pixel sizes are now effectively the micro lens size [46]. Assuming  $N_u = N_v$  the depth of field becomes

$$D_{\text{tot}_2} \approx \frac{(2 + N_u)\lambda n}{2NA^2}. \quad (21)$$

In case three, consider a single pixel behind a micro lens [46]. By restricting the set of rays to only those that can reach the pixel, the depth of field is increased by a

factor of  $N_u$  giving

$$D_{\text{tot}_3} \approx \frac{(2 + N_u^2)\lambda n}{2NA^2}. \quad (22)$$

$D_{\text{tot}_3}$  gives the largest depth of field and is the range over which the light field microscope can refocus and maintain a spatial resolution equal to  $R_{res}$ .  $D_{\text{tot}_2}$  is the depth of field for standard images created by refocusing the plenoptic field. Given that  $D_{\text{tot}_2}$  is effectively  $D_{\text{tot}_3}$  divided by  $N_u$ ,  $N_u$  gives the number of fully distinct layers to which one can refocus and have resolution match the resolution of the micro lenses. These properties in terms of resolution and depth of field are the tools to determine the best 3D volume in which a LFM can image.

### 3.4.2 The Point Spread Function and Deconvolution.

One of the great capabilities of the light field camera is to refocus the image after taking it as shown in Section 3.2 and this still applies to the light field microscope. Refocusing is related to how microscopists have been constructing 3D images for some time [4]. Strong microscopes have very narrow depths of focus thanks to the resolving power. If an object has much depth then a microscope image will only show part of the full object in focus. Moving the object up and down shifts the location of the focal plane on the object and one can start to create in-focus slices of the 3D object. A series of images can be taken and combined to get a full 3D image. Each slice suffers from the parts of the object that are out of focus; they still contribute light to the image but it is blurred, obstructing a clear view of the in-focus slice. Microscopists developed the technique of taking several slice images along with a point spread function (PSF) representing the blurring along the optical axis [65]. The PSF describes how light from a point source in the object space of the microscope gets transferred to the image plane. In general if  $o(x, y, z)$  is a function describing the distribution of light radiating from an object of interest in scalar wave

form, then the image formed by the microscope system is the convolution of  $o$  with the PSF given by  $h(x, y, z)$

$$I(x', y', z'_i) = |o(x, y, z) * h(x, y, z)|^2,$$

where  $I$  is the intensity measured,  $(x', y', z')$  are coordinates in image space,  $(x, y, z)$  are coordinates in object space,  $z'_i$  is the image plane, and  $*$  is the 3D convolution operator. A given plane in object space  $z$  is mapped to  $z'_i$  via the thin lens equation  $1/f = 1/z'_i + 1/z$ . Given a series of images taken at different depths  $z'_i$ , the distribution of the object  $o$  can be determined by a deconvolution using  $h$ .

Levoy *et al.* [46] saw that with a plenoptic system this series of images focused at different slices could be created from a single plenoptic image. In this case the refocused images are all created synthetically from a plenoptic image, and the PSF is created by imaging a point-like source and again synthetically refocusing. Refocusing to different depths in a plenoptic image will produce images with out-of-focus light in them. The deconvolution works to remove this light giving a more accurate picture of a particular slice of the image. Doing this at each slice creates a good 3D image of the volume. Levoy's group then improved on this method by creating a PSF based off of a wave optics model [14]. The wave optics model is used to capture a 3D image of trapped cold atoms.

A deconvolution utilizing the PSF is used to perform the inverse operation needed to recover an original volume imaged by a LFM. The Richardson-Lucy deconvolution method for a LFM is developed in [14]. A model is used to produce an accurate PSF to describe the transfer of light from the 3D volume being imaged to the 2D sensor array. This can be represented as an operator,  $H$ , operating on a vector,  $\mathbf{g}$ , which represents points in a volume being imaged. The resulting vector,  $\mathbf{f}$ , represents the

pixels on the sensor,

$$\mathbf{f} = H\mathbf{g}. \quad (23)$$

$H$  is determined by making a model of the PSF, first as a continuous function then discretizing to make  $H$ . This model can be determined using an FFT method for propagating the light through the system, described in detail in [18]. A more accurate model can be made using analytical PSFs for the objective optics as developed in *Advanced Optical Imaging Theory* by Min Gu [37], and discussed in [14] for LFM; the propagation of the wave through the MLA and to the sensor is still done using FFT methods. The analytical model is slower to calculate on a computer compared to the FFT-based model, but it is more accurate and is used here and described in the following.

When dealing with incoherent imaging the imaged intensity of each point is added together to form the image of the volume. In this case an intensity-based PSF can be used. The PSF is given by

$$|h(\mathbf{x}, \mathbf{p})|^2 = \left| \mathcal{F}^{-1} \left\{ \mathcal{F} \{ \Phi(\mathbf{x}) U_i(\mathbf{x}, \mathbf{p}) \} \exp \left[ -\frac{i}{4\pi} \lambda f_{ml} (\omega_s^2 + \omega_t^2) \right] \right\} \right|^2, \quad (24)$$

where  $\mathbf{x}$  is the  $(s, t)$  position on the sensor,  $\mathbf{p}$  is the point in three-dimensional object space from which the radiance is coming (this PSF is not shift invariant),  $f_{ml}$  is the focal length of a micro lens, and  $\omega_s$  and  $\omega_t$  are the spatial frequencies in the  $s$  and  $t$  dimensions.  $U_i(\mathbf{x}, \mathbf{p})$  is the wave front at the micro lens array coming from a point source at  $\mathbf{p}$  in object space and is effectively the complex wave PSF of the objective system that is imaging onto the MLA.  $\Phi(\mathbf{x})$  is the phase contributed to the wave front by the MLA. The exponential and inverse Fourier transform give the propagation from the micro lenses to the sensor using the Fresnel propagator [36].

The light field recorded,  $f(\mathbf{x})$ , is produced from some 3D distribution of sources,  $g(\mathbf{p})$ , by linear superposition with the PSF,

$$f(\mathbf{x}) = \int |h(\mathbf{x}, \mathbf{p})|^2 g(\mathbf{p}) d\mathbf{p}. \quad (25)$$

This is the continuous version of Equation (23) where the elements of the matrix  $\mathbf{H}$  are given by

$$h_{ij} = \int_{a_j} \int_{v_i} w_i(\mathbf{p}) |h(\mathbf{x}, \mathbf{p})|^2 d\mathbf{p} d\mathbf{x}, \quad (26)$$

and  $a_j$  is the area of a pixel  $j$ ,  $v_i$  is the volume of a voxel  $i$  in  $g(\mathbf{p})$ , and  $w_i(\mathbf{p})$  is a weighting factor to avoid aliasing.  $H$  must first be determined in order to try to solve for the volume  $\mathbf{g}$  given an image  $\mathbf{f}$ .

### The Point Spread Function.

$h(\mathbf{x}, \mathbf{p})$  depends primarily on  $U_i$ , the PSF of the combined microscope objective lens and the tube lens. Determining  $U_i$  is done following the development in Gu for a 3D scalar wave PSF. The geometry of the optical system is shown in Figure 15, where the objective lens and tube lens are considered a single thin lens [37].

In a thin lens optical system the image and object planes are distances  $d_{10}$  and  $d_{20}$  on either side of the lens such that  $1/f = 1/d_{10} + 1/d_{20}$ . If depth information is needed, as is the case for a 3D PSF, shifts along the  $z_1$  and  $z_3$  axis need to be added, giving  $d_1$  and  $d_2$  defined as

$$d_1 = d_{10} - z_1,$$

$$d_2 = d_{20} + z_3,$$

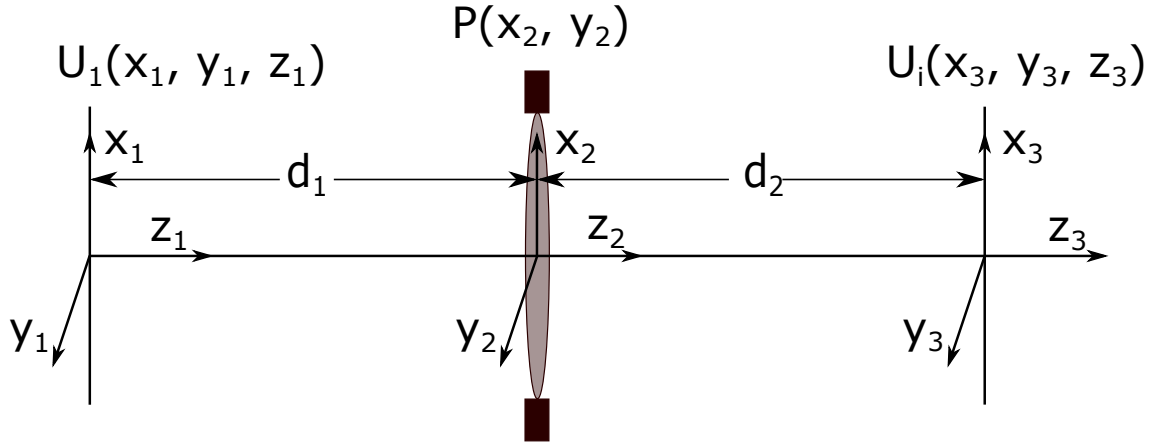


Figure 15. The geometric relation between the different coordinates used in calculating the point spread function. In the generalized case for a 3D scalar field  $U_1$ , the resulting object and image planes will be  $d_1$  and  $d_2$  away from the lens such that  $\frac{1}{f} \neq \frac{1}{d_1} + \frac{1}{d_2}$ .

where

$$\frac{1}{f} \neq \frac{1}{d_1} + \frac{1}{d_2}.$$

If this is the case, then from Gu, the PSF of a thin lens is expressed explicitly as

$$h'(x, y) = \iint_{-\infty}^{\infty} P(x_2, y_2) \exp \left[ -\frac{ik}{2} \left( \frac{1}{f} - \frac{1}{d_1} - \frac{1}{d_2} \right) (x_2^2 + y_2^2) \right] \exp \left[ \frac{ik}{d_1} (x_2 x + y_2 y) \right] dx_2 dy_2. \quad (27)$$

where the apodization function of the lens is  $P(x_2, y_2)$ , and  $k = 2\pi/\lambda$ . Assuming the following holds true

$$\frac{1}{d_1} = \frac{1}{d_{10} - z_1} \approx \frac{1}{d_{10}} \left( 1 + \frac{z_1}{d_{10}} \right), \quad (28)$$

$$\frac{1}{d_2} = \frac{1}{d_{20} - z_3} \approx \frac{1}{d_{20}} \left( 1 + \frac{z_3}{d_{20}} \right), \quad (29)$$

then

$$\frac{1}{f} - \frac{1}{d_1} - \frac{1}{d_2} \approx -\frac{1}{d_{10}^2}(z_1 - M^2 z_3), \quad (30)$$

where  $M = d_{10}/d_{20}$ . This gives a PSF of

$$h'(x, y) = \iint_{-\infty}^{\infty} P(x_2, y_2) \exp \left[ -\frac{ik}{2} \left( -\frac{1}{d_{10}^2}(z_1 - M^2 z_3) \right) (x_2^2 + y_2^2) \right] \exp \left[ \frac{ik}{d_1}(x_2 x + y_2 y) \right] dx_2 dy_2. \quad (31)$$

This PSF can then be used to find the scalar wave at the image plane,  $U_i$ , by convolving  $h'$  with the object,  $o(x_1, y_1)$ , taking into account the scaling caused by magnification.  $U_i$  is given by Gu as

$$U_i(x_3, y_3) = \frac{M \exp[-ik(d_1 + d_2)]}{d_1^2 \lambda^2} \exp \left[ -\frac{ikM}{2d_{10}}(x_3^2 + y_3^2)(1 + M) \right] \times \iiint_{-\infty}^{\infty} P(x_2, y_2) o(x_1, y_1) \exp \left[ -\frac{ik}{2} \left( \frac{1}{d_{10}} \right)^2 (z_1 - M^2 z_3)(x_2^2 + y_2^2) \right] \times \exp \left\{ \frac{ik}{d_{10}} [x_2(x_1 + Mx_3) + y_2(y_1 + My_3)] \right\} dx_1 dy_1 dx_2 dy_2. \quad (32)$$

The additional phase terms are a result of the Fresnel propagation to and from the lens. Using the Born approximation, which assumes secondary diffraction and scattering in the volume do not occur and the object is semi-transparent,  $U_i$  can be extended for an object which has depth,  $o(x_1, y_1, z_1)$ , by integrating over  $z_1$  giving

$$\begin{aligned}
U_i(x_3, y_3, z_3) = & \frac{M \exp[-ik(d_{10} + d_{20})]}{d_1^2 \lambda^2} \exp \left[ -\frac{ikM}{2d_{10}} (x_3^2 + y_3^2)(1 + M) \right] \\
& \times \int \cdots \int_{-\infty}^{\infty} P(x_2, y_2) o(x_1, y_1, z_1) \exp[ik(z_1 - z_3)] \\
& \times \exp \left[ -\frac{ik}{2} \left( \frac{1}{d_{10}} \right)^2 (z_1 - M^2 z_3)(x_2^2 + y_2^2) \right] \\
& \times \exp \left\{ \frac{ik}{d_{10}} [x_2(x_1 + Mx_3) + y_2(y_1 + My_3)] \right\} dx_1 dy_1 dz_1 dx_2 dy_2. \quad (33)
\end{aligned}$$

If  $o(x_1, y_1, z_1) = \delta(x_1 - a)\delta(y_1 - b)\delta(z_1 - c)$ , this will represent the field from a point  $\mathbf{p} = (a, b, c)$ . The result is a three-dimensional field in image space. The MLA is at  $z_3 = 0$ . Using these substitutions  $U_i$  will be in terms of  $\mathbf{x} = (x_3, y_3)$  and  $\mathbf{p}$  as in Equation (24)

$$\begin{aligned}
U_i(\mathbf{x}, \mathbf{p}) = & \frac{M \exp[-ik(d_{10} + d_{20})]}{d_1^2 \lambda^2} \exp \left[ -\frac{ikM}{2d_{10}} |\mathbf{x}|^2 (1 + M) \right] \\
& \times \int_{-\infty}^{\infty} \int_{-\infty}^{\infty} P(x_2, y_2) \exp[ikz_1] \exp \left[ -\frac{ik}{2} \left( \frac{1}{d_{10}} \right)^2 c(x_2^2 + y_2^2) \right] \\
& \times \exp \left\{ \frac{ik}{d_{10}} [x_2(a + Mx_3) + y_2(b + My_3)] \right\} dx_2 dy_2. \quad (34)
\end{aligned}$$

$U_i$  can be simplified further by letting  $o(x_1, y_1, z_1) = \delta(x_1)\delta(y_1)\delta(z_1)$ , a point source at the origin. This will make  $U_i$  more general and useful for calculating  $H$ .  $U_i$  becomes

$$\begin{aligned}
U_i(x_3, y_3, z_3) = & \frac{M \exp[-ik(d_{10} + d_{20})]}{d_1^2 \lambda^2} \exp \left[ -\frac{ikM}{2d_{10}} (x_3^2 + y_3^2)(1 + M) \right] \\
& \times \exp[-ikz_3] \iint_{-\infty}^{\infty} P(x_2, y_2) \exp \left[ \frac{ik}{2} \left( \frac{1}{d_{10}} \right)^2 M^2 z_3 (x_2^2 + y_2^2) \right] \\
& \times \exp \left\{ \frac{ik}{d_{10}} [x_2(Mx_3) + y_2(My_3)] \right\} dx_2 dy_2. \quad (35)
\end{aligned}$$

Converting to polar coordinates

$$x_2 = r_2 \cos \theta$$

$$y_2 = r_2 \sin \theta$$

and

$$\frac{Mx_3}{\lambda d_{10}} = l \cos \Psi$$

$$\frac{My_3}{\lambda d_{10}} = l \sin \Psi$$

and assuming  $P(x_2, y_2)$  is radially symmetric and has an aperture of radius  $a$ , then using the Hankel transform

$$\begin{aligned} U_i(x_3, y_3, z_3) &= \frac{M \exp[-ik(d_{10} + d_{20})]}{d_1^2 \lambda^2} \exp \left[ -\frac{ikM}{2d_{10}} (x_3^2 + y_3^2)(1 + M) \right] \exp[-ikz_3] \\ &\quad \times \int_0^{2\pi} \int_0^\infty P(r_2) \exp \left[ \frac{ik}{2} \left( \frac{1}{d_{10}} \right)^2 M^2 z_3 r_2^2 \right] \exp \{2\pi i r_2 l \cos(\theta - \Psi)\} r_2 dr_2 d\theta \end{aligned} \quad (36)$$

$$\begin{aligned} &= \frac{M \exp[-ik(d_{10} + d_{20})]}{d_1^2 \lambda^2} \exp \left[ -\frac{ikM}{2d_{10}} (x_3^2 + y_3^2)(1 + M) \right] \exp[-ikz_3] \\ &\quad \times \int_0^a P(r_2) \exp \left[ \frac{ik}{2} \left( \frac{1}{d_{10}} \right)^2 M^2 z_3 r_2^2 \right] 2\pi J_0(2\pi r_2 l) r_2 dr_2. \end{aligned} \quad (37)$$

Next, using  $r_3 = \sqrt{x_3^2 + y_3^2}$  and substituting  $\rho = r_2/a$  then

$$\begin{aligned} U_i(x_3, y_3, z_3) &= \frac{M \exp[-ik(d_{10} + d_{20})]}{d_1^2 \lambda^2} \exp \left[ -\frac{ikM}{2d_{10}} r_3^2 (1 + M) \right] \exp[-ikz_3] \\ &\quad \times \int_0^1 P(a\rho) \exp \left[ \frac{ik}{2} \left( \frac{1}{d_{10}} \right)^2 M^2 z_3 a^2 \rho^2 \right] J_0(2\pi a\rho \frac{M}{\lambda d_{10}} r_3) a^2 2\pi \rho d\rho. \end{aligned} \quad (38)$$

The constant phase term  $\exp[-ik(d_{10} + d_{20})]$  can be dropped. The image space coordinates,  $(x_3, y_3, z_3)$  are changed to  $(v, u)$  based on the NA and  $M$  of the system as follows,

$$\text{NA} = n \sin(\alpha_o) = \frac{1}{M} n \sin(\alpha_i), \quad (39)$$

$$v = \frac{2\pi}{\lambda} r_3 \frac{a}{d_{20}} \approx \frac{2\pi}{\lambda} r_3 \sin(\alpha_i), \quad (40)$$

$$u = \frac{2\pi}{\lambda} z_3 \frac{a^2}{d_{20}^2} \approx \frac{8\pi}{\lambda} z_3 \sin^2\left(\frac{\alpha_i}{2}\right), \quad (41)$$

where  $\alpha_o$  and  $\alpha_i$  are the acceptance angles of the objective in object and image space. Finally, with the removal of the constant  $a^2$  term to match Gu,  $U_i$  is given by

$$U_i(v, u) = \frac{M \exp\left(-\frac{iu}{4\sin^2(\alpha_i/2)}\right)}{d_1^2 \lambda^2} \exp\left[-\frac{iv^2}{4N}(1+M)\right] \times \int_0^1 P(\rho) \exp\left(\frac{iu}{2}\rho^2\right) J_0(\rho v) 2\pi \rho d\rho, \quad (42)$$

where  $J_0$  is the zeroth-order Bessel function of the first kind and  $N = \frac{\pi a^2}{\lambda d_{20}}$ .

$U_i$  is the 3D scalar wave in image space. The constant  $\frac{M}{d_1^2 \lambda^2}$  simply scales the magnitude based on the distance propagated. The phase terms outside of the integral account for the phase accumulation from propagation and depend on the axial and radial location of the wave at the image plane. The first is the small changes right around the focal plane and only depend on  $u$ , the second accounts for propagation in the Fresnel approximation both to the lens and to the image plane. The integral describes the diffraction and focusing of the wave due to the lens and pupil function  $P$ . The integral of the Bessel function describes the Airy disk created from a circular aperture. The added  $u$ -dependent phase term describes the de-focus phase shift induced by shifting off of the focal plane.

Equation (42) gives  $U_i$  from Equation (24), for the specific case of  $\mathbf{p} = (0, 0, 0)$ . The 2D scalar wave at the MLA is  $U_i(v, 0)$ , matching the dimensions of  $U_i$  from Equation (24). The wave then passes through the MLA and on to the sensor as shown in Equation (24). This produces the PSF for a point at the origin in the object-space volume. To create the full  $H$  matrix, the PSF needs to be calculated for every value in  $g$  representing voxels of some finite size in the full volume being imaged.  $U_i$  of Equation (42) is space-invariant and can be used to calculate any of the values  $h_{ij}$ , but the wave still has to be propagated through the MLA for each  $i$ , which is not space-invariant. However the MLA is periodic. If it is a square lattice, then  $h$  at a given point  $\mathbf{p}_0 = (x, y, z)$  will be the same as  $h$  at  $\mathbf{p}_1 = (x + \eta D_{\text{ml}}/\mathcal{M}, y + \nu D_{\text{ml}}/\mathcal{M}, z)$  up to a translation on the sensor of  $(\eta D_{\text{ml}}, \nu D_{\text{ml}})$ , where  $\eta$  and  $\nu$  are indices indicating the location of a micro lens on the grid where  $(\eta, \nu) = (0, 0)$  is in the center. This reduces the number of  $h_{ij}$  values that need to be calculated. In practice just those along an axial column in  $z$  are calculated and then the shift is applied to create the full  $H$ .

### Richardson-Lucy Deconvolution.

Now that  $H$  can be determined analytically, a volume can be reconstructed from a recorded image  $\mathbf{f}$  by solving for  $\mathbf{g}$  in Equation (23). The transfer matrix  $H$  is in general not invertible, so Equation (23) cannot be directly solved for  $\mathbf{g}$ . The volume is approximated iteratively using the Richardson-Lucy deconvolution following this process

$$\mathbf{g}^{(k+1)} = \text{diag}(H^T \mathbf{1})^{-1} \text{diag}(H^T \text{diag}(H \mathbf{g}^{(k)} + \mathbf{b})^{-1} \mathbf{f}) \mathbf{g}^{(k)} \quad (43)$$

where  $\mathbf{b}$  accounts for background noise and the  $\text{diag}(\cdot)$  operator returns a matrix with the argument on the diagonal and zeros elsewhere [14].

This equation takes a first guess at the volume  $\mathbf{g}^{(k)}$ , which can be a volume of ones, a single point in the volume, or a volume based on a focal stack.  $g^{(k)}$  is projected onto the sensor using the PSF,  $\mathbf{f}' = H\mathbf{g}^{(k)}$ , and the vector  $\mathbf{b}$  representing background noise is added.  $\mathbf{f}'$  is then compared to  $\mathbf{f}$ , the image taken. A value in the image is divided by the corresponding value determined from the predicted volume,  $\mathbf{f}'' = (\mathbf{f}_1/\mathbf{f}'_1, \dots)^T$ . The result is a vector with values that are one if the values are the same as the measured picture, greater than one if  $\mathbf{f}'_i < \mathbf{f}_i$ , and less than one if  $\mathbf{f}'_i > \mathbf{f}_i$ .  $\mathbf{f}''$  is then multiplied by the transpose of  $H$ . This is effectively a back projection of the scaled values back into the volume. That is, the values for a given pixel (a particular value in  $\mathbf{f}''$ ) are spread into the volume as a weighted distribution to each voxel (a particular value in  $\mathbf{g}$ ) based on the amount of light each voxel contributes to a total value of one on the pixel. Hence if a particular value of  $\mathbf{f}''$  is less than one, a reduced value is projected into the volume, and if it is greater than one, an amplified value is projected. This is normalized against back projecting all ones into the volume, and the result reduces or increases the value in a particular voxel based on the comparison to the image recorded. As the projected volume approaches the values of the recorded image, the updates approach one and converge toward the answer. The back projection step is where the evidence of lost information along the optical axis becomes apparent. This is discussed further in the Chapter IV as it can be clearly seen when reconstructing images. It is also closely related to tomography, about which more details can be found in Appendix A.

Using the LFM described above, along with modeling the PSF described here, this Richardson-Lucy deconvolution was done on images of fluorescing rubidium atoms cooled in a MOT. The description of the processing of the images, and analysis of the resulting 3D volumes is discussed next.

## IV. Three Dimensional Fluorescence Imaging of Trapped Cold Atoms with a Light Field Microscope

This chapter demonstrates the capability to reconstruct volumetric information of a cold atom cloud utilizing a light field microscope (LFM), greatly increasing the information that can be gathered about the atom cloud when a single camera is used. The design considerations and optical system accuracies important to understanding the technique are discussed.

The LFM was first applied to dilute atomic clouds by Sakmann and Kasevich in 2014 [64]. They showed 3D structure in a cross pattern of fluorescing rubidium created by crossing laser beams passing through a dilute rubidium gas. They created a simple set-up with a standard camera, a micro lens array (MLA,) a microscope objective and some relay optics. Two lasers were shot through a chamber of rubidium gas which then fluoresces for imaging. The lasers had different angles and crossed through the  $z$  dimension as well as the  $x, y$  plane of the imaging system. They used a 3D deconvolution to create a stack of in-focus images at known depths. This is taken a step farther in this research, a Lytro® Development Kit MLA and sensor are used in combination with a low-magnification microscope objective to create a LFM which is used to image a 3D cloud of cold rubidium atoms in a MOT. The wave optics model PSF is then used to reconstruct a 3D image of the cloud of atoms.

The optics of the LFM used will be presented first, then the images taken and reconstructed 3D volumes will be shown and compared to reference images. The errors affecting the measurements are discussed, then the effect of a phase term in the point spread function (PSF) model on the reconstructions is shown. The locations of the atom clouds measured from the 3D reconstructions with respect to the relative locations of a shifting focal plane is presented. Lastly the trade space of the LFM

optical system is looked at for different uses, and how atom number calculations used in atom interferometry could be made with these 3D images.

#### 4.1 The Light Field Microscope

As discussed in Section 3.4, the imaging capabilities of the LFM depend primarily on the numerical aperture (NA) and the magnification of the objective. The LFM was built to utilize the Lytro® Development Kit MLA sensor and work with the MOT system described in Section 2.3, requiring a long working distance objective. Additionally the atom cloud's size was on the order of a millimeter so reconstruction depth at that order was desired. The optical system was designed based on these considerations.

The optics system was a Mitutoyo Plan Apo NIR Infinity Corrected microscope objective with a NA of 0.26, a focal length of  $f_o = 20.0\text{mm}$ , a working distance of 30.5mm, and a tube lens with a focal length of  $f_{tl} = 25\text{mm}$  giving a magnification of  $\mathcal{M} = f_{tl}/f_o = 1.25$ . The micro-lenses were  $f/2$  lenses,  $20\mu\text{m}$  in diameter, with approximately 14 pixels behind each micro-lens. This is summarized in Table 1, and Figure 16 is a picture of the camera.

There were two main assumptions made in determining the PSF in Chapter III which need to be checked now that the optical system has been determined. Both are

**Table 1. Optical System Details**

Property	Value
Objective NA	0.26
Objective focal length	$20\text{mm}$
Tube Lens focal length	$25\text{mm}$
Magnification	1.25
Micro-Lens $f/\#$	2
Micro-Lens diameter	$20\mu\text{m}$

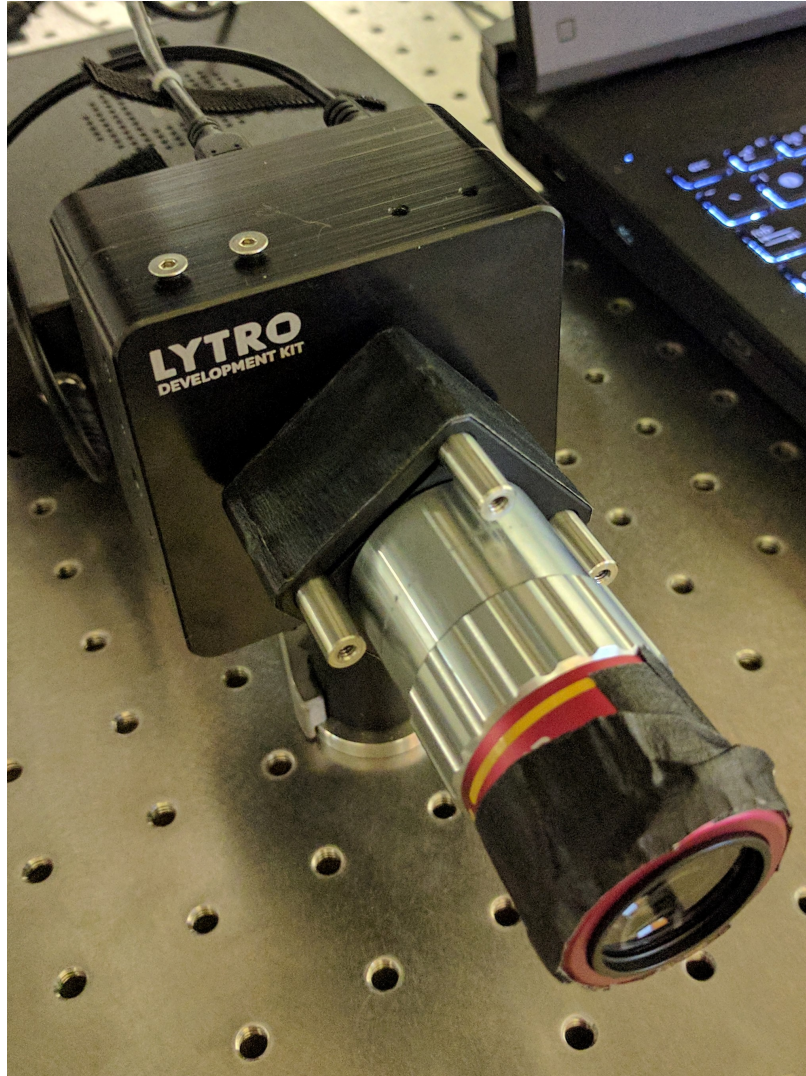


Figure 16. The light field microscope used to take the images of the atom clouds. The Lytro® Development Kit sensor is in the body of the camera. The optics attached were put together for the MOT described in Chapter II. Here the Mitutoyo Plan Apo NIR Infinity Corrected Objective with a Numerical Aperture (NA) of 0.26 is being used. It could be switched out for a NA= 0.14 objective, but only a few pictures were taken with the lower NA objective.

good approximations when dealing with lower NA systems  $NA < 0.5$  with standard magnifications on the order of  $10\times$ , but this system is has a lower magnification. The first is from Equation (29), and checks the approximation made in the distances to the object and image plane. It still holds for the system used in this work where the distances  $d_{10}$  and  $d_{20}$  are the focal lengths of the objective and tube lens respectively,

$$d_{10} = 20\text{mm},$$

$$d_{20} = 25\text{mm},$$

$$-1.5\text{mm} \leq z_1, z_3 \leq 1.5\text{mm},$$

then the ratio of the exact value to the approximation is equal to within a percent

$$\frac{1/(d_{10} - z)}{(1 + z/d_{10})/d_{10}} = 1.006 \quad \text{for } z = 1.5\text{mm},$$

$$\frac{1/(d_{20} + z)}{(1 - z/d_{20})/d_{20}} = 1.004 \quad \text{for } z = 1.5\text{mm}.$$

The second assumption is that  $N \gg v_3^2/4$ , in which case the phase term,  $\exp\left[-\frac{iv_3^2}{4N}(1 + M)\right]$ , from Equation (42) is dropped. The actual values are

$$v_3^2/4 = \left(\frac{2\pi a}{\lambda d_{20}}\right)^2 r_3^2/4 \approx 1.5 \times 10^6 \text{m}^2 \quad \text{for } r_{3\text{max}} = 1.5 \times 10^{-3} \text{m}^2,$$

$$N = \frac{\pi a}{\lambda d_{20}} \approx 4.3 \times 10^3 \text{m}^2,$$

where  $a = 5.2\text{mm}$  and  $\lambda = 780\text{nm}$ . Clearly  $N \not\gg v_3^2/4$ . Typically with greater magnification, the range of  $r_3$  values would be smaller and  $d_{20}$  would be larger than those for this system. As this is not the case here this phase was included in the PSF calculations. The impact of this phase is looked at further in Section 4.5.

The resolution properties of the system can now be determined as well. Using the Sparrow limit,  $R_{\text{obj}}$ , and the number of resolvable spots behind a micro-lens (along one dimension),  $N_u$ , for this system is

$$R_{\text{obj}} = \frac{0.47\lambda}{NA} \mathcal{M} = 1.76\mu\text{m}, \quad (44)$$

$$N_u = \frac{D_{\text{ml}}}{R_{\text{obj}}} \approx 11, \quad (45)$$

where  $D_{\text{ml}} = 20\mu\text{m}$ . The eleven resolvable spots ensure the optical system is not limited by pixel resolution. The spatial resolution is

$$R_{\text{res}} = \frac{D_{\text{ml}}}{\mathcal{M}} = 16\mu\text{m}.$$

The ideal depth of the reconstructed volume is given by the full depth of field ( $D_{\text{tot}_3}$ ), the depth of field for a sub-aperture image, given by

$$D_{\text{tot}_3} \approx \frac{(2 + N_u^2)\lambda n}{2NA^2} \approx 750\mu\text{m}. \quad (46)$$

The reconstruction is not limited to this region but the lateral,  $(x, y)$ , resolution falls off as the distance from the focal plane increases. The depth-dependent band limit (in cycles/ $m$ ), derived in [14], is given by

$$\nu(z) = \frac{D_{\text{ml}}}{0.94\lambda\mathcal{M}|z|} \quad (47)$$

for values of  $|z| \geq D_{\text{ml}}^2/(2\mathcal{M}^2\lambda)$ . The band limit drops to a resolution of  $R_{\text{res}} \approx 70\mu\text{m}$  at  $z = \pm 1.5\text{mm}$ , the furthest extent of the deconvolved volume done here.

A notable difference in this system when compared to the LFM systems of the Stanford group [46, 14] is the magnification. The magnification of this system is about one, where typical LFMs have a magnification of at least  $20\times$ . The LFM used here

takes advantage of the MLA sensor from the Lytro® Development Kit. This comes with the constraint of  $f/\#$  matching the microscope optics to that of the micro-lenses, which limits the degree of magnification possible. In this system, a low magnification was desired because the size of the atom clouds was on the order of a millimeter. A low magnification system was also looked at by Mignard in [51]. They used a first-generation Lytro® camera, including its objective lens system, in combination with a microscope objective, and worked in what they refer to as the Inverse Regime, where a virtual image is viewed by the Lytro® objective. Here, because a standard objective did not need to be used, the magnification could be adjusted directly using the tube lens of the microscope system. This reduced the complexity of the LFM implemented here; their emphasis was a direct use of the Lytro® camera off the shelf.

## 4.2 Image Collection and Calibration

Using the LFM just described and a reference camera, plenoptic and reference images were taken for three different MOT atom clouds. All have the same structure with slight differences day to day in the MOT properties. Two images were taken for each MOT. One was taken with the atoms present and a second was taken without the atoms. The atoms were removed by switching off the magnetic field, letting the atoms escape from the trap but leaving all the background light scattered from the trapping laser beams. For each MOT, three plenoptic pictures were taken in succession, giving a total of 18 images, six for each of the three MOTs. Only one atom and background image were taken with the reference camera for each MOT.

The exposure of the plenoptic camera was adjusted for each MOT to get good images, resulting in exposures of 2, 4, and 3 seconds for MOT One, MOT Two and MOT Three, respectively. The long exposures resulted in an averaging of the atoms'

fluorescing intensity which did oscillate at a rate faster than 1Hz. The measured intensity can be used for calculations of the number of atoms in a cloud which will be discussed in Section 4.8, but it was not important for looking at the 3D structure of the cloud and the first applications of such a 3D imaging system. Additionally the plenoptic camera has a Bayer [8] color pattern on it so the raw data for each image was taken and demosaiced using OpenCV [13] and then converted to gray scale.

The images without atoms were subtracted from the respective paired image with atoms to remove background light from the images. This produced a certain amount of noise in the dark areas of the images as the background light was not exactly the same, which was aggravated by the long exposure times. This was alleviated in the reconstruction process by Gaussian smoothing the plenoptic data with a 4D Gaussian. The Gaussian had a different standard deviation for each dimension, taking into account total length of the spatial and angular dimensions, where the standard deviation was equal to or less than 1 pixel. The added noise was still apparent, particularly in those planes near the focal plane where the reconstruction suffers from the most artifacts [14].

The raw data from the plenoptic camera is a normal rectangular grid of data but has a hexagon pattern of micro lenses on top of it. Figure 17 shows an image of MOT One after background subtraction and being cropped, but before processing the plenoptic data; the MLA pattern can be seen in the inset. All the pixels behind a given micro lens need to be labeled with respect to the position of that micro lens and converted to a 4D block of data in order to perform the deconvolution. Determining how to break up the pixel data and create a 4D block is done based off of a calibration image. The calibration image is a picture taken with a diffuse light source filling the field of view. A bright, consistently lit image is produced with the micro lens pattern clearly visible. It is used in a calibration process to find the centers of the micro

lenses with respect to the pixel grid coordinates. The micro lenses are given their own grid label and the positions of the micro lens centers are calculated to sub pixel accuracy. The grid of the pixels is warped and re-sampled to put a pixel in the center of each micro lens. Using the center pixel as the center point for a circle with the radius of the micro lens, the pixels behind a micro lens are determined and associated with their respective micro lens position. An interpolation is done to change the micro lens hex grid to a square grid by shifting every other line of micro lenses half a micro lens over. Also in the hex grid, the centers of the micro lenses more closely spaced in one direction (in this case vertically) than in the other by  $\sin(\pi/3)$ , so the columns are down sampled to match the spacing of the rows (simply the diameter of the micro lens). This calibration provides the mapping needed to take any image on the same set of pixels to a 4D grid of spatial and angular information tiled in 2D. Also, part of the calibration is accounting for how the intensity is distributed over the sensor and compensates for imbalances in the distribution of the light on the pixels, for example vignetting. The intensity calibration is used to adjust the modeled point spread function's intensity and the overall intensity. The calibration provides a mapping from the raw pixel data to the desired 4D plenoptic data that can then be applied to each MOT image on a time scale of about a second depending on the size of the image and the speed of the computer.

The calibration and deconvolution code was created by the Stanford Light Field Microscope Project and was used with permission [46, 14, 18] with some modification. The hex grid transformation was based off open source MATLAB code created by D. Dansereau [23, 22].

After the calibration process, based on the desired depth of the reconstruction, the code creates the necessary PSFs needed for the transfer function  $H$ . This is done once and can take several hours depending on the size and resolution of the volume

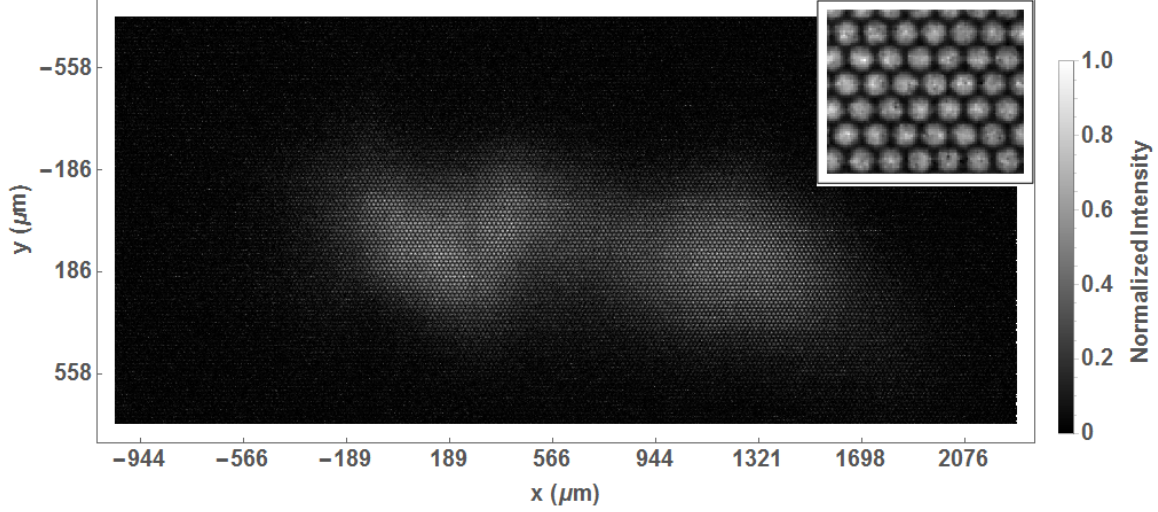


**Figure 17.** The raw plenoptic camera data after cropping and the background has been subtracted. The inset highlights the pattern produced on the sensor by the micro-lens array.

to be reconstructed. Once this is done, the saved PSFs can be quickly used in the Richardson-Lucy deconvolution.

### 4.3 3D Reconstructions

The Richardson-Lucy deconvolution was performed on the images following the process described in Section 3.4.2 with Equation (43). Each volume reconstruction done here was iterated 15 times; beyond this, there was little improvement of the residual norm. Figure 17 is the plenoptic data of MOT One operated on by the deconvolution. Figure 18 shows a contour surface of the deconvolved volume with an axial depth of 3mm and resolution of  $\approx 77\mu\text{m}$ . The images of all 3 MOT clouds and their reconstructions are presented in Appendix C.

In order to analyze the accuracy of the reconstructed 3D volume and the axial spreading observed, a reference image was taken of each MOT studied. Figure 19 represents the approximate orientations of the plenoptic camera and the reference image with respect to the vacuum chamber.

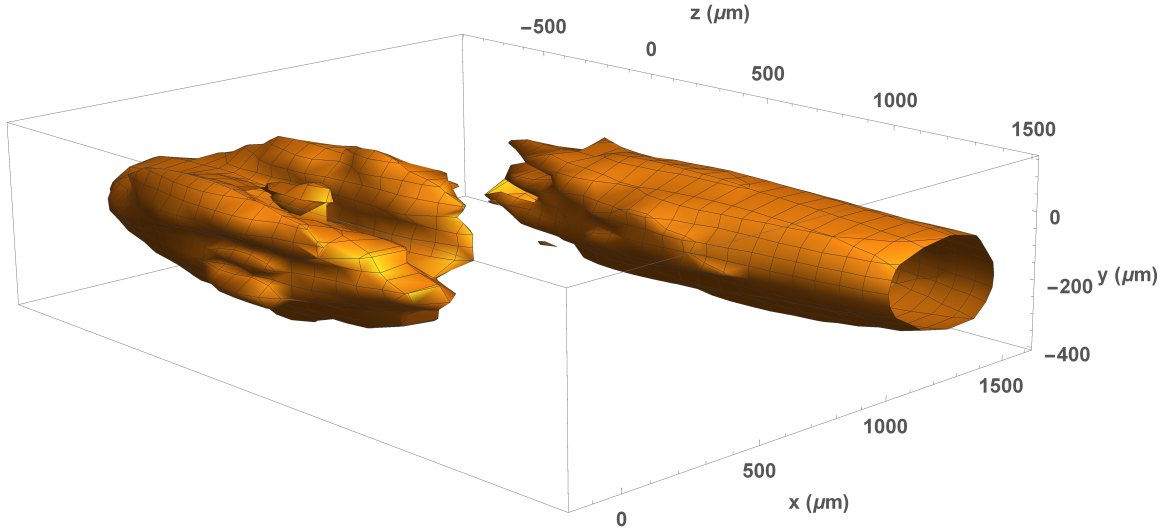


**Figure 18.** A contour surface through the normalized deconvolved volume at 0.44 voxel intensity produced from the plenoptic data in Figure 17. The elongation effect is noticeable and is why part of one of the clouds extends out of the volume.

The deconvolution attempts to assign to the voxels in the volume the amount of light coming from only that voxel. In order to compare the deconvolved volume data to the reference image, a projection image was made from the 3D volume. The angle of the projection was based off of the physical location and angle of the reference camera assuming the optical axis of the reference camera was in a single  $xy$ -plane of the volume data.

The projection image was made using a Radon transform [27]. Each depth slice of the 3D volume was taken as a 2D  $(x, y)$  image and then Radon transformed at the angle of the reference camera. Each transform at a given depth was a line in the final 2D  $(z, x)$  projection of the volume at an angle matching the reference camera. Figure 20 shows the projected image and the corresponding reference image for MOT One, where the axes have been labeled to match the plenoptic volume coordinates, but the  $(z, x)$  translation has not been accounted for. The  $z$ -axis shift in the centers of the two atom clouds can be seen in both.

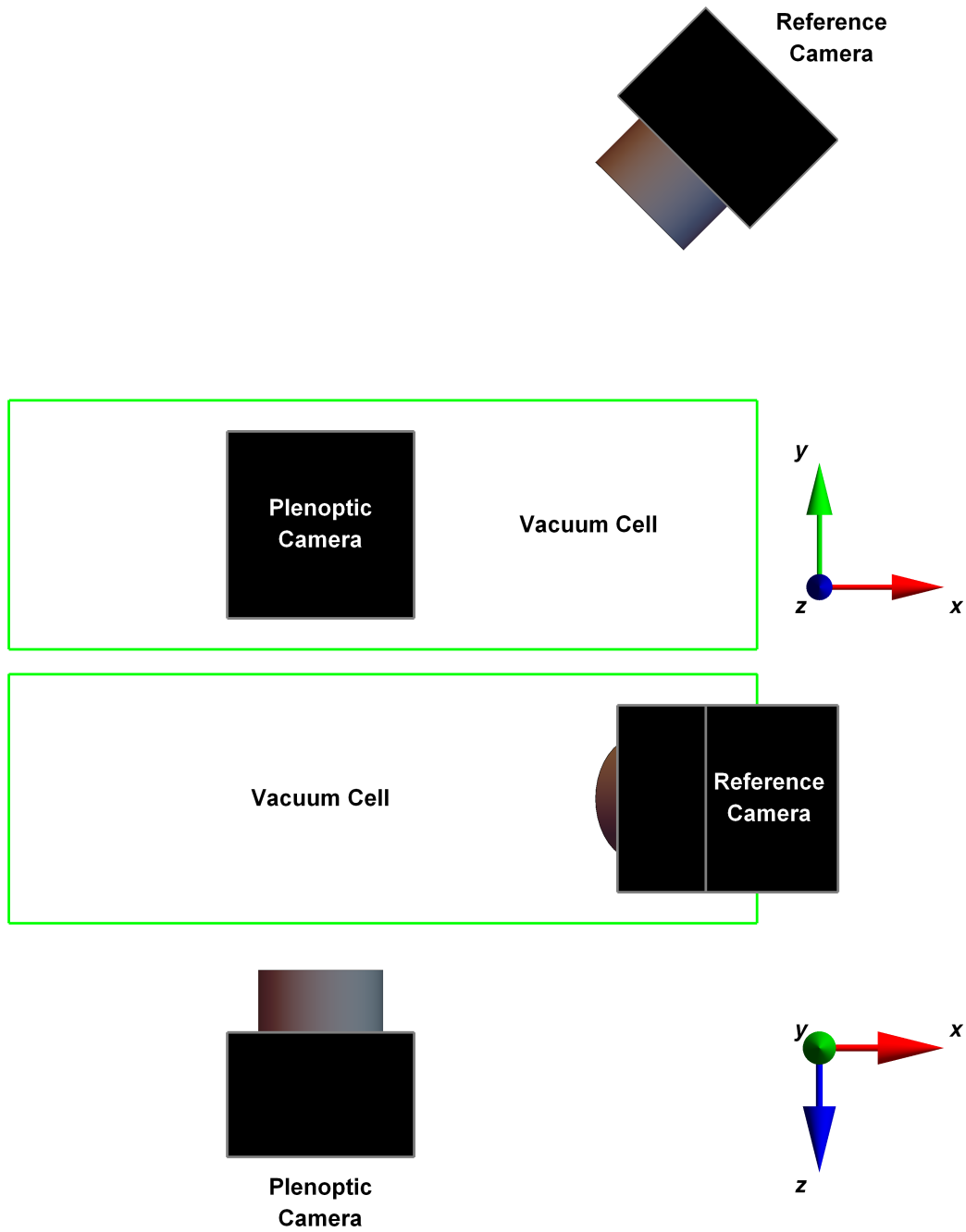


Figure 19. A model of the placement of the plenoptic camera (LFM) and the reference camera with respect to the vacuum chamber. Also shows the coordinate system of the 3D image reconstructions.

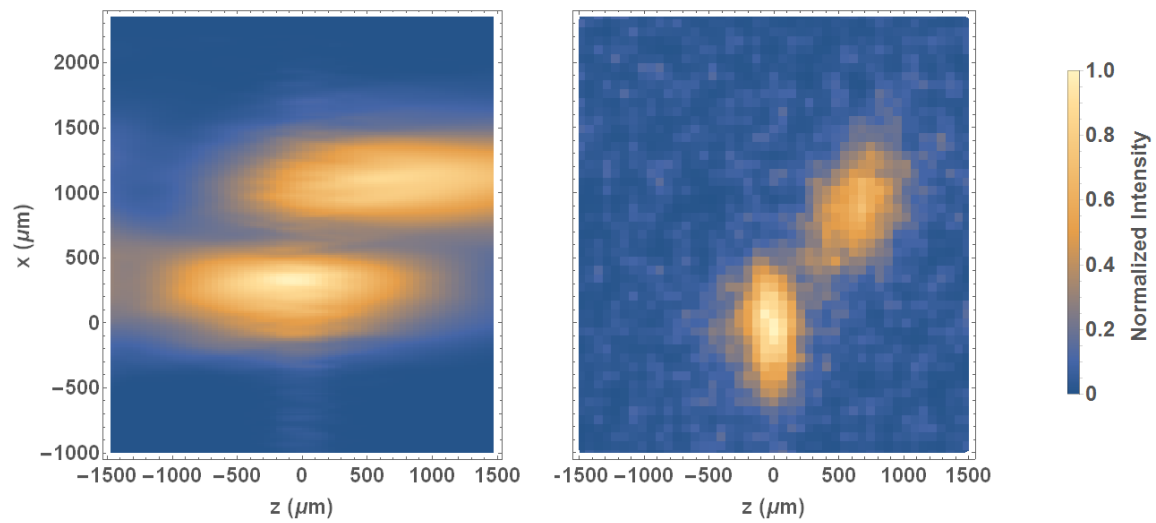


Figure 20. The left image is the projected image created from doing a Radon transform on each  $z$  slice in the reconstructed volume at the angle of the reference image. The right image is the reference image taken at an orthogonal view to the plenoptic camera. Both have been scaled and plotted over the same range for comparison. Translation shifts have not been removed.

The projections were compared to the reference images by looking at the relative locations of the two intensity peaks. The clouds do not have well defined edges and the peak intensities are at the center. These clouds are not expected to strictly follow a Gaussian distribution as discussed in Section 2.2, but the centers of the two peaks were most consistently and accurately found by fitting two 2D Gaussians to the intensity data. First, a threshold was set in the image based on the maximum intensity in order to create two regions around each peak separated by zeros. These two areas could then be identified as connected components by image processing software and the intensity-weighted centroids of each region calculated. These estimations of the centers were used as initial guesses for a fit of two 2D Gaussians to the data. The centers of the fitted Gaussians provided the locations of the atom cloud centers. The relative distance between the peaks was found simply by subtracting one from the other.

As mentioned in Section 4.1, the resolution of reconstructed depth slices degrades for planes farther from the focal plane. This makes the data look smoother. In contrast, planes at  $z$  depths inside the bounds  $|z| \geq D_{\text{ml}}^2/(2\mathcal{M}^2\lambda)$  (see Equation (47)) suffer from reconstruction artifacts during the deconvolution [14]. These planes have been replaced with interpolated data. The planes within the depth of field and beyond the region suffering from reconstruction artifacts are at the highest resolution. In order to account for the changing uncertainty with respect to depth, depth-dependent weights were added when fitting the 2D Gaussians to the data.

The mean values of the peak's axial separation for each MOT were calculated from the three images taken of each. The results are shown in Table 2. The separation between the two peaks is correct within error for all three peaks except in the case of MOT One. This is the only case where the reconstruction of the shifted peak was affected by edge effects (shown in Figure 21). The two atom clouds are the furthest

apart and one is centered on the volume. Because of this, the intensity of the second peak does not drop off before the edge of the reconstruction volume is reached (see Figure 18). Near the edge of the volume, the reconstructed intensity is artificially increased. This caused the fitted Gaussian to be pulled toward the edge.

### 4.3.1 Optical Axis Spreading from Back Projection.

There is clear spreading along the optical axis in the reconstruction shown in Figure 20. And it does not correspond to the depth of field of the LFM, which is the measure of the optical axis resolution of the system. The optical axis spreading is a result of the limited angular data in the plenoptic images and the back projection used to reconstruct the volume in the Richardson-Lucy deconvolution.

The plenoptic data of a perspective view is the orthographic projection of the volume in the direction associated with angle  $(u, v)$ . The deconvolution uses the projections from all the angles collected by the plenoptic image and back projects them into the volume to try to reconstruct where the light came from. This concept is related to tomography which is discussed in Appendix A. Figure 22 shows the overlapping back projections created from orthographic projections of a solid green bar for a limited number of angles. Each of the back projections is simply a path through the 2D volume with a width and angle determined by the orthographic projection of the bar at the corresponding angle. The orthographic projection of the bar along the optical axis will be a line the length of the bar, a projection  $90^\circ$  off the

**Table 2. The calculated relative separation of the two atom clouds in the projected image and reference image.**

Image	Projected Reconstruction (z,x $\mu\text{m}$ )	Reference (z,x $\mu\text{m}$ )
MOT One	(890 $\pm$ 100,820 $\pm$ 100)	(680 $\pm$ 30,930 $\pm$ 30)
MOT Two	(370 $\pm$ 90,620 $\pm$ 50)	(430 $\pm$ 10,640 $\pm$ 10)
MOT Three	(360 $\pm$ 90,590 $\pm$ 50)	(460 $\pm$ 10,560 $\pm$ 10)

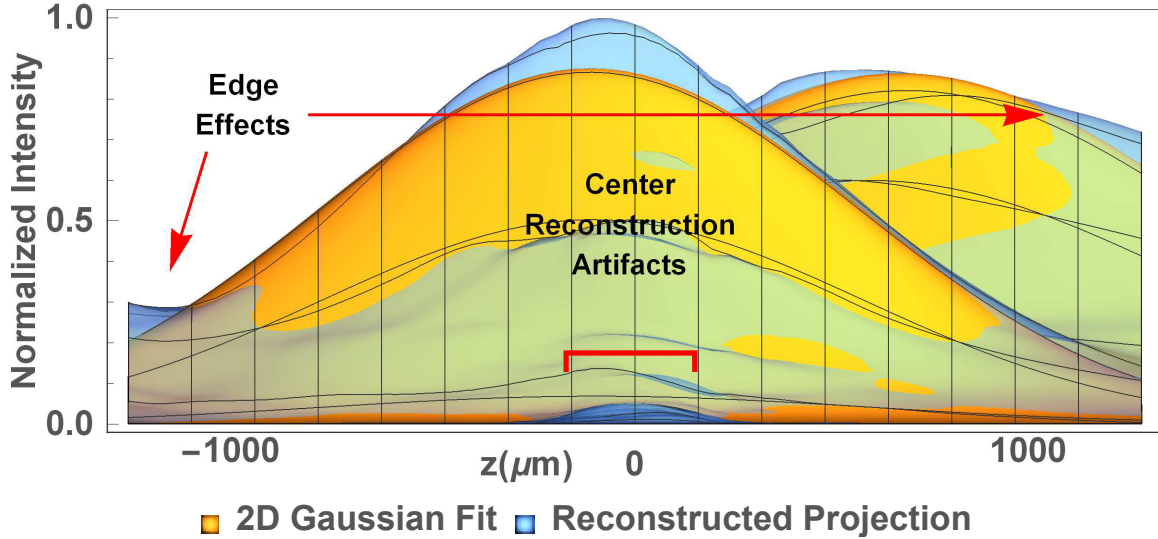


**Figure 21.** There are two major areas where reconstruction artifacts effect the projection image data. The first is  $z$ -axis positions near the focal plane ( $z = 0$ ). As discussed in the text, this creates increases in intensity. The second is edge effects; near the  $z$ -axis edges of the volume, the intensity tends to increase. This is MOT One data.

optical axis will be a line the width of the bar. Those areas where only some of the back projections overlap likely do not contribute to the original 2D shape, but the areas where all overlap could have contributed to the shape, given the information available from the limited angles of the projections. A ray of light passing by the “edge” of the line creates the edge of a triangle and will cross the center along the optical axis at  $l = b/2 \tan(\pi/2 - \alpha_0)$  where  $b$  is the length of the base of the triangle in Figure 22. The full volume is being estimated based on the back projections and sees this effect forward and back so the optical axis spreading is  $2l$  for a spreading factor of  $\tan(\pi/2 - \alpha_0)$ . This principle and geometry was used to check if the optical axis spreading observed is simply a result of this back projection and predict the optical axis spreading.

The effective  $b$  for the image of the atom cloud was determined using a standard image created from the plenoptic data with no refocusing. The peak intensity was found and the two peaks separated by thresholding the intensity values at as close

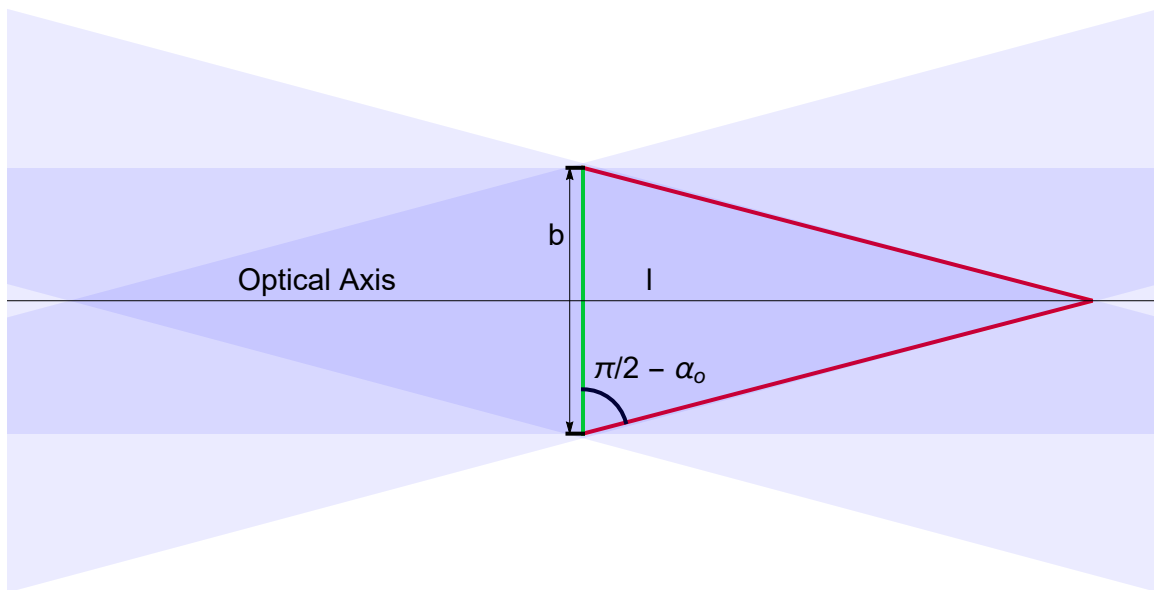


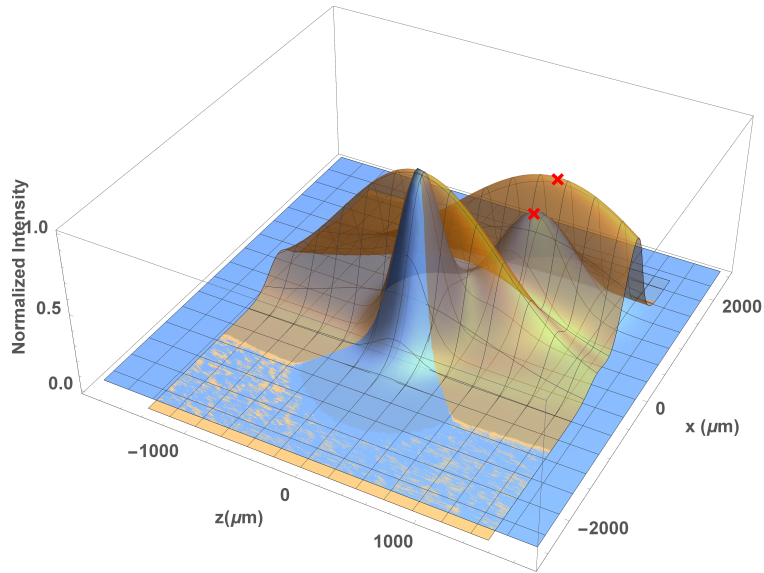
Figure 22. Pictorially shows how the back projection estimation of optical axis spreading depends on the acceptance angle  $\alpha_0$  of the objective NA and the width  $b$  of the object,  $l = b/2 \tan(\pi/2 - \alpha_0)$ . The shades of color show the overlapping of back projections of the line at a several different angles. The darkest triangle is where they all overlap and there is no data from the projections to suggest that there should not be part of the original object filling that portion of the plane.

to half the maximum as possible while still creating two distinguishable peaks. The intensity-weighted centroids were found and an ellipse fit to the resulting regions. The minor axis of the fitted ellipse was scaled, if necessary, to approximate the narrowest full width at half maximum (FWHM) across the atom cloud for each peak, and this determined the base of the triangle, or the narrowest part of the cloud that had to be looked around by the different angled projections.  $\alpha_0 = 15^\circ$  was given by the NA of the objective.

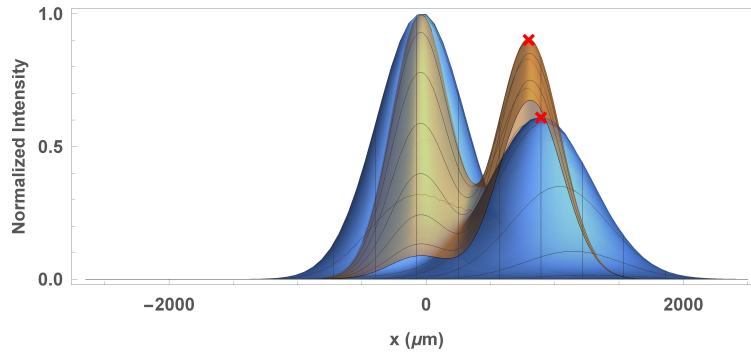
Table 3 presents the optical axis spreading of the data compared to calculated predictions. The  $z$ -axis spreading of the reconstructed image was determined using the 2D Gaussian fit values for the width,  $\sigma$ , to calculate the FWHM along the  $z$ -axis. Figure 23 shows the Gaussian fits of the projected and reference image of MOT One plotted together, with the center peak of the projection Gaussian shifted to match that of the reference.

The predicted length of MOT Three Peak 2 shows the greatest discrepancy. The stretching of the fit is because of the reconstruction artifacts near the center of the volume. An example is shown in Figure 24. In the case of MOT Three, the two atom clouds are closer together. Peak 1 is nearly centered and Peak 2 is just off center; it also has a much lower peak intensity. The result is the reconstruction noise broadens the fitted Gaussian.

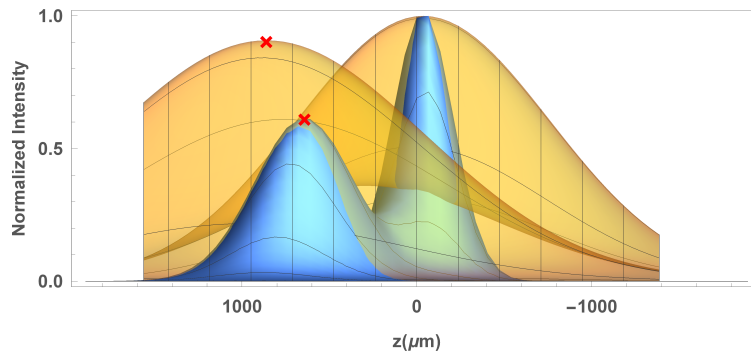
This optical axis spreading does limit the ability to see an object directly behind another. If the two peaks shown in Figure 20 were in line along the optical axis, they would be spread over each other and they could not be identified. This will need to be taken into account for any application to a similar system.



(a)



(b)



(c)

Figure 23. Shown are the two 2D Gaussians fit to the projected image (Orange) and the reference image (Blue) where Peak 1 (the more intense peak) of the projected image has been shifted to the same location as Peak 1 of the reference image. Shifting shows the relative locations of the second peak for both images, indicated by the red  $\times$ . The plot is in 3D with respect to normalized intensity.

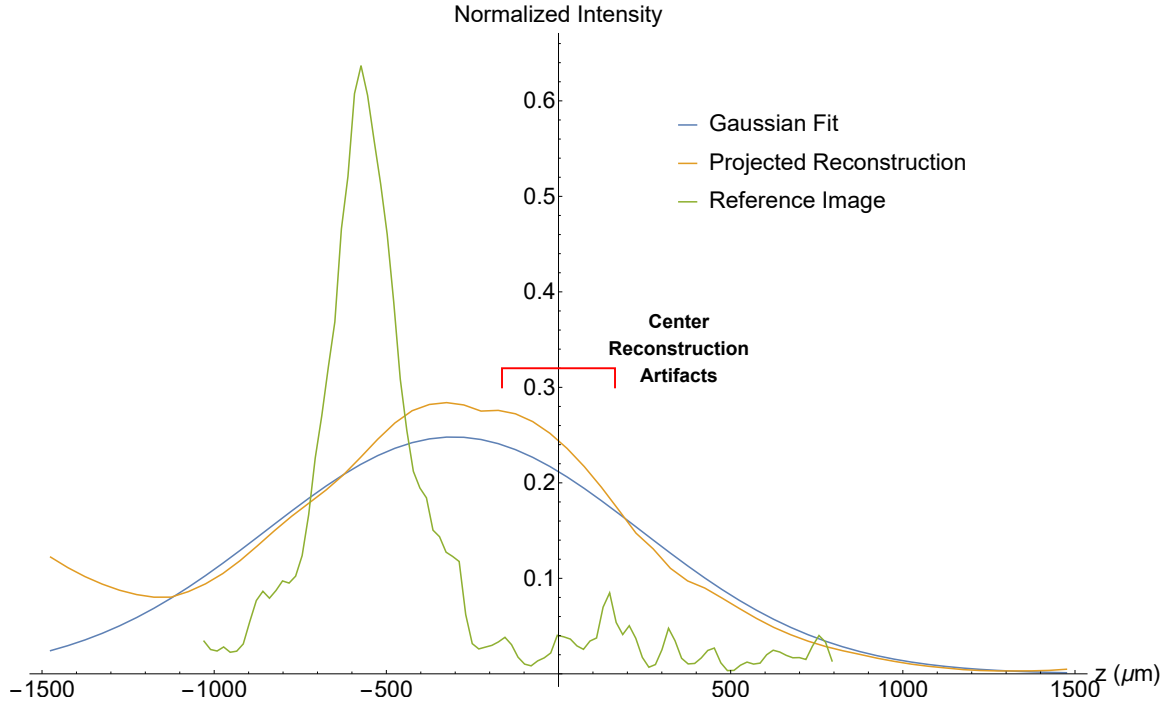


Figure 24. A single line along the  $z$ -axis is plotted of the Gaussian fit to the projected reconstruction data of MOT Three and the reference image. The line goes through the Peak 2. The reference image has a different intensity scaling than the plenoptic data and shows that the peak is behind the focal plane and is narrow. The center reconstruction artifacts result in raising the value of the projected reconstruction near the center and broadening the peak, increasing the measured optical axis spreading beyond that of the back projection spreading and also shifting the estimated axial location toward the center.

Table 3. The calculated lengths of the peaks along the optical axis and back-projection based estimations of the optical axis lengths given the minor axis of an ellipse fit to the FWHM data of the standard on-axis image of the atoms.

Image and Peak	Projected Image Optical Axis Length ( $\mu\text{m}$ )	Back-projection Based Estimate of Optical Axis Length ( $\mu\text{m}$ )
MOT One: Peak 1	$1960 \pm 140$	$1950 \pm 60$
MOT One: Peak 2	$1950 \pm 140$	$1850 \pm 60$
MOT Two: Peak 1	$1360 \pm 130$	$1270 \pm 60$
MOT Two: Peak 2	$1190 \pm 130$	$1090 \pm 60$
MOT Three: Peak 1	$1200 \pm 130$	$1210 \pm 60$
MOT Three: Peak 2	$1250 \pm 130$	$860 \pm 60$

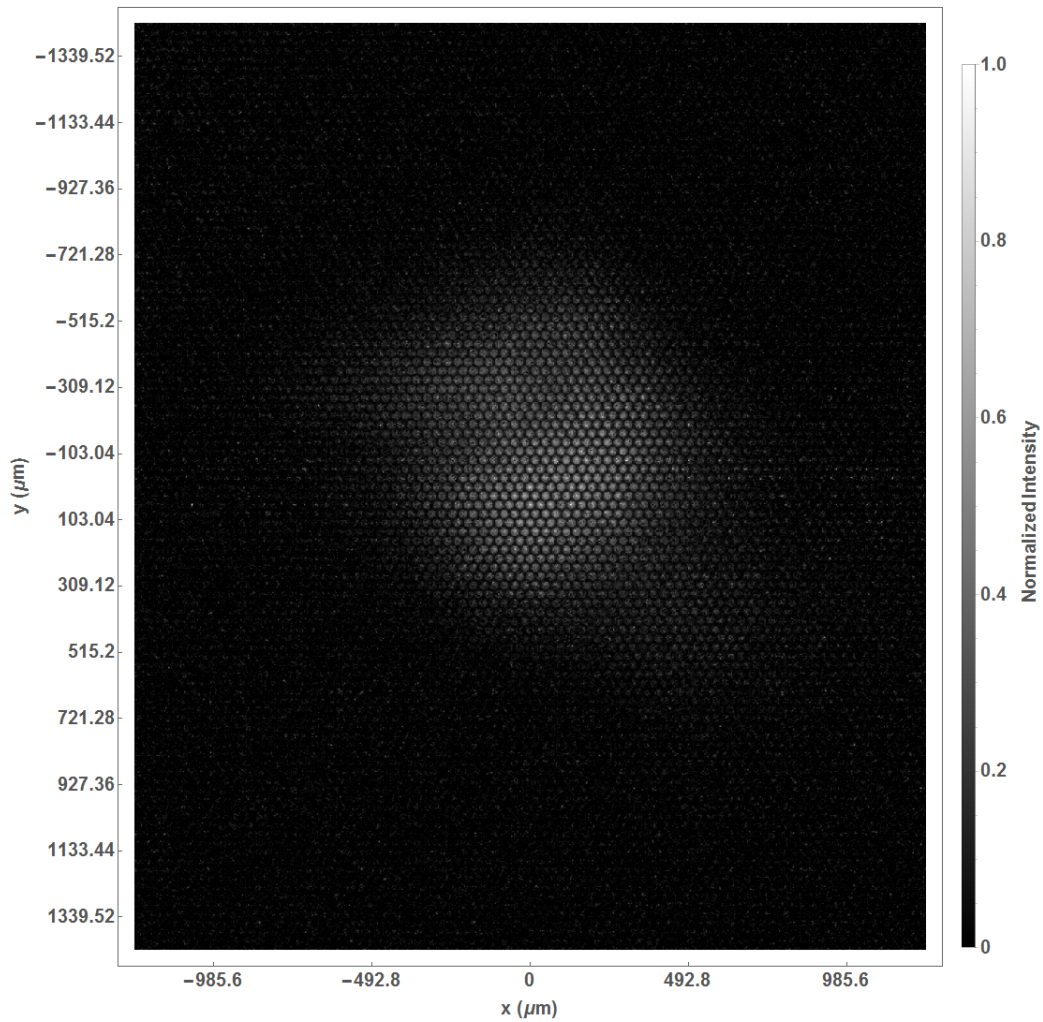


Figure 25. The raw plenoptic camera data after cropping and the background has been subtracted of a single small atom cloud taken with a 0.14 NA objective LFM. The the cloud is about about 0.7mm wide.

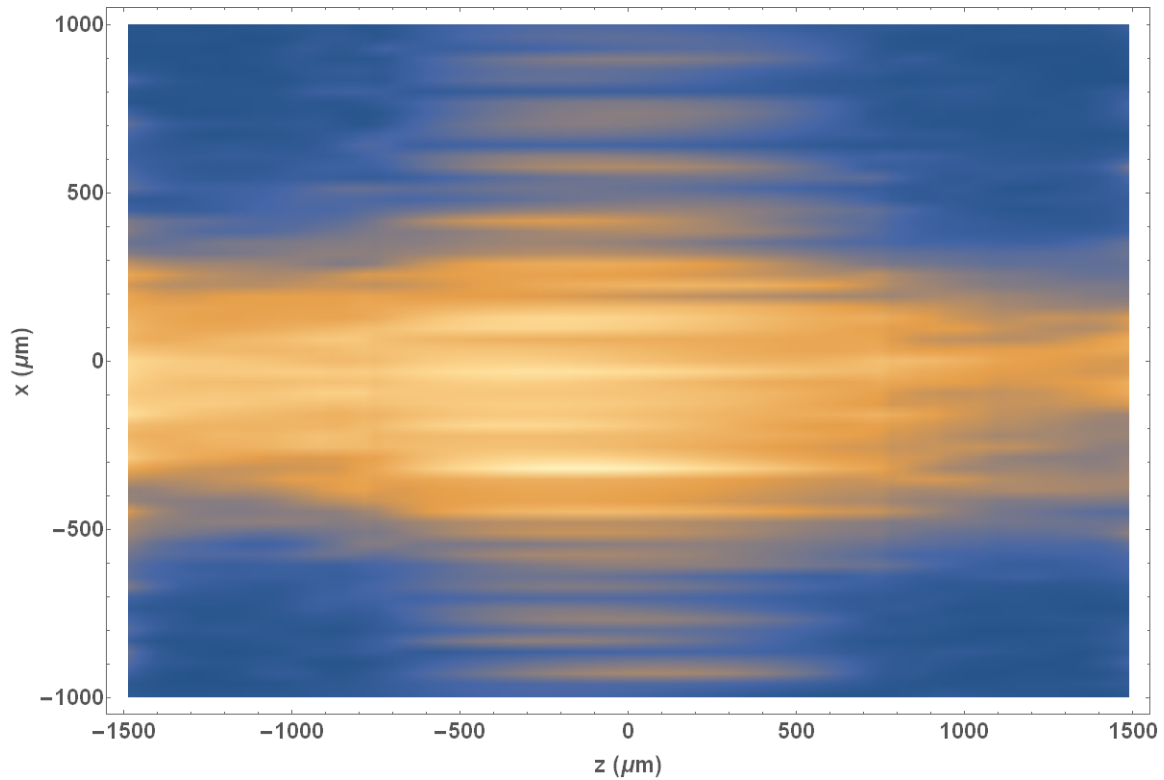
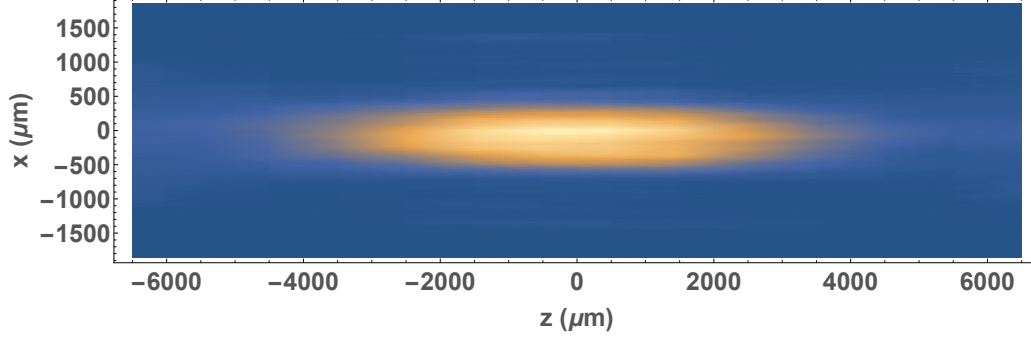


Figure 26. The projected data of the 0.14 NA objective LFM for a 34mm deep volume reconstruction. It is clear here that the extent of the atoms in the z-direction is not accurate as it spreads across the entire 3mm but is less than a millimeter in diameter based on the plenoptic image in Figure 25.

### 4.3.2 Back Projection Spreading Comparison to $NA = 0.14$ Objective and Modeled Ellipse.

A few pictures were taken using a 0.14 NA objective on the LFM, which was the same optical set-up, swapping out the 0.26 NA objective, but because of the even smaller NA, the back projection spreading was significantly worse. Figure 25 shows the background subtracted plenoptic data of one of the 0.14 NA images. Figure 26 shows the projection of a deconvolved volume that is 3mm deep. The deconvolution is not able to remove light along the  $z$ -dimension or optical axis effectively enough to limit the reconstruction to the defined volume. This cloud did not have the wire imaged onto it and was close to spherical in shape and easily fit well inside the nearly  $2\text{mm} \times 2\text{mm} \times 3\text{mm}$  volume of the reconstruction. Figure 27 shows that if the  $z$ -axis depth of the deconvolved volume is long enough, the deconvolution does reach a point at which it can effectively determine that no light is coming from those planes, but the result indicates a long cigar-shaped MOT according to the deconvolution when it is much closer to a sphere in reality. The standard image gives a diameter measurement of about  $0.73 \pm 0.03\text{mm}$ , for  $NA = 0.14$  the resulting back projection lengthening factor,  $\tan(\pi/2 - \alpha_0) = 7.1$ , giving a predicted axial length of  $5.2 \pm 0.2\text{mm}$ . The extent of the spreading measured from the projection of the reconstruction was  $5.8 \pm 0.5\text{mm}$ .

To double check the back projection calculation on a more controllable case, a modeled volume (**g**) was made. The volume had voxel values of all zeros except in one plane along the optical axis. This plane was at  $z = -250\mu\text{m}$  and a value of one was given to voxels in the shape of an ellipse. The volume containing this thin ellipse was then forward projected to create an image. The resulting image was deconvolved the same way as the cold atom pictures. The reconstructed volume shows the peak at the appropriate location and the shape stretched along the optical axis as expected.



**Figure 27.** Here as apposed to Figure 26 the deconvolved volume does limit the light in the  $z$ -direction but it is far too extended, reaching a projected FWHM of about  $5.8 \pm 0.5\text{mm}$  when the atoms only extend about  $0.7\text{mm}$  in the  $x$  and  $y$  directions.

An ellipse with a semi-major axis of  $304\mu\text{m}$  and a semi-minor axis of  $192\mu\text{m}$  gets spread along the optical axis  $1450\mu\text{m}$  using the FWHM of the reconstruction data down the center of the volume. The predicted spreading is  $2l = 1460\mu\text{m}$ . Figure 28 shows the ellipse, the resulting plenoptic image and the reconstruction projected along the  $x$ -axis.

#### 4.4 Error

The error in the peak locations of the projection images is estimated from the resolution of the reconstruction and the angle chosen for the projection. The resolution, in the case of the plenoptic projection, was determined by the magnification of the optical system and the diameter of the micro lenses, giving an  $(x, y)$  resolution of  $16\mu\text{m}$ , along with the  $z$ -axis resolution of the voxels,  $50\mu\text{m}$ . In the case of the reference image, the resolution is purely the magnification of the objective and the size of the pixels. This estimation of the error is based on the discrete nature of the data and pixel noise. This contribution to error was estimated straightforwardly as half the pixel size in a given direction. This pixel error is the only error in the reference image measurements. In the case of MOT One, a different objective was used for the reference image than for MOT Two and MOT Three; the magnification was lower,

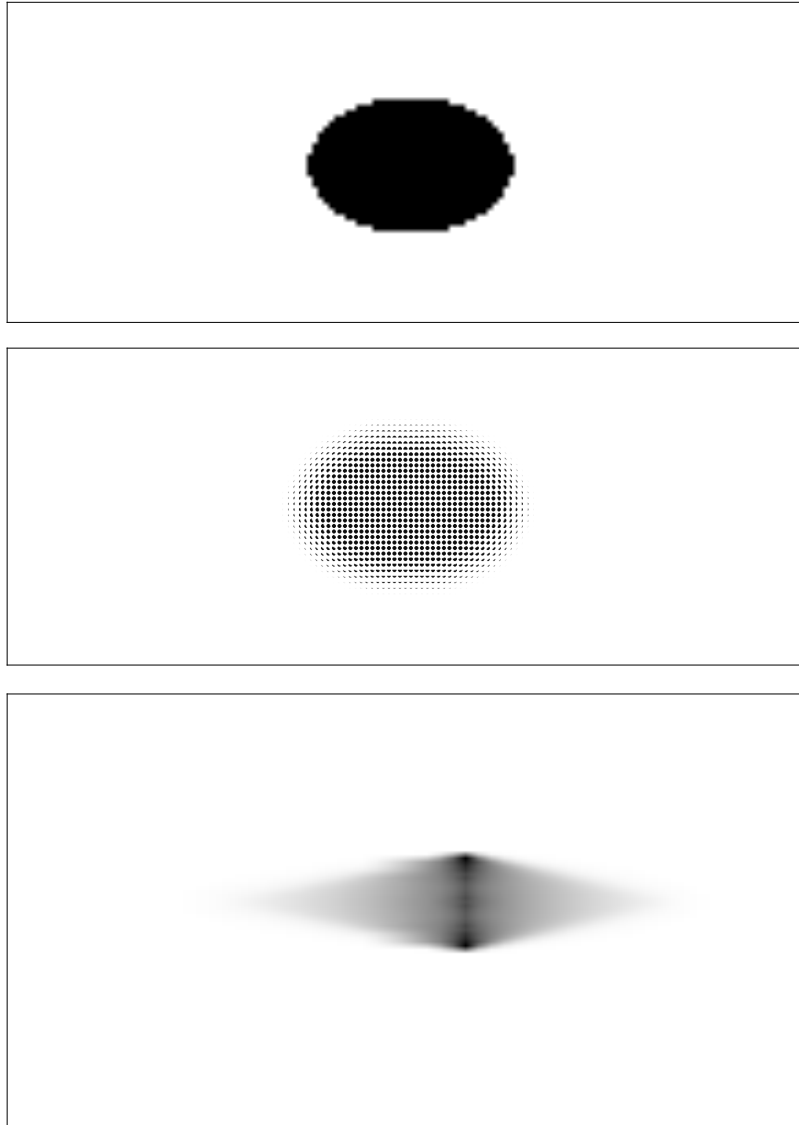


Figure 28. The top image is the ellipse placed in the reconstruction volume and then projected on to the sensor. The resulting image is shown in the center. The reconstruction is projected along the major axis of the ellipse in the bottom image, showing the optical axis spreading. The ellipse has a minor axis of  $384\mu\text{m}$ , giving an expected axial spreading of  $1460\mu\text{m}$ , the measured spreading was  $1450\mu\text{m}$ .

hence there is a larger error in the reference image locations (see Table 2).

The second source of position error is from the angle of the reference camera with respect to the reconstructed volume created from the plenoptic image. The projection was created assuming that the reconstructed volume was level with the optical table and that the  $x$ -axis of the reference image was in line with the  $z$ -axis of the plenoptic volume (also level with the table); that is, the image was taken at  $90^\circ$  degrees to the  $z$ -axis and rotated up to be looking down on the reconstructed volume from the side. That meant that the Radon transform could be performed on individual slices along the  $z$ -axis. However, there are variations to how level the reconstructed volume was, how well-aligned the camera was to the  $z$ -axis and even how far up it was rotated. This error can be approximated by looking at the effects of rotations on a vector in the plenoptic volume.

The plenoptic volume has coordinates  $(x, y, z)$  as shown in Figure 19. Using the  $x$ -,  $y$ -, and  $z$ -axes as fixed pitch, yaw, and roll rotation axes, the view of the reference camera can be rotated to the view of the plenoptic camera by three rotations. First a rotation around the  $x$ -axis of  $\theta_{x1}$  if the volume is not level. Second, a rotation around the  $y$ -axis of  $\theta_y$ , which will be approximately  $90^\circ$  to get the side view. Lastly a second rotation around the  $x$ -axis of  $\theta_{x2}$ , which will be approximately  $50^\circ$  to raise the view to looking down on the original volume. This set of rotations will transform a vector in the original plenoptic volume  $(x_1, y_1, z_1)^T$  to a vector  $(x_2, y_2, z_2)^T$  seen by the reference camera. The rotation matrix  $R$  is

$$R = \begin{pmatrix} \cos(\theta_y) & \sin(\theta_{x1}) \sin(\theta_y) & \cos(\theta_{x1}) \sin(\theta_y) \\ \sin(\theta_{x2}) \sin(\theta_y) & \cos(\theta_{x1}) \cos(\theta_{x2}) - \cos(\theta_y) \sin(\theta_{x1}) \sin(\theta_{x2}) & -\cos(\theta_{x2}) \sin(\theta_{x1}) - \cos(\theta_{x1}) \cos(\theta_y) \sin(\theta_{x2}) \\ -\cos(\theta_{x2}) \sin(\theta_y) & \cos(\theta_{x2}) \cos(\theta_y) \sin(\theta_{x1}) + \cos(\theta_{x1}) \sin(\theta_{x2}) & \cos(\theta_{x1}) \cos(\theta_{x2}) \cos(\theta_y) - \sin(\theta_{x1}) \sin(\theta_{x2}) \end{pmatrix}. \quad (48)$$

Then  $(x_2, y_2, z_2)^T$  is given by

$$\begin{pmatrix} x_2 \\ y_2 \\ z_2 \end{pmatrix} = R \begin{pmatrix} x_1 \\ y_1 \\ z_1 \end{pmatrix}. \quad (49)$$

The values  $x_2$  and  $y_2$  are the 2D projected coordinates of the original vector in the new reference frame. Taking the total differential of  $x_2$  and  $y_2$  gives their respective errors given  $(x_1, y_1, z_1)$ ,  $(\delta x_1, \delta y_1, \delta z_1)$ ,  $(\theta_{x1}, \theta_y, \theta_{x2})$ , and  $(\delta\theta_{x1}, \delta\theta_y, \delta\theta_{x2})$ .  $(x_1, y_1, z_1)$  is estimated using the calculated  $z$  location from the projection and the standard image  $x$  and  $y$  locations, and  $(\delta x_1, \delta y_1, \delta z_1)$  are simply the resolution errors.  $(\theta_{x1}, \theta_y, \theta_{x2})$  is assumed to be simply the rotation used for the projections,  $(\theta_{x1}, \theta_y, \theta_{x2}) = (0, 90^\circ, 53^\circ)$  for MOT One, and  $(\theta_{x1}, \theta_y, \theta_{x2}) = (0, 90^\circ, 51^\circ)$  for MOT Two and MOT Three. The errors in the angles were estimated based on the camera locations and the measurement of the  $\theta_{x2}$  rotation,  $(\delta\theta_{x1}, \delta\theta_y, \delta\theta_{x2}) = (1^\circ, 3^\circ, 9^\circ)$  for MOT One, and  $(\delta\theta_{x1}, \delta\theta_y, \delta\theta_{x2}) = (1^\circ, 3^\circ, 5^\circ)$  for MOT Two and MOT Three. The error for MOT One tends to be higher than for MOT Two and MOT Three because of the greater uncertainty in the determination of the reference camera angle  $\delta\theta_{x2}$  (see Table 2).

The location error based on the pixel's resolution and the location error based on the rotation error were added in quadrature to determine the error of the locations in Table 2. For the error in the back projection lengths in Table 3, the location errors were simply propagated through the calculation.

There is a systematic error evident in the projected reconstruction axial separation. In the case of MOT Two and MOT Three, the  $z$ -axis splitting measurement in Table 2 is smaller than the reference in both cases. This is because the clouds were closer together in the first place, and due to the reconstruction noise near the center planes of the reconstruction, the Gaussian fits get pulled toward the center.

#### 4.4.1 Impact of Using the Lytro Development Kit Sensor.

The LDK micro lens array and sensor provided a simple and cost-effective basis for the LFM where custom systems were more than twice the cost. The sensor also provided an excellent  $(x, y)$ -plane resolution while still providing depth information. However this did fix the micro lens properties so the rest of the LFM had to be built around this. The micro lenses were not designed for large magnifications and the optics of the objective and tube lens had to be restricted to matching the  $f/\#$  of the MLA. This was not a major problem for this system because increasing the magnification made the atom cloud larger than the field of view. But with further objective design, this could be expanded and greater magnification could be applied, which can improve the  $(x, y)$  resolution further, if the loss in angular resolution can be accepted along with a reduction in the volume that can be reconstructed.

The larger impact on performance came from the color sensor. The Lytro® sensor was designed for visible wavelength color images with well lit scenes. The pixels were very small,  $\approx 1.4\mu\text{m}$  and color filtered with a Bayer pattern, resulting in primarily red pixels responding to the 780nm wavelength fluorescence of the atoms, and very little light reaching a given pixel. Only one in four pixels are red in the Bayer pattern resulting in a greatly reduced signal detected by the sensor. The exposures had to be several seconds to get a good signal and small signals got washed out by the noise. This contributed to the estimated location error resulting from pixel noise. Additionally, it made determining the correct intensity signal at the sensor difficult to determine from the measured pixel values, and as discussed in Chapter V, made detecting the low levels of light needed for absorption imaging impractical. The pixel intensity is ultimately used to determine the number of atoms seen in the image (see Section 4.8). For this first application of a LFM to cold atom imaging, this was not

a limiting factor but future application to atom interferometry will require accurate measurements of the atom number and distribution.

#### 4.5 Phase Term Effects on the 3D Volume

As discussed in Section 4.1, the phase term,

$$\exp\left(-\frac{iv^2}{4N}(1+M)\right), \quad (50)$$

is typically dropped from  $U_i$ , the PSF equation, assuming  $N \gg v^2/4$ , but is not for this LFM. This means there is a fairly rapidly changing phase term that needs to be added to the calculation of the PSF. The question then is, what is the impact of including this phase?

For  $U_i$ , the difference between the wave with the additional term dropped and that with it added is a change in overall phase. The added term is a quadratic phase with respect to the radius  $v$  which will come out as a shift in the focal point of the point source. This can be seen in the intensity difference on the sensor between PSFs created with and without the additional term as shown in Figure 29. The intensity behind each micro lens is shifted toward the center. If a point is being focused past the MLA, then the rays will tend toward the center of the cone focusing down to the actual image point, while if the point is being focused before the MLA, the rays tend to be focused away from the center behind the MLs. So a shift of rays towards the center shifts the light field up in object space.

This shift in the light behind the ML impacts the deconvolution. The difference between two deconvolutions, which were the same except for the phase term in the creation of the PSFs, is shown in Figure 30. The primary effect is a shifting of the light in the positive  $z$ -direction.

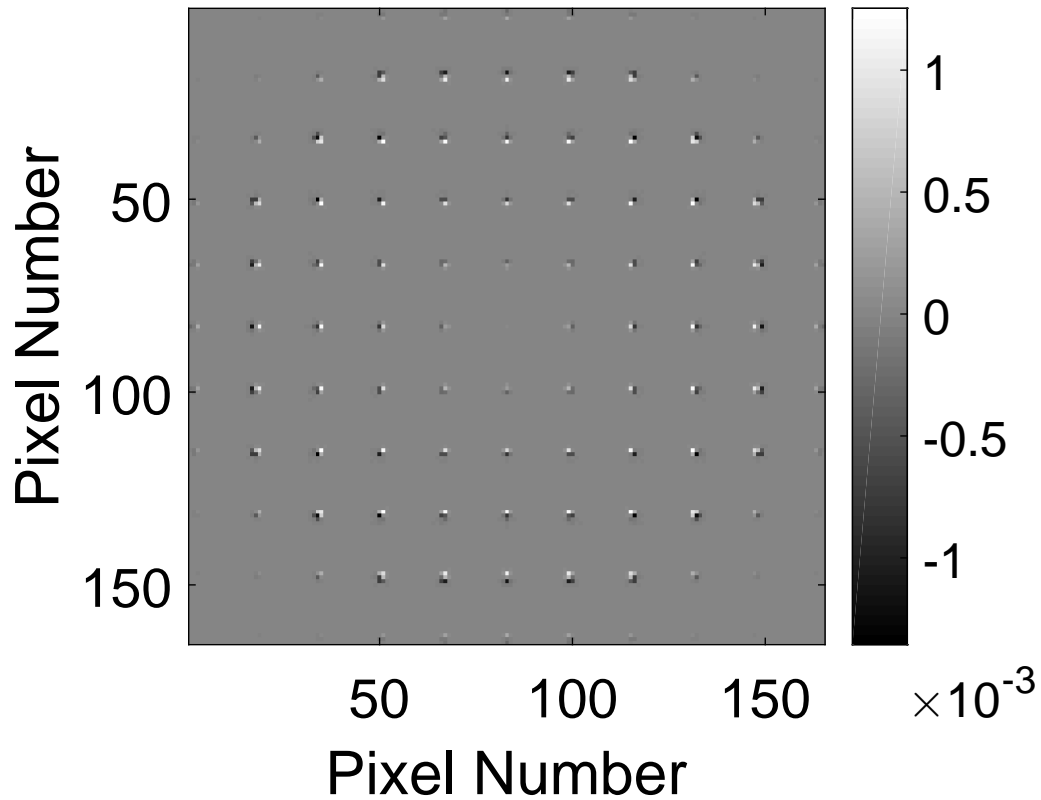


Figure 29. A plot of the difference between the PSF intensity at the sensor calculated with and without the typically dropped phase term (Equation (50)) used in calculating  $U_i$ . It is clear that near the origin the effect is small but has increasing importance as the distance from the center increases. The intensity behind each ML is shifted preferentially toward the center as those value are more positive. The difference scale is on the order of  $10^{-3}$  which is also the scale of the intensity images from which it is derived.

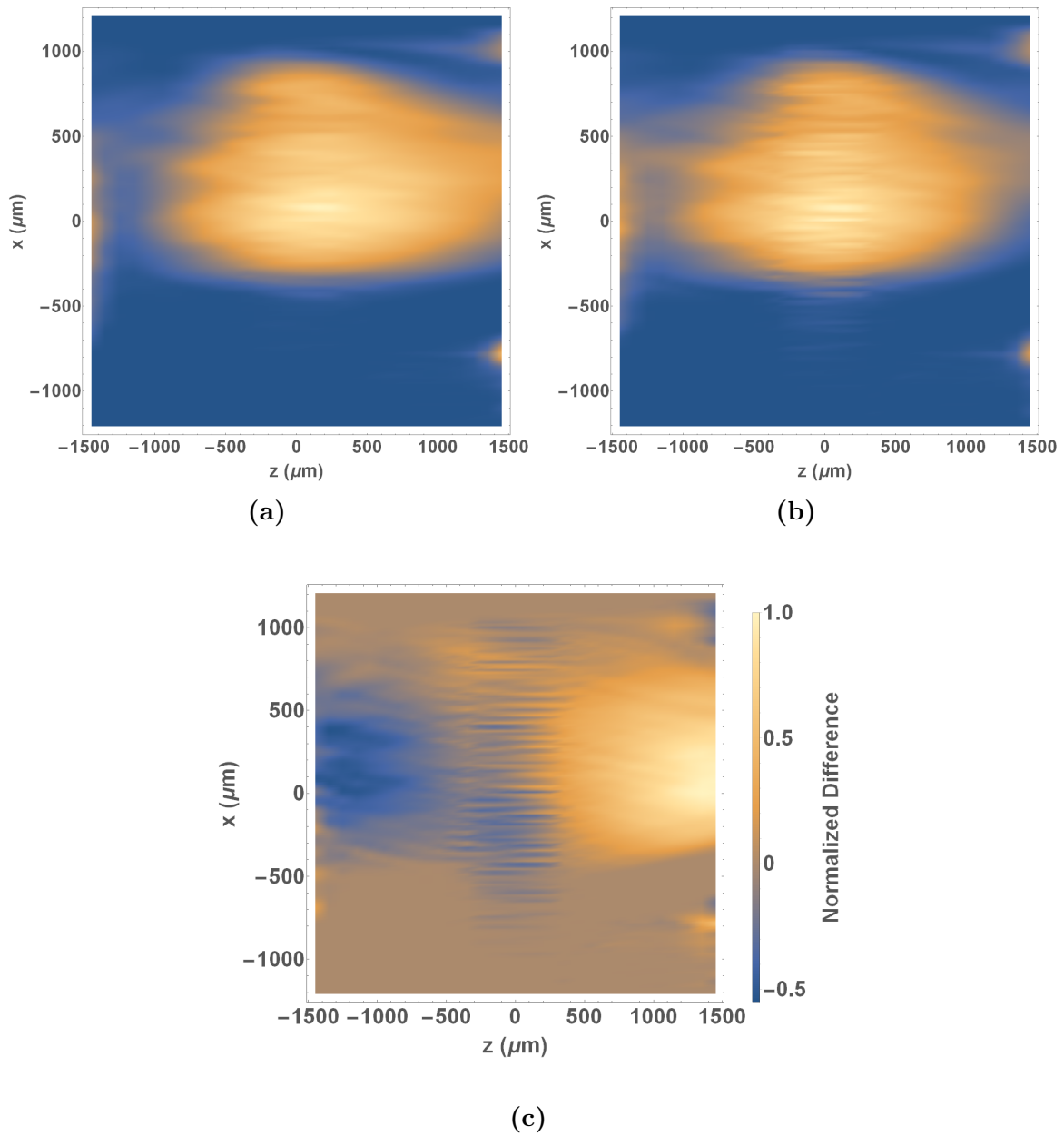


Figure 30. The deconvolution produced using PSFs modeled with the added phase term is in (a), and the one without it in (b). (c) shows a projection of the difference of the two deconvolved volumes, emphasizing the shift in light from the back to the front.

## 4.6 Shifting the Focal Plane of the LFM

Another simple measure of the accuracies of the LFM 3D reconstructions was performed, in some ways by accident, on MOT Two and MOT Three. When imaging the atoms it was difficult to tell exactly when the cloud of atoms was in focus. The focal distance was directly measured as accurately as possible from outside the vacuum chamber but the error was on the order of a millimeter which was the scale of the cloud. To get at least one image with the entire cloud in focus, seven pictures were taken shifting the position of the camera between each. The first image was the central point, assuming it was near the optimal focus. Three images were taken moving the camera closer at each step. The camera was returned to the center position and three more images were taken moving back at each step. Each step was a shift of  $230\mu\text{m}$  along the optical axis using a translation stage and micrometer. From this series of images, one that was in focus on one atom cloud or the other was used. It also provided data on the accuracy of the measured axial locations made from the reconstructions. Figure 31 shows a fixed projection of the reconstructed volume with the full series of images taken in micrometer position order.

Figure 32 shows the  $z$ -axis locations of the two peaks in the clouds as determined by the reconstruction plotted versus the relative camera position. The offset of the peaks shows that neither was quite in focus for the central image but it was actually centered between the two peaks and shows their axial separation from each other. The straight center line in the figure is a plot of the camera position plotted against its self. The slope of the peak lines should match that of the center line if the reconstruction always accurately determined the locations of the cloud as the cloud would shift the same amount as the camera. Instead the slopes change. As the peaks start to get close to the edge of the reconstruction volume ( $z = 1500\mu\text{m}$ ), the slope starts to increase, and when it is near the center of the volume ( $z = 0\mu\text{m}$ ), the slope decreases.

It is most notable in the Peak 1 data which was the brighter of the two clouds. This is a result of the pull on the Gaussian fits toward the edges of the volume when the cloud is close to the edge and towards the noise in the center when the cloud is near  $z = 0\mu\text{m}$ .

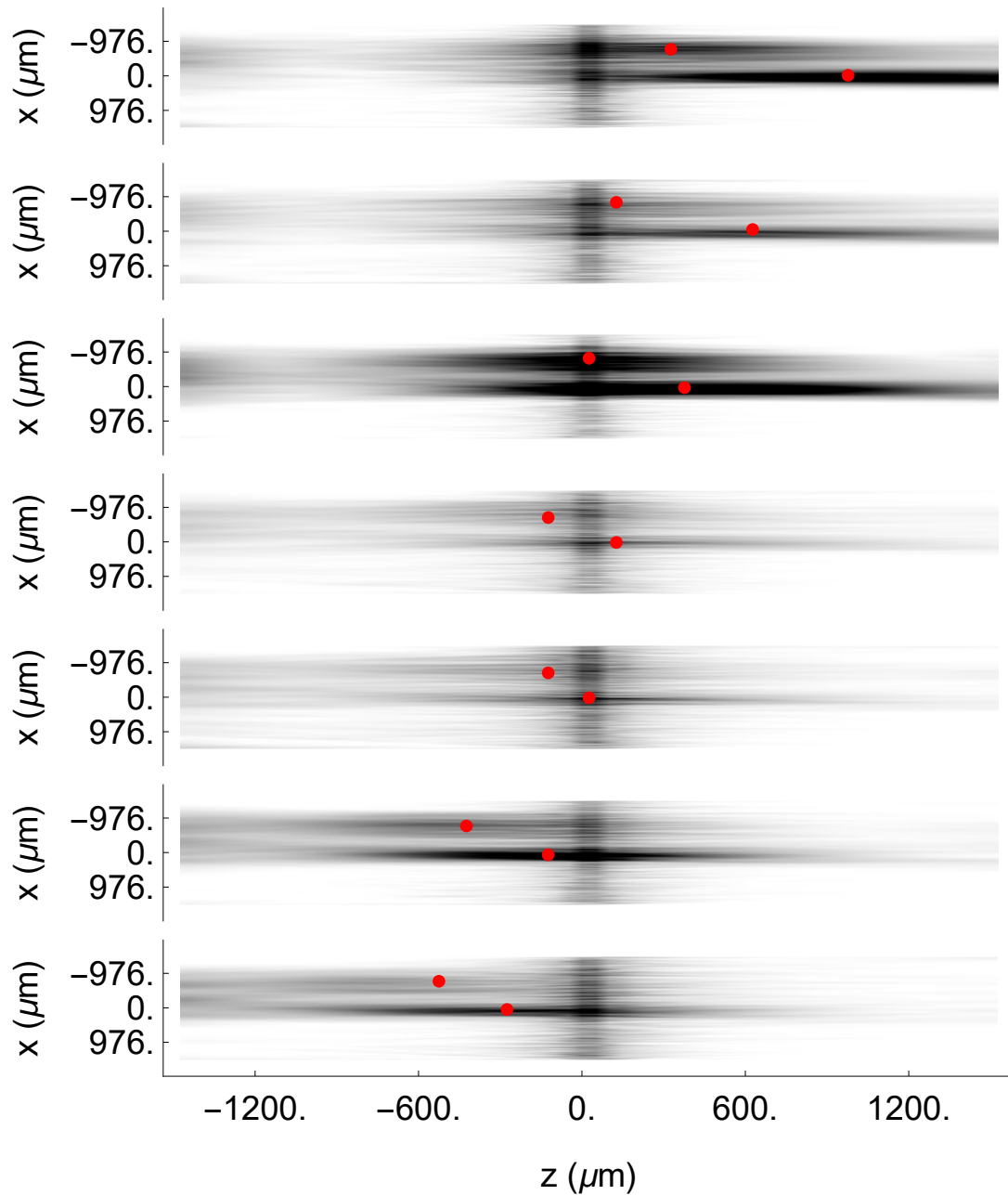


Figure 31. A series of projected reconstructions of MOT Two from images taken while adjusting the position of the LFM, effectively changing the focal plane to different planes in the MOT. The red points show the calculated centers of the cloud. The reconstruction can effectively determine if the cloud is shifting closer or further away. The spacing on the shifting locations is compared to the actual shift of the MLA in Figure 32. Note: The aspect ratio has been stretched to show the changing locations along the  $z$ -axis all together.

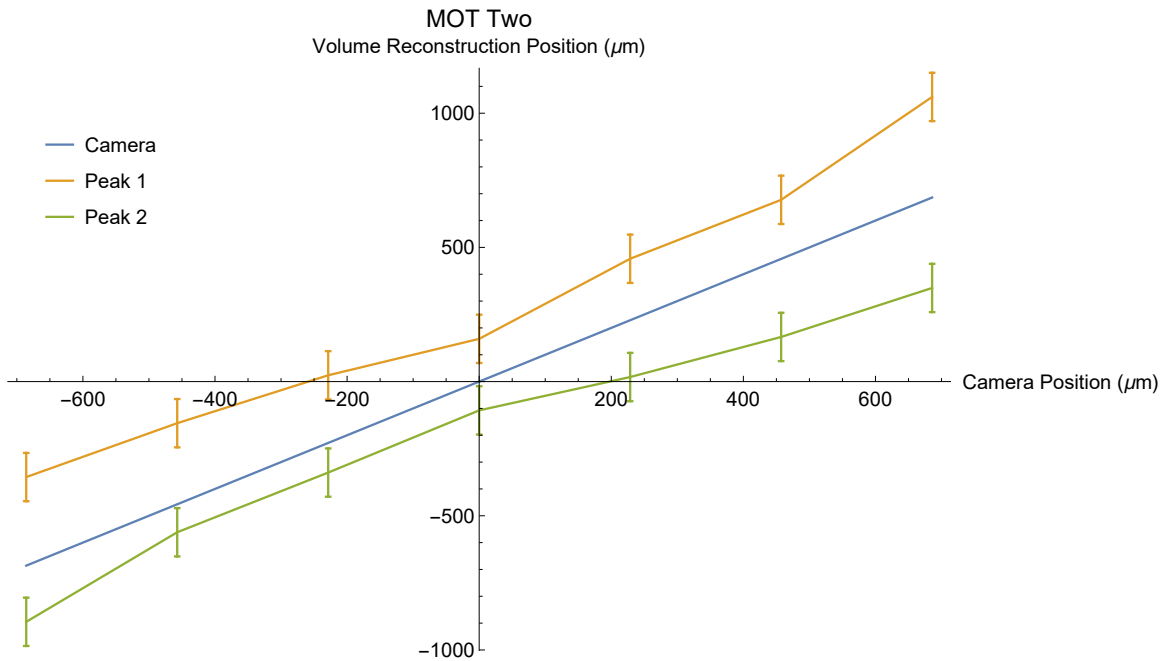
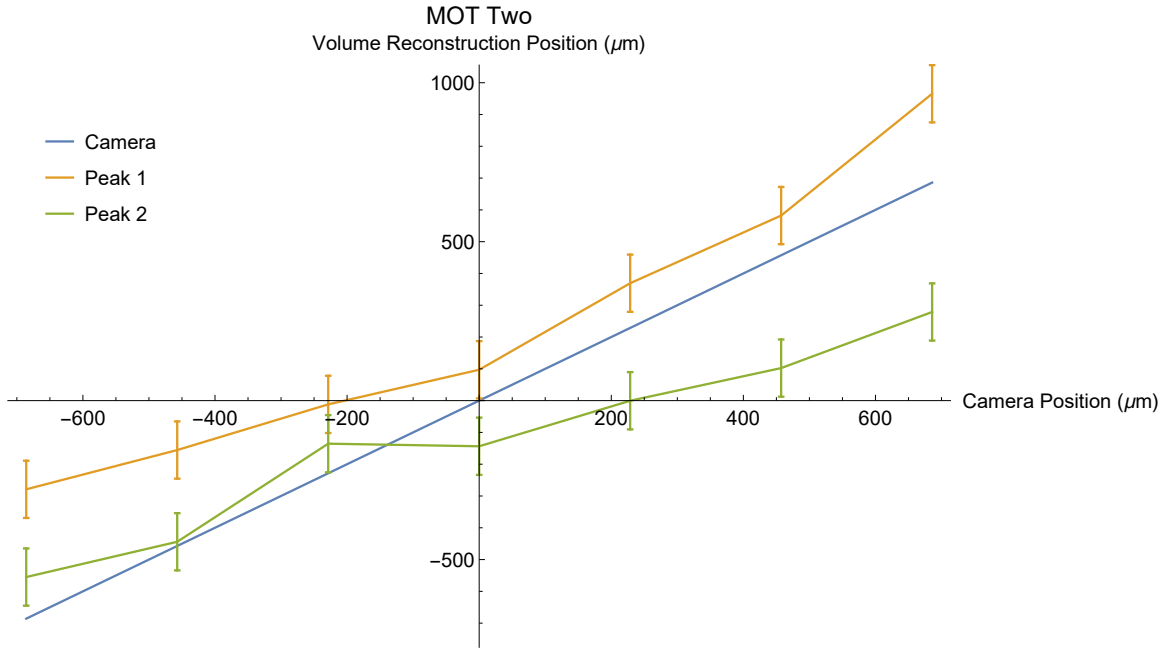


Figure 32. The measured location along the  $z$ -axis of the two peaks in the MOT atom cloud reconstructions after projection, as a function of shifts in the focal plane position made by moving the camera forward and back with micrometer stage. The Camera line is a plot of its position against itself. Moving the camera “forward” is a negative translation along the  $z$ -axis so the Camera position sign was flipped, to give a better comparison of how the MOT positions would ideally be shifting.

## 4.7 Optical System Trade Offs

There are many factors to consider when designing a LFM; on the optical side, there is NA, magnification, and micro-lens size. There are also practical factors such as working distance, and physical pixel size. The working distance tends to decrease with increasing NA but with good objective designs such as the long working distance Mitutoyo objectives, this can be adjusted to some degree independently of the NA. The pixel size is closely tied to the diffraction-limited spot size of the imaging system including magnification.

If a large reconstruction volume with the best possible resolution is desired, the pixel size is the primary physical limitation to consider because of its direct relation to the NA and magnification  $\mathcal{M}$  via the spot size given by the Sparrow limit in Equation (18). Considering the pixel as the limit on spot size, it can be used to determine the highest NA and magnification combination possible. Figure 33 shows how the spot size changes with respect to magnification and NA. Obviously a bigger NA gives a smaller spot size, and this allows for more total spots in the trade-off between angular and spatial resolution. Determining the desired spot size fixes the  $\mathcal{M}/\text{NA}$  ratio, but in general, a larger NA is desired as it also reduces the optical axis spreading as discussed in Section 4.3.2. With the desire for a high number of spots/pixels but with the limit of a  $1\mu\text{m}$  pixel, the NA and magnification pairs that

**Table 4. Numerical Aperture Optical Stretching Factor and Magnification Resulting in  $\approx 1\mu\text{m}$  Spot Sizes**

NA	$\tan(\pi/2 - \alpha_0)$	Magnification
0.14	7.1	0.38
0.26	3.7	0.71
0.4	2.3	1.10
0.7	1.0	1.91
0.9	0.5	2.45

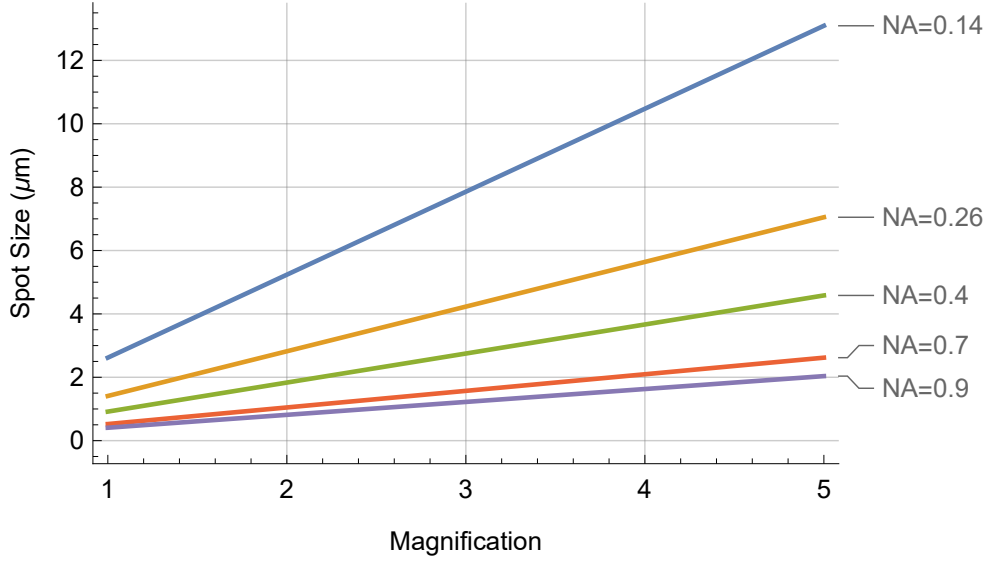


**Figure 33.** The spot size of the LFM increases linearly with Magnification with a slope dependent on the NA. The higher NA the better the spot size and the smaller the optical axis spreading from back projection.

result in  $\approx 1\mu\text{m}$  spot sizes can be calculated and are shown in Table 4 along with the axial spreading factor. This fixes the NA and magnification variables in looking at the other properties of the LFM.

The next consideration is the axial resolution in the depth of field  $D_{\text{tot}2}$ , the full depth of field  $D_{\text{tot}3}$ , and the spatial resolution  $R_{\text{res}}$ . Using Equations (18) and (19),  $D_{\text{tot}2}$  and  $D_{\text{tot}3}$  can be written in terms of NA,  $D_{\text{ml}}$ , and  $\mathcal{M}$ ,

$$D_{\text{tot}3} \approx \frac{\lambda n}{NA^2} + \frac{D_{\text{ml}}^2 n}{2(0.47)^2 \lambda \mathcal{M}^2}. \quad (51)$$

Similarly a single slice is

$$D_{\text{tot}2} \approx \frac{\lambda n}{NA^2} + \frac{D_{\text{ml}} n}{2(0.47) NA \mathcal{M}}. \quad (52)$$

The spatial resolution is simply  $R_{\text{res}} = D_{\text{ml}}/\mathcal{M}$ . All depend on the chosen diameter of the micro lens. Figure 34 shows the resolution, depth of field, and full depth of

field as a function of micro lens diameter.

Basing the design off of the minimum spot size optimizes the system in terms of depth of field. It will allow the most resolvable points behind a micro lens of a given diameter which gives the largest full depth of field. Given a minimal acceptable resolution, the result will be the best axial resolution over the largest volume. For instance with a  $NA=0.7$ , a magnification of 2 and  $D_{ml} = 40\mu\text{m}$ , the resulting system would have a spatial resolution of about  $20\mu\text{m}$ , a depth resolution of about  $30\mu\text{m}$ , and a full depth of field of about 1mm, which could work well for a small MOT atom cloud. In the  $NA=0.26$  system used in this work, the working distance was a higher priority and the full implications of the limits imposed by the NA were not yet known.

The system can be optimized for axial resolution as well by increasing the magnification. For instance a 3D lattice of atoms could be imaged such as the lattice described by Nelson in [52], where imaging multiple layers of the lattice all at once is desired. In Nelson's paper, the spacing between atoms is approximately  $5\mu\text{m}$ . Using a LFM with a  $NA=0.7$  objective, a magnification of 80, and  $D_{ml} = 175\mu\text{m}$ , the slice depth of field is  $4.92\mu\text{m}$  with a full depth of field of  $15.5\mu\text{m}$  potentially allowing about three different layers of the lattice to be distinguished.

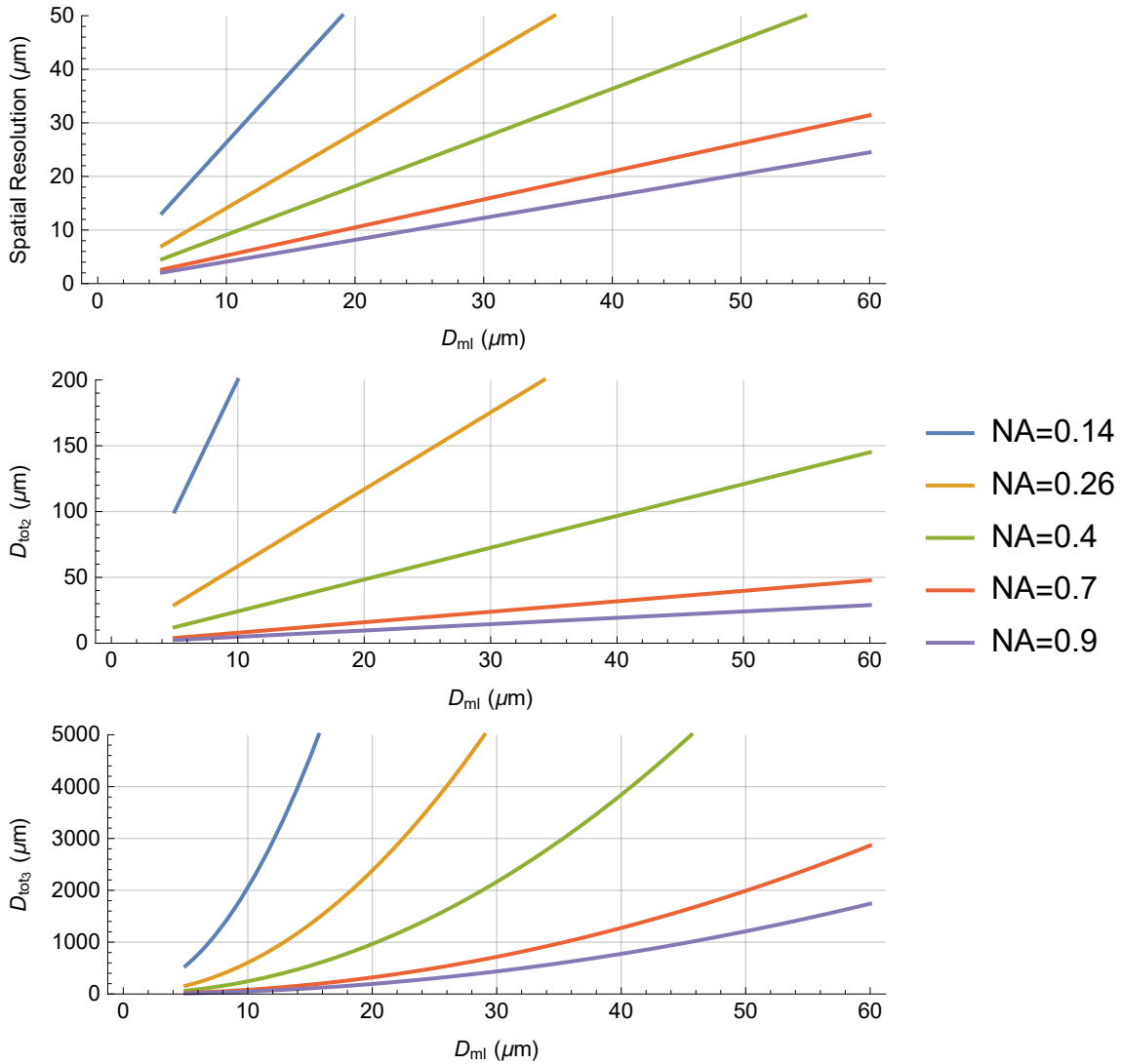


Figure 34. The top plot is the spatial resolution of the LFM as a function of the diameter of a micro lens  $D_{ml}$ , for different numerical apertures. The middle and bottom plots are the slice depth of field and the full depth of field along the optical axis also as a function of  $D_{ml}$  for the same set of numerical apertures. The magnification is chosen to give a  $1\mu\text{m}$  spot size.

## 4.8 Atom Number Measurements

All of the MOT cloud images were taken using fluorescence from the atoms. While in the MOT, the atoms are absorbing light from the trapping lasers and then re-radiating. This fluorescence depends on the number of atoms in the cloud and can be used to measure the 2D density distribution from an image. In order to get the density distribution, the rate that light is emitted per atom is related to the intensity of light measured by an image or photo-diode. The fluorescence for an atom is given by the scattering rate of the atom

$$R_s = \frac{\Gamma}{2} \left( \frac{I/I_{sat}}{1 + I/I_{sat} + 4\Delta^2/\Gamma^2} \right), \quad (53)$$

where  $I$  is the incident intensity,  $\Delta$  is the detuning of the laser from resonance,  $\Gamma$  is the natural line width, and  $I_{sat}$  is the saturation intensity. The number of atoms seen by a given pixel is given by

$$N = \frac{4\pi(\text{photon detection rate})}{(\text{solid angle})R_s}. \quad (54)$$

The solid angle is determined by the radius of the objective  $a$  and the distance from the atoms  $d$  and is equal to  $\pi \frac{a^2}{d^2}$ . The photon detection rate is determined by the camera sensor's quantum efficiency and the exposure time.

This calculation is prone to errors. These include not getting the solid angle correct due to errors in distance to the atoms, to scattering rate changes due to line broadening, power broadening and the optical thickness of the atoms in front of the radiating atoms [61]. But fluorescence imaging is easy, can be done continuously while the atoms are in the MOT, and is easily applied to a LFM.

The number of atoms in the atom clouds imaged here was calculated using an objective lens with an aperture of one inch, focusing on a Thor Labs PDA100A

photodiode to count photons. Unfortunately, the objective got misaligned from the atoms but the change was not caught until after the data had been collected. The directly calculated atom numbers are about a factor of 100 lower than expected.

If this had not been the case, the total number of atoms in the cloud calculated using the photodiode could be used to calibrate the LFM volume reconstruction. By sectioning off each cloud with an intensity threshold and then totaling the intensity associated with each cloud, the overall intensity of the cloud in the image could be determined. The total number of atoms related to the overall intensity of the cloud would give the intensity per atom as measured by the LFM in the reconstructed volume. Then the cloud number distribution could be determined. However, it would not have been very accurate because of the axial spreading in the reconstruction. But this application would be needed for determining atom number in two atom clouds resulting from an interferometric measurement as mentioned in the introduction.

Future work can be done to utilize the intensity images taken by the LFM for atom number calculations. A calibration step would be essential as the reconstruction places light in the volume iteratively and not completely accurately. Knowing the value of a voxel cannot be directly tied to the intensity of that voxel in object space. The calibration would simply be a measurement of the total number of atoms in the cloud as described above. Once this is done, the number of atoms imaged can be calculated directly from the images and reconstructions.

## V. Absorption and Off-Resonance Imaging

The previous chapter dealt entirely with atoms in a MOT being imaged by measuring their fluorescence. In this chapter, imaging atoms by absorption imaging or their dispersive properties will be explored in relation to the plenoptic camera's capabilities.

### 5.1 Absorption and Off-Resonance Imaging Theory

Absorption and off-resonance imaging can be more accurate than fluorescence imaging because it avoids unknowns in scattering rate changes from line broadening and power broadening, and the optical thickness of the atoms in front of radiating atoms does not come into play. It is a bit more difficult to do because a probe laser is needed to image the atoms. The principle is to shine a laser through the atoms, which will interact with the light casting a “shadow” on a sensor array. The recorded image can be used to determine the 2D column distribution of the atoms.

The light interacts with the atoms via their complex index of refraction which depends on the density distribution of the atoms. For a two-level atomic system using the rotating wave approximation, the index of refraction is

$$n_{refr} = 1 + \frac{\sigma_0 n(x, y, z) \lambda}{4\pi} \left[ \frac{i}{1 + \delta^2} - \frac{\delta}{1 + \delta^2} \right], \quad (55)$$

where  $n(x, y, z)$  is the number density of the atoms,  $\sigma_0 = \frac{\hbar\omega_0\Gamma}{2I_{sat}}$  is the resonant cross section, and  $\delta \equiv \frac{\omega - \omega_0}{\Gamma/2} = \frac{\Delta}{\Gamma/2}$  is the detuning of the probe light frequency  $\omega$  from the atomic resonance frequency  $\omega_0$ , normalized by the natural half line width of the atomic transition  $\Gamma$  [43]. This imaginary index gives both the absorption (from the imaginary part) and the phase shift (from the real part) imparted to a wave propagating through the atoms. Assuming the probe beam is simply a collimated plane wave propagating

along the  $z$ -axis, the scalar wave just after the atoms can be given by

$$E(x, y) = E_0 \exp \left\{ ik_0 \int [n_{refr}(x, y, z) - 1] dz \right\} = E_0 t(x, y) \exp(i\phi(x, y)), \quad (56)$$

where, given  $\tilde{n} = \int n(x, y, z) dz$ ,

$$t(x, y) = \exp\left(-\frac{\tilde{n}\sigma_0}{2} \frac{1}{1 + \delta^2}\right) \quad (57)$$

and

$$\phi(x, y) = -\frac{\tilde{n}\sigma_0}{2} \frac{\delta}{1 + \delta^2}. \quad (58)$$

Pure absorption imaging is the case where  $\delta = 0$  and there is no phase shift in the wave, only attenuation. In this case, the imaged intensity is

$$I = \frac{1}{2} |E|^2 = \frac{1}{2} |E_0|^2 \exp(-\tilde{n}\sigma_0) = I_0 \exp(-\tilde{n}\sigma_0). \quad (59)$$

In practice,  $\tilde{n}$  can be extracted by taking an intensity image with no atoms present,  $I_0$ , and dividing by an atom image with the atoms in the path of the probe beam,  $I$ . An image of background light is subtracted from each to remove the added noise,  $I_{bg}$ ,

$$\frac{I - I_{bg}}{I_0 - I_{bg}} = \exp(-\tilde{n}\sigma_0). \quad (60)$$

The resulting image can then be used to calculate  $\tilde{n}$ .

### 5.1.1 Absorption Imaging with the Light Field Microscope.

Using the LFM discussed in the last chapter and NA=0.26 objective, some absorption images were attempted. But it was determined that with the LDK MLA and sensor, it was impractical to do.

The three images just described are typically taken in rapid succession because the probe beam is coherent and there are always some interference effects from optics and surfaces in the path of the beam. Taking the atom and intensity images as close together as possible in time reduces any changes between images that might take place in the interference pattern over time. The images are also taken in sync with the control system of the MOT in order to precisely time exposures of the camera and probe beam to when the atoms are present and when they are not. Typically the timing system is set up as desired to control the atoms, then the probe beam and camera are triggered at the appropriate times.

Timing the system was a problem as the LDK sensor was not designed for an external trigger or to be read quickly. Successive images had to be taken about 500ms apart. Without an external trigger, the control of the MOT and the probe beam had to be based around when the camera took the picture. A triggering signal was used which came from the camera when it would fire its physical shutter, but the timing on the actual exposure would change shot to shot by as much as 4ms. This made synchronizing the probe beam with the exposure of the sensor difficult. Additionally, the camera used a rolling electronic shutter along with the physical shutter and they could not be controlled independently. The lack of control, along with the fact that a probe pulse for good absorption imaging is typically about  $10\mu\text{m}$  long meant that, even when the timing did work, only part of the sensor would be exposed. The end result was, after many attempts at taking a picture, only one or two sets of intensity, atom and background images would be correctly timed, greatly increasing the time needed to make adjustments.

Additionally, the quantum efficiency of the sensor at the 780nm wavelength was low. High probe beam intensities on the order of a  $100\mu\text{W}$  along with long exposure times on the order of 0.5ms were needed just to consistently see a signal from the

beam. Exposure to the probe beam cycles the atoms out of the absorbing transition into a dark state in about  $170\mu s$ , so most of the light observed by the camera was not absorbed by the atoms. The combination of poor timing control and very low absorption signal made standard imaging of absorption impractical with the LDK sensor.

With some custom design, most of these problems could be avoided. Then the properties of a plenoptic system should provide angular as well as spatial information about the light imaged. With absorption imaging, the light is primarily a plane wave coming straight at the camera with no angular component; in general there is little angular information to be measured. But in the case of pure absorption, the atoms do cause some diffraction and an estimate of the amount of diffraction can be made by assuming the atom cloud is a fully absorbing disk of some radius  $r$ . The normalized Fraunhofer diffraction of a circular aperture can be written in terms of the angle of the ray from the center of the disk as

$$I(\theta) = \left( 2 \frac{J_1(kr \sin(\theta))}{kr \sin(\theta)} \right)^2,$$

where  $\theta$  is the angle of the ray,  $k$  is the wave number, and  $J_1$  is the first order Bessel function.  $I(\theta)$  is the Airy disc. Using Babinet's principle, the image of a blocking disk will simply be the shadow  $1 - I(\theta)$  [12].

Most of the diffracted light (or diffracted shadow in this case) is contained in the center peak of the Bessel function. Using the first zero of the Bessel function, the angles containing most of the diffracted light can be calculated and compared to the angles measurable by the LFM system. The first zero is at  $3.83 = kr \sin(\theta)$ . Given a LFM with a resolvable angle  $\theta$ , the necessary size of the cloud can be determined. The resolution in angle of the LFM sensor is simply twice the acceptance angle of the objective  $\alpha_0$  divided by the number of resolvable spots behind a micro lens  $N_u$ ,

$R_{\text{angle}} = 2\alpha_0/N_u$ . For the NA= 0.26 LFM from Chapter IV,  $R_{\text{angle}} = 0.046$  rad. For a wavelength of  $\lambda = 780\text{nm}$  and  $\theta = 0.046$  rad, the radius of the disk would need to be  $r = 10.3\mu\text{m}$ . This is already smaller than the spatial resolution of  $16\mu\text{m}$  and increasing the angular resolution will only decrease the spatial resolution, and vice versa. Increasing the size of the cloud only reduces the angle of diffracted light, and in the end, the cloud is not strictly a disk so the diffraction would be reduced even more. This means that for standard absorption imaging, the plenoptic camera cannot collect any angular information without reducing the spatial resolution too far. So no angular information could be extracted.

## 5.2 Off-Resonance Imaging

Off-resonance imaging takes advantage of the dispersion of the light in the atoms and occurs when  $\delta \neq 0$  in Equation (56). The phase shift  $\phi(x, y)$  is non-zero and the absorption  $t(x, y)$  is reduced by  $1/(1 + \delta^2)$ . Because of the reduced absorption, if  $\delta$  is large enough, the atoms are not heated and can remain in their cold state, either in the MOT or even as a BEC. This is desirable for better understanding the dynamics of cold atom systems [6].

The phase shift induced by the atoms causes interference in the images of the atoms if steps are taken to expose it. This is typically done using dark field or phase contrast imaging as described in [43]. These methods use a screen at the Fourier plane of the imaging system with a spot at the center to either block the undisturbed or constant portions of the plane wave or give it a phase shift to interfere with the scattered light. The intensity of such an image is given by

$$I = I_0(1 + t^2 + \tau^2 + 2t\tau \cos(\phi - \gamma) - 2t \cos \phi - 2\tau \cos \gamma), \quad (61)$$

where the properties of the spot on the screen at the Fourier plane are determined by  $\gamma$  the phase shift, and  $\tau^2$  the transmission. For dark field imaging,  $\tau = 0$ , and for phase contrast,  $\tau = 1$  and  $\gamma = \pm\frac{\pi}{2}$  [43].

There are a few other ways to extract the 2D number density utilizing the phase shift  $\phi$ , notably the diffraction pattern from cold atoms used in diffraction contrast imaging [70] which is closely related to off-resonance contrast imaging [71]. This method assumes a probe laser is propagated through the atom cloud and then diffracts in free space on the other side and does not need a phase screen at the Fourier plane and can even avoid using imaging optics at all. The resulting intensity diffraction pattern can be used to determine the column density and even distance from the sensor to the cloud.

### 5.2.1 Off-Resonance Imaging with the Light Field Microscope.

Each case of off-resonance imaging uses the scalar wave right after the atoms given by Equation (56), and in most cases, extracting the phase shift of the light caused by the atoms requires interfering the wave with itself in some way. Imaging this wave is interesting in the light field microscope case when considering only 2D information.

Up to the MLA, the optical system of the LFM acts straight forwardly as a microscope. The objective system simply images the plane wave to the MLA. It will magnify the wave and convolve it with the point spread function. If the PSF is sufficiently close to a Dirac Delta function, then only the magnification needs to be taken into account. Then the MLA can be thought of as a Shack-Hartmann sensor with the imaged plane wave hitting it; the Shack-Hartmann sensor measures the phase gradient across the wave [56]. The phase gradient is measured straightforwardly at the pixel plane as the Fourier transform of the portion of the wave hitting a given micro lens. Because the micro lenses are small, the wave hitting a given micro lens

can be assumed to have primarily a linear slope across it. The Fourier transform of a linear phase shift (or constant slope) is

$$\mathcal{F} \{ \exp(i2\pi(ax + by)) \} = \delta(f_x - a)\delta(f_y - b)$$

where  $\delta$  is the Dirac Delta function and  $f_i$  are the spatial frequencies, related to physical positions by  $f_i = \frac{i}{\lambda f_{\text{ml}}}$ . Considering just one dimension the minimal spatial frequency that can be detected is when the physical shift matches that of the spot size of the LFM, that is  $x = R_{\text{obj}}$ . Then

$$a_{\text{min}} = \frac{R_{\text{obj}}}{\lambda f_{\text{ml}}}$$

and similarly for  $b$ .  $a$  and  $b$  are related to the slope of  $\phi$  by,

$$\frac{d\phi}{dx} = 2\pi a \quad \frac{d\phi}{dy} = 2\pi b.$$

The LFMs designed for imaging large volumes do not have very high angular resolution, such as the NA= 0.26 system used in Section 4.1 or the NA= 0.7 system proposed in Section 4.7. In those cases,  $a_{\text{min}} \approx 55000/\text{m}$  and  $\approx 32000/\text{m}$ , respectively. For a high magnification situation, like the case where NA= 0.7 and  $\mathcal{M} = 80$  mentioned at the end of Section 4.7, the minimum slope is much smaller with  $a_{\text{min}} \approx 7500/\text{m}$ .

The density distribution of the atoms determines the slope of the phase shift on the scalar wave. No experimental images were taken to test this situation but the maximum phase slopes induced by the cloud can be found using a modeled atom cloud. A MOT cloud was modeled based on the distribution of a Gaussian as described in Section 2.2. The column density of a Gaussian cloud with  $10^8$  atoms and a FWHM

of  $\approx 0.6\text{mm}$  is plotted in Figure 35 along with the phase  $\phi$  induced by the atoms and the slope of the phase when the effect is maximized at  $\delta = 1$ . The maximum phase slope, marked with a red dot in the figure, is only  $\frac{2.61}{2\pi}/\text{m} = 0.415/\text{m}$ , so it would not be detectable by the LFM.

Here is where having a BEC could be an advantage as the density of the atoms is much higher and a much larger phase shift can be applied. The 2D density distribution of a BEC is given by

$$\tilde{n}_c(x, y) = \tilde{n}_0 \max \left( 1 - \frac{x^2}{L_x^2} - \frac{y^2}{L_y^2}, 0 \right)^{3/2}, \quad (62)$$

where  $\tilde{n}_0$  is the peak density of the distribution and  $L_{(x,y)}$  is the Thomas-Fermi length, further details can be found in Appendix B. If this is used to model the distribution, Figure 36 shows the distribution, phase shift and slope for a BEC with  $L_x = L_y = 30\mu\text{m}$  and a peak density of 100 atoms per  $\mu\text{m}^2$  or a total atom count of  $\approx 10^5$ . The peak slope is marked with the red dot and is a phase slope of  $\approx \frac{170000}{2\pi}/\text{m} \approx 27000/\text{m}$  at  $x = 21\mu\text{m}$ . However, this is in object space; the wave will hit the MLA in image space after having been magnified by the imaging system. Moving to image space modifies the slope by  $1/\mathcal{M}$ , for the  $\mathcal{M} = 80$  case the slope seen by the MLA would be  $\approx 340/\text{m}$  which is also too small to be detected.

The way to greatly increase the phase resolution of a plenoptic camera is to set it up for wave front-sensing, a plenoptic 3.0 system as discussed in Section 3.3. In this system, the angular information is now labeled by the micro lenses and the spatial information by the pixels behind each one. Along a single dimension, the spatial frequency resolution of the plenoptic 3.0 system is

$$a_{\min} = \frac{D_{\text{ml}}}{\lambda f_{\text{obj}}}.$$

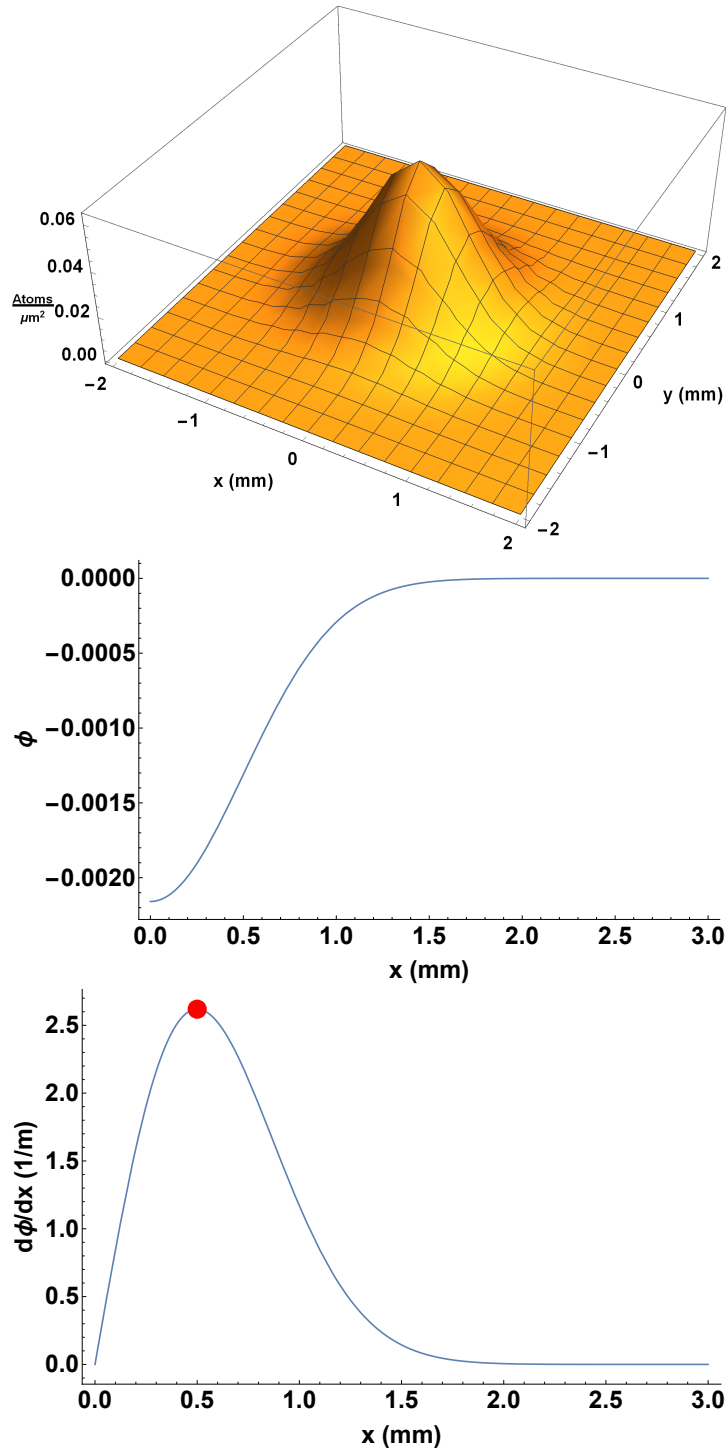


Figure 35. The top plot is the 2D density distribution of a 3D Gaussian atom cloud with  $10^8$  total atoms and a FWHM of 0.6mm. The middle plot shows the phase shift imparted to a plane wave passing through the atoms plotted as a function of the distance from the center of the cloud which is radially symmetric. The bottom plot is the slope of the phase, also radially symmetric. The peak slope is marked with the red dot and is a gradient of  $\frac{2.62}{2\pi}/\text{m} = 0.417/\text{m}$  at  $x = 0.5\text{mm}$ .

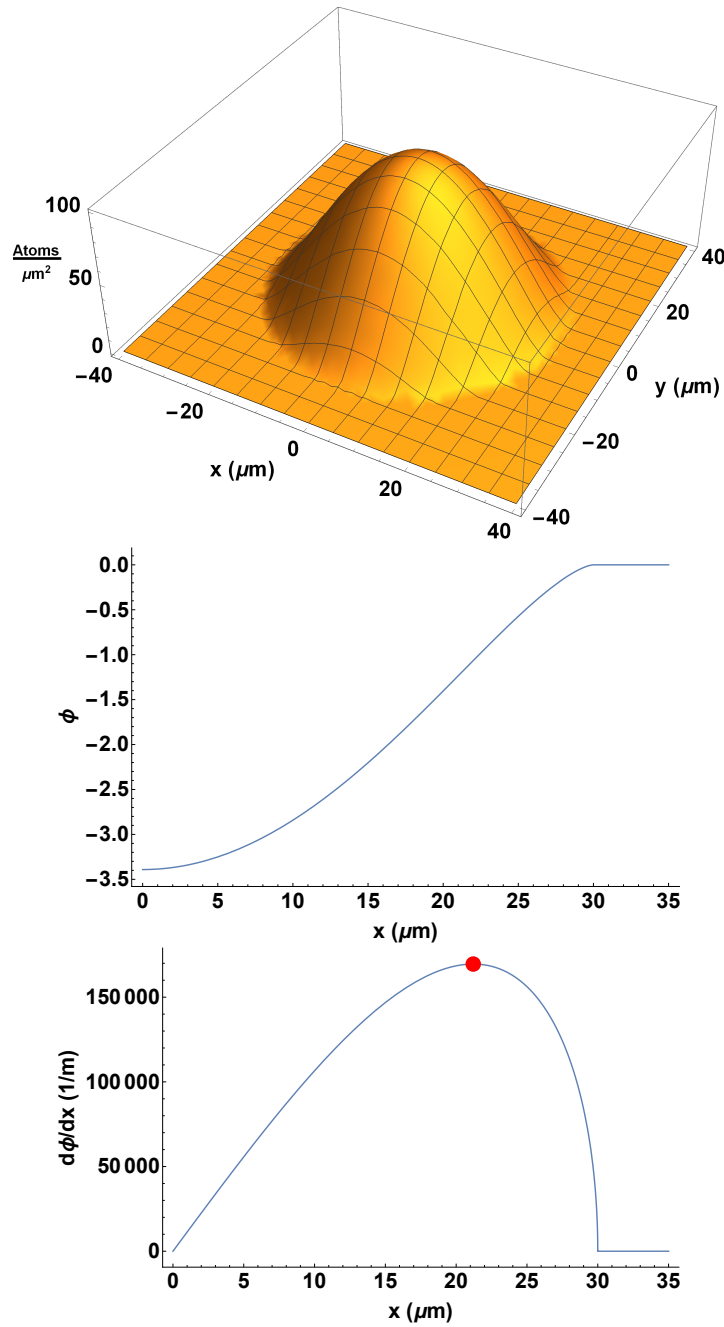


Figure 36. The top plot is the 2D density distribution of a BEC atom cloud with  $10^5$  total atoms and a Thomas-Fermi length of  $30\mu\text{m}$ . The middle plot shows the phase shift imparted to a plane wave passing through the atoms plotted as a function of the distance from the center of the cloud which is radially symmetric. The bottom plot is the slope of the phase, also radially symmetric. The peak slope is marked with the red dot and is a gradient of  $\approx \frac{170000}{2\pi}/\text{m} \approx 27000/\text{m}$  at  $x = 21\mu\text{m}$ .

If  $D_{\text{ml}} = 400\mu\text{m}$  and  $f_{\text{obj}} = 750\text{mm}$ , then  $a_{\text{min}} \approx 4300/\text{m}$ . This is fine enough to see the slope of the BEC phase shift, but now the resolution is only the number of resolvable spots behind a micro lens tiled across the pupil. For a reasonable size lens like a 2cm diameter objective there are only five resolvable spots behind a micro lens giving a spatial resolution of 4mm.

It is evident from this analysis that the trade-off of spatial resolution for angular resolution that a plenoptic system provides is not beneficial for standard plane-wave absorption or off-resonance imaging. In the case of absorption, the diffraction produced is too small to be measured. In the off-resonance case, the phase shift imparted to the wave is also too small even in the case of a high density BEC cloud of atoms. Strictly speaking, in the BEC cloud case, the phase shift is large enough to be observed but the resolution trade-off required to measure it is too significant.

### 5.3 Toward 3D Absorption Imaging

The reasons a LFM is not able to collect any more information from absorption images than a standard camera has just been outlined. Why does 3D imaging with the LFM work for fluorescence imaging? Each atom is radiating in all directions, so there is no limit on the angle a ray could have. The only limit is what angles can be collected by the objective as determined by the NA. In the case of absorption, most of the light is all going along the direction of the original incoming probe beam. This is by design but the diffraction and refraction that does occur is not enough to be measured given the trade-off of resolution in plenoptic systems.

However, if there were multiple plane waves, at a range of angles matching the NA of the imaging system, all propagating through the atoms at the same time, the MLA would separate them into their respective directions at the sensor. This multi-plane wave arrangement could be done with coherent light if an array of pin holes

were placed at the focal plane of an objective and illuminated from behind. The result would be a discrete series of plane waves at the Fourier plane. The problem is that because the waves are coherent, they would interfere with each other as they passed through the cloud. Atoms at locations where the wave experienced destructive interference would see no electro-magnetic field and not interact with the light. So they would be missed in any analysis of the beams after they had passed through the atoms.

If the waves were incoherent then simply the added intensities can be assumed to be passing through the atom cloud. In terms of extracting 3D information, it would be the equivalent to the fluorescing system. A set of pixels defining a perspective view would be the absorption image along that direction, just as the fluorescence image would be the light coming in from that direction. Figure 37 shows a comparison of a simulated absorption image of a very small spherically symmetric 3D Gaussian distribution and the standard analytical PSF for a fluorescing point source. The simulation was made by projecting waves at a discrete set of angles through the atoms using Equation (56). Each was individually propagated to the sensor and then the intensity calculated and summed with each of the others. The figure shows the division of  $I_0/I$  to show the removed intensity.

This means that with an incoherent source of light, the atoms can be imaged in 3D via absorption imaging techniques. Because the intensity of the light is directly measured by the camera, shot noise does not increase with the number of atoms in the cloud, making number calculations more accurate. However, to determine the total intensity of light passing through the atoms and the related fraction of scattered light, a calculation based on the area of the source and the distance to the atoms will be needed which can introduce the same errors as determining the solid angle of the objective in fluorescence imaging. However, the cone of light can more directly

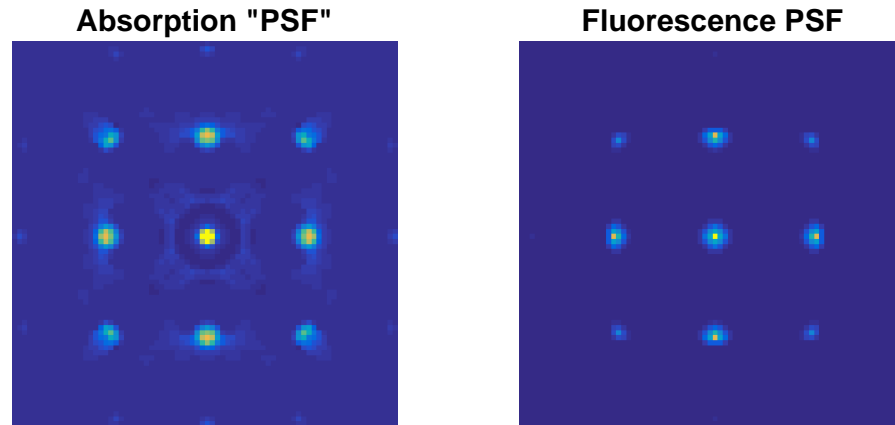


Figure 37. The simulated absorption “PSF” is shown on the left with the standard fluorescence PSF on the right. The absorption PSF was created by propagating a discrete set of plane waves through a small 3D Gaussian cloud of atoms that was behind the focal plane  $75\mu\text{m}$ . The intensity of each wave was added at the sensor. This was done again for a set where the cloud was removed and the left figure is the division of the intensity image  $I_0$  and the atom image  $I$ ,  $I_0/I$ . The fluorescence PSF is for a point source  $75\mu\text{m}$  behind the focal plane. The absorption “PSF” simulation does not start with an analytical solution for the objective PSF like the fluorescence PSF image is, and the division operation amplifies small differences in the simulated intensities, so there are some artifacts in the absorption simulation. Also the 3D Gaussian used to absorb the light has a finite size introducing some changes from an analytical point source.

be controlled to reduce this error. The end result is an absorption imaging system capable of 3D imaging of cold atoms. Finding the full benefits and trade offs of this method is a subject of further work.

## VI. Conclusion

Cold atom interferometers have demonstrated their ability to precisely measure accelerations and rotations which can in turn be used for creating inertial navigation systems (INS) [73, 17, 62]. The Air Force Research Laboratory Space Vehicles Directorate (AFRL/RV) is researching these systems because inertial navigation can be critical in times and places where GPS may be unavailable. In order for these INSs to be practical, the atom interferometers must function in dynamic environments and be small enough to fit on a mobile vehicle. The dynamic environment creates challenges when measuring the cold atom clouds, as the location of the clouds and the distribution of the clouds (which can contain the needed interference pattern) will be unknown. Additionally, making the systems smaller and mobile limits optical access to the cloud of atoms. The research that has been presented here is the first work done to find a solution to these two problems by using a plenoptic or light field imaging system which is capable of three-dimensional imaging with a single camera.

The goal of this research was to build and analyze a plenoptic imaging system capable of imaging a trapped cold atom cloud in 3D. A plenoptic or light field imaging system utilizes a micro lens array (MLA) at the focal plane of the objective imaging system to enable the recording of spatial and angular information about light rays hitting the MLA and propagating to the image sensor behind the array. This information can then be used to measure depth information about what was imaged by the camera. A light field microscope (LFM) was the plenoptic imaging system used here. The point spread function (PSF) of a LFM is depth-dependent because of the angular information made available from the MLA and sensor combination. Utilizing the depth-dependent PSF, a Richardson-Lucy deconvolution can be performed on LFM images to reconstruct the 3D volume imaged.

The first use of a low-magnification LFM to reconstruct a 3D volume containing cold atoms in a magneto-optical trap (MOT) was demonstrated in this work. Analysis of the low magnification optical system revealed that assumptions used in deriving the PSF no longer hold, introducing a phase term back into the PSF scalar wave equation which is typically dropped. The use of a Lytro© Development Kit MLA and sensor allowed for a simple cost-effective optical system while providing high resolution standard fluorescence images and still allowing for 3D reconstruction. Utilizing a long working distance objective, it was demonstrated that the reconstruction could be done from a range of about 30cm allowing observation of the atom cloud well inside a MOT. The use of a single camera is an important piece of this research because space around the atom traps becomes very limited as cold atom systems are made smaller and more portable.

The potential use of the LFM for absorption imaging was also explored as this method can be used to more accurately determine the number of atoms in a cloud. The imaging system was not able to extract the needed angular data in the standard coherent light absorption imaging cases. The spatial and angular resolution trade-off does not allow it. However, another method using an incoherent light source was shown to produce similar PSFs to that of the fluorescence imaging case. This method would allow for 3D image reconstruction with absorption-based images, allowing higher accuracy atom number calculations while also providing depth information.

## 6.1 Future Work

Accurately measuring the atom number and their distribution will be critical for applying LFMs to atom interferometers as it enables the inertial measurement. The number of atoms in each cloud and the distribution is the value needed to determine the inertial forces that acted on the atoms as they moved through the interferometer.

In the case of the 3D distribution, when the interferometer is on a dynamic system, the orientation of the cloud and the interference pattern will be unknown, using the 3D reconstruction demonstrated here enables the measurement on a practical system. A combination of improving the reconstructions along with determining the accuracy of atom number calculations will be important steps toward an atom interferometer application.

The 3D image resolution can be improved by increasing the NA of the LFM's objective. The trade offs associated with changing the NA were looked at in Section 4.7. Creating a system tailored to smaller cold atom clouds along with a custom MLA and sensor are important next steps. This can be combined with research looking at improving the 3D reconstructions using the data collected.

The 3D reconstructions were based on back projections (part of the Richardson-Lucy deconvolution) of the images taken by the LFM. The back projection reconstruction depends on the range of angles measured by the plenoptic system to determine the depth from which a given amount of light came. This range of angles is limited by the numerical aperture of the LFM objective. Back projection with a limited range of angles resulted in spreading of the reconstructed image along the optical axis, discussed in Section 4.3.1. The limited range of angles can fundamentally affect the resolution of the system which is discussed in detail by Crowther and Radermacher [20, 58]. But the axial spreading observed in this work is not caused by this fundamental limit but is an artifact of the reconstruction with limited angle information. There is a significant amount of work looking at this problem in other cases [32, 26] to try and reduce the reconstruction artifacts. One particular method for improving the reconstructions uses prior information [72]. Using the known physics of the MOT as a basis for the reconstruction could potentially improve the final 3D images, and applying such techniques is an excellent area for future work.

Experiments to determining the accuracy of atom number calculations can be performed in the near future using the fluorescence imaging technique shown here. There was a brief discussion of the steps needed for this in Section 4.8. The associated errors in the 3D atom number calculations need to be analyzed in light of how the reconstruction is done and how well it can be calibrated. Absorption imaging can reduce errors inherent in fluorescence imaging atom number calculations. Creating and testing such a system is an important candidate for further research, and is the next step after analyzing the fluorescence imaging atom number calculations. The absorption images should be able to improve on the atom number calculations once the 3D imaging capability has been shown.

Developing the capability to accurately measure atom number distributions can be useful in general. It can be used anywhere a 3D construction would be useful in a system where optical access is limited. In the case of a cold atom trap, it could be used to aid in determining trap shape, allowing for adjustment. Additionally, volumetric imaging could impact observation of three-dimensional arrays of atoms or ions in some quantum computing architectures, and thus the scalability of the qubits in those systems, by allowing concurrent observation of multiple planes of the array simultaneously [52].

The work done here is the first steps into creating a new way to image cold atoms. There is significant work to be done improving the system and demonstrating its capabilities for atom interferometry measurements. And there is a lot of exciting potential in creating a 3D imaging system for cold atom cloud applications.

## Appendix A. Tomography and Back Projection

Three dimensional (3D) imaging with a microscope and 3D imaging via tomography are mathematically equivalent as Levoy and others have pointed out [46, 67]. The connection is the reasoning behind using a basic back projection to determine the optical axis spreading of the reconstructions of the atom cloud as done in Chapter IV.

Tomography is performed by taking multiple 2D orthographic projections of a volume and using the Fourier slice theorem to form a reconstruction of the volume based purely on the 2D information collected. A orthographic projection or parallel projection is the 2D image created by integrating a volume along a single direction defined by a unit vector at the origin pointing in direction  $(\theta, \phi)$  in spherical coordinates, Figure 38 shows an example in 2D. The Fourier slice theorem says:

The 2D Fourier transform of the orthographic projection of an object  $f(x, y, z)$  obtained at angle  $(\theta, \phi)$  equals a 2D slice in the 3D Fourier transform of  $f$  where the normal vector to the 2D plane of the slice is at the same angle  $(\theta, \phi)$ .

This theorem can be reduced to two dimensions or expanded to higher dimensions. It enables sampling of the 3D Fourier space of an object from lower dimensional images and is what is done quite often in computed tomography (CT) scanners for imaging inside the human body [41]. Several projections through an object are created, either by collecting radiation from the object of interest (as in fluorescing atoms) or by shining a beam through it and measuring the absorption (as with x-rays for CT scans or absorption imaging of atoms). This gives a particular 2D slice in the 3D Fourier domain. By taking pictures at many angles through a full semi-sphere the full 3D Fourier transform is sampled. This set of data is then inverse Fourier transformed to recover a 3D reconstruction of the object.

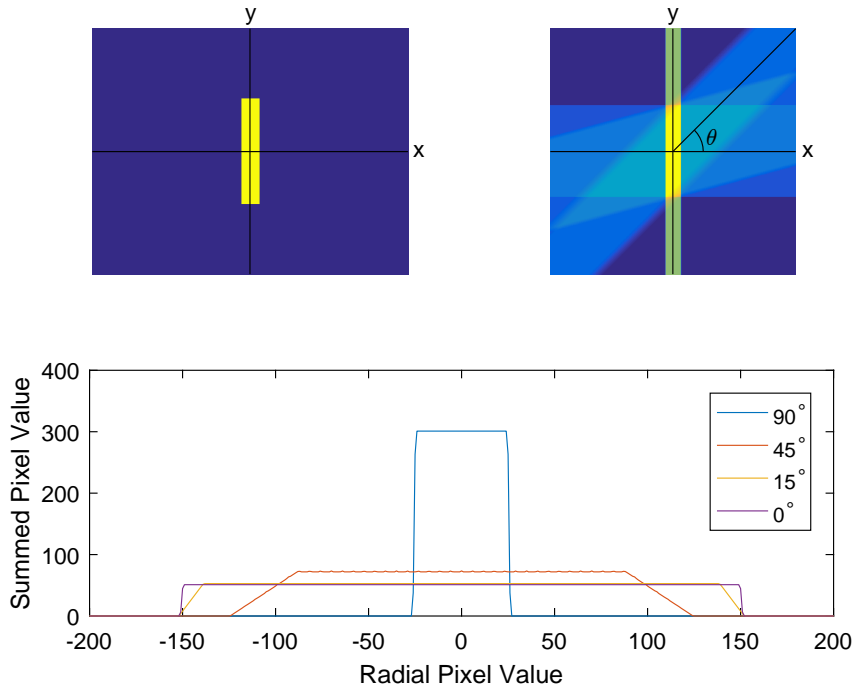


Figure 38. The top left image is a rectangle 300 pixels high and 50 pixels wide, each pixel has a magnitude of one and the rest of the image pixels are zero. The top right image shows the back projections of the orthographic projections shown in the bottom plot, at  $0^\circ$ ,  $15^\circ$ ,  $45^\circ$ , and  $90^\circ$ . The  $0^\circ$  projections shows the height and width of the rectangle in its width and magnitude because it is simply a sum of the pixel values along the  $x$ -axis, similarly for the  $90^\circ$  projection. The  $15^\circ$  and  $45^\circ$  degree projections show the mixed values of projecting at the respective angle to the rectangle.

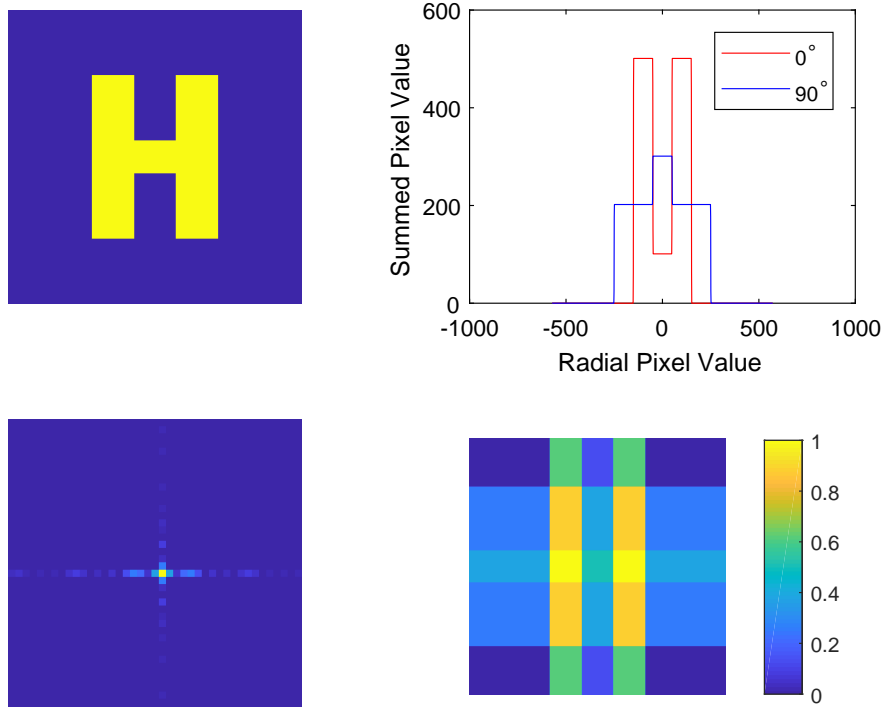


Figure 39. The back projections made from the Fourier transform of horizontal and vertical projections. The top left image is the 2D object being projected. The top right figure shows the 1D projections at  $0^\circ$ , and  $90^\circ$  plotted versus  $r$  the distance from the center of the image. The bottom left is the Fourier transforms of the two projections placed in a 2D matrix representing the approximation to the full 2D Fourier transform of the object. The bottom right is the 2D inverse Fourier transform of the bottom left image and is simply the 1D projections back projected over the 2D surface, the intensity scale has been normalized.

Using a single slice in the 3D Fourier space and inverse Fourier transforming is the same as performing a back projection of the orthographic projection corresponding to the slice, Figure 39 the process in 2D. The back projection simply takes the projected intensities and spreads them back over the volume to be reconstructed. A single plane in 3D Fourier space will be a Dirac Delta function along the plane's normal vector. The Delta function will simply be a constant along the direction of the normal vector when inverse transformed back to the volume. The magnitude of the constant will be determined by the inverse transformed 2D portion, resulting in the same pattern of the back projection filling the volume.

Recreating the volume purely using the Fourier transform introduces errors because of the discrete sampling, lack of views from every angle and the introduction of noise. Because of this iterative techniques are used instead [68]. Equation 43, the Richardson-Lucy deconvolution in Section 3.4.2, is such an iterative technique.

The point spread function (PSF) of an imaging system is describing the orthographic projection of a point source onto the sensor for all angles collected by the imaging system. It is the connection between the projected images and the volume being reconstructed in iterative techniques. In terms of the plenoptic imaging system the perspective views are the orthographic or parallel projections. The PSF is used to both back project the images into the volume and forward project the estimated volume to the sensor in order to iteratively build and test the volume reconstruction.

## Appendix B. Bose-Einstein Condensate Distributions

A Bose-Einstein Condensate (BEC) is typically created by taking atoms in a magneto-optical trap and putting them in a purely magnetic trap and then evaporatively cooling the atoms, and in some cases compressing the trap in order to reach the required density for the phase transition to a BEC. A good summary of BEC theory is given by Dalfovo [21] and Ketterle [43], from these a summary of the three-dimensional (3D) distribution of atoms in a BEC is given in the following.

The atoms are assumed to be in a magnetic trap with a harmonic potential given by

$$V(\mathbf{r}) = \frac{m}{2}(\omega_x^2 x^2 + \omega_y^2 y^2 + \omega_z^2 z^2) \quad (63)$$

where  $m$  is the mass of the atoms and the omegas are trap frequencies determined by the design of the trap. In this trap the atoms move in clouds with two different distributions, one for the atoms in the ground state, that is those actually part of the condensate, and another for those still in an excited state. The BEC atom distribution in the Thomas-Fermi limit is given by

$$n_c(x, y, z) = n_0 \left( 1 - \frac{x^2}{L_x^2} - \frac{y^2}{L_y^2} - \frac{z^2}{L_z^2} \right), \quad (64)$$

where  $n_0$  is the maximum density of ground state atoms at the center of the distribution and  $L_{(x,y,z)} = \sqrt{2\mu/m\omega_{x,y,z}^2}$  is the Thomas-Fermi length in their respective directions and  $\mu$  is the chemical potential of the gas. The thermal distribution is given by a Gaussian,

$$n_{th}(x, y, z) = n_t e^{-\left(\frac{x^2}{w_x^2} + \frac{y^2}{w_y^2} + \frac{z^2}{w_z^2}\right)}, \quad (65)$$

where  $n_t$  is the maximum density of the thermally distributed atoms and  $w_{(x,y,z)}$  are

the Gaussian widths given by

$$w_{x,y,z} = \frac{a_{ho}}{2} \left( \frac{k_B T}{\hbar \omega_{ho}} \right)^{1/2},$$

where  $a_{ho} = \sqrt{\hbar/(m\omega_{ho})}$  with  $\omega_{ho} = (\omega_x \omega_y \omega_z)^{1/3}$ ,  $k_B$  is Boltzmann's constant,  $T$  is temperature and  $\hbar$  is Plank's constant divided by  $2\pi$ .

When looking at absorption imaging of these clouds the 2D density distribution is seen by the light after passing through the cloud, integrating the density along the path of the light. If the light is traveling along the  $z$ -axis the thermal and condensate portions of the distribution become

$$\tilde{n}_c(x, y) = \tilde{n}_0 \max \left( \left( 1 - \frac{x^2}{L_x^2} - \frac{y^2}{L_y^2}, 0 \right) \right)^{3/2} \quad (66)$$

$$\tilde{n}_{th}(x, y) = \tilde{n}_t e^{-\left( \frac{x^2}{w_x^2} + \frac{y^2}{w_y^2} \right)} \quad (67)$$

where  $\tilde{n}_c$  and  $\tilde{n}_t$  are now the peak 2D densities.

## Appendix C. MOT Image Collection

Here is presented the images discussed in Chapter IV for each of the three MOTs. The plenoptic image, a contour plot, and the projected reconstruction with the reference image are shown.

### 3.1 MOT One

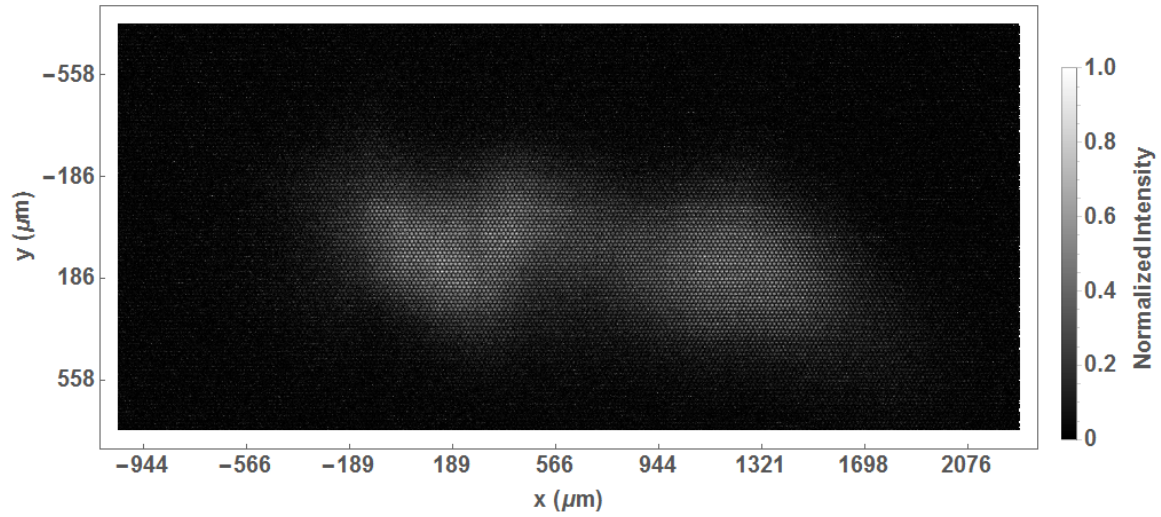


Figure 40. The raw plenoptic camera data after cropping and the background has been subtracted for MOT One.

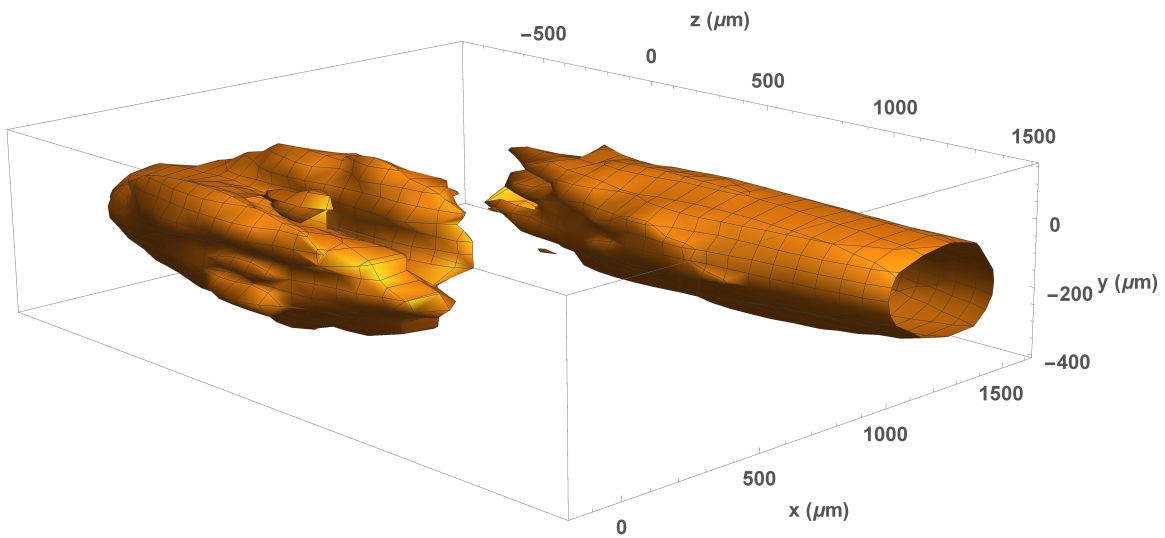


Figure 41. A contour surface through the normalized deconvolved volume produced from the plenoptic data in Figure 40.

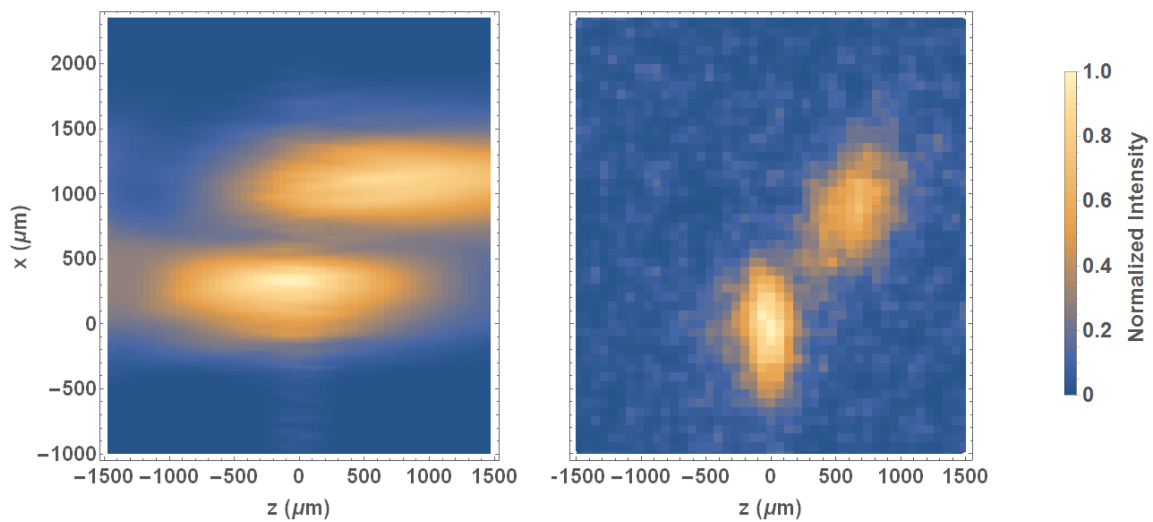


Figure 42. The projected image and the reference image for MOT One. Both have been scaled and plotted over the same range for comparison. Translation shifts have not been removed.

### 3.2 MOT Two

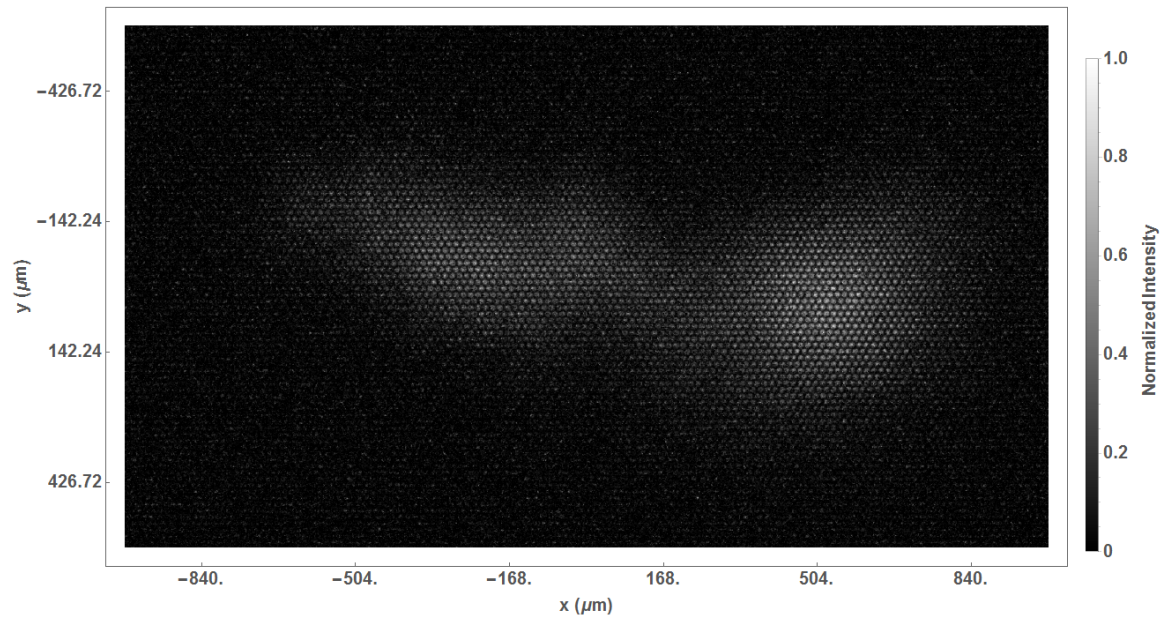


Figure 43. This is the raw plenoptic camera data after cropping and the background has been subtracted.

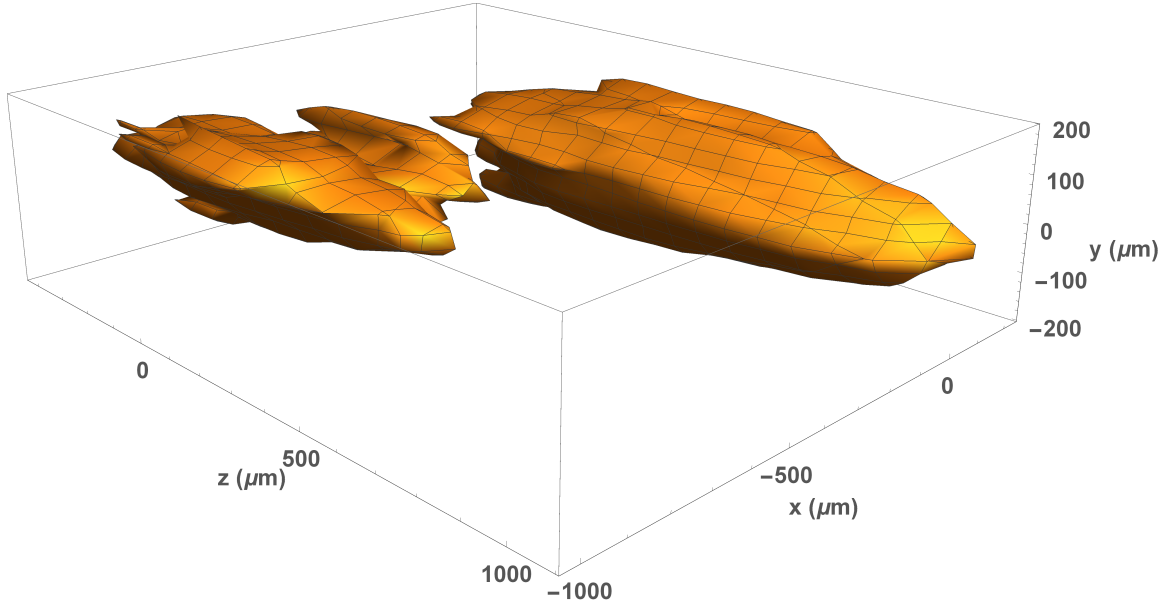


Figure 44. A contour surface through the normalized deconvolved volume produced from the plenoptic data in Figure 43.

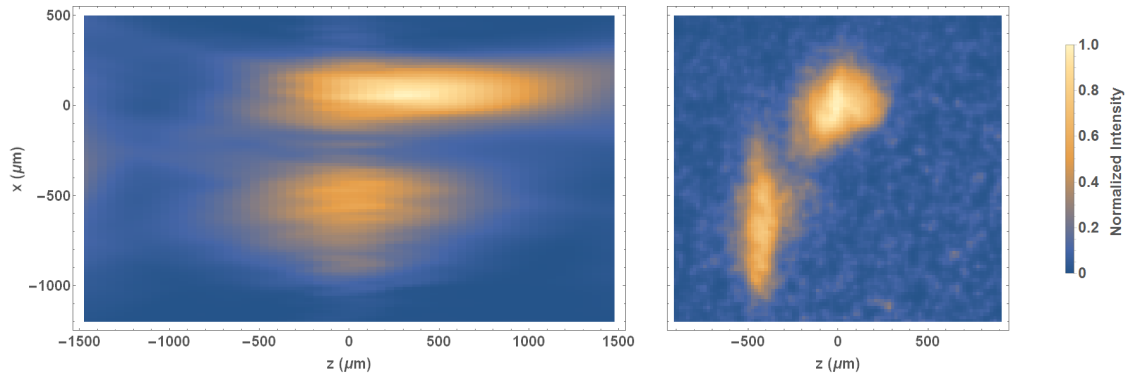


Figure 45. The projected image and the reference image for MOT Two. Both have been scaled and plotted over the same range for comparison. Translation shifts have not been removed.

### 3.3 MOT Three

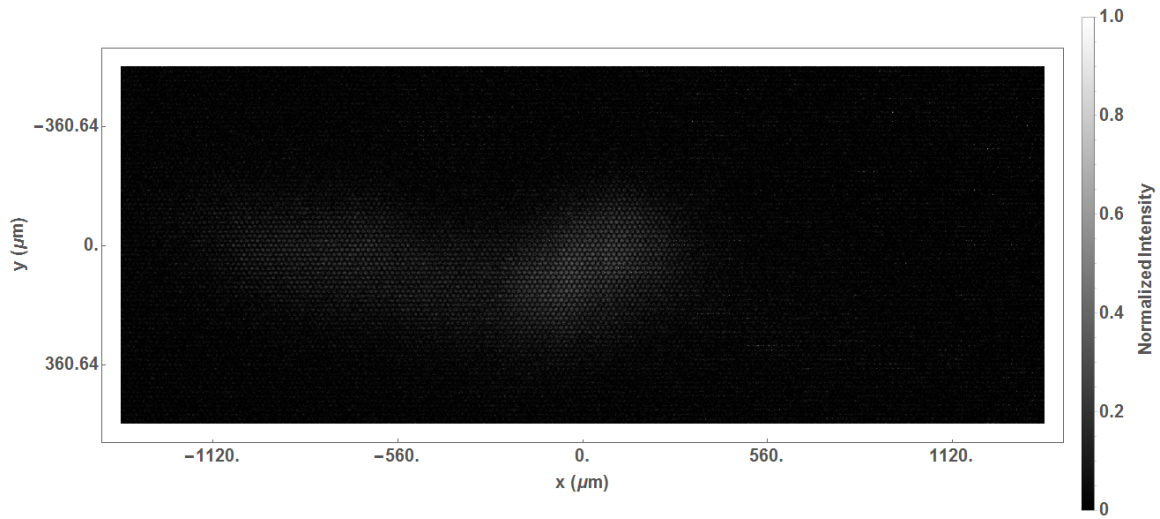


Figure 46. This is the raw plenoptic camera data after cropping and the background has been subtracted.

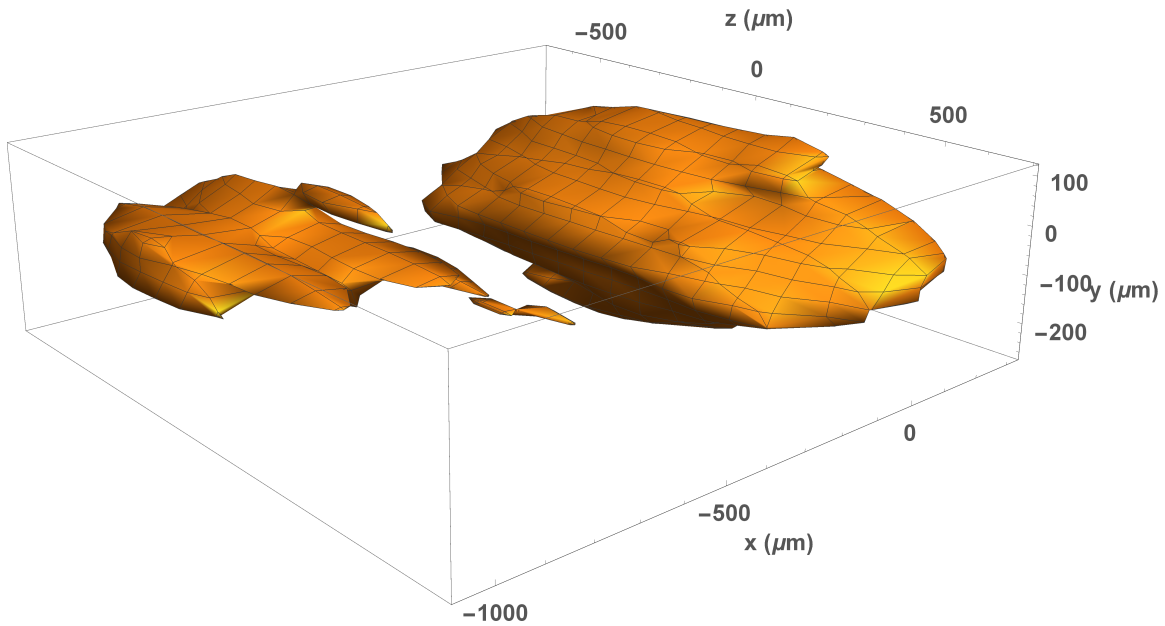


Figure 47. A contour surface through the normalized deconvolved volume produced from the plenoptic data in Figure 46.

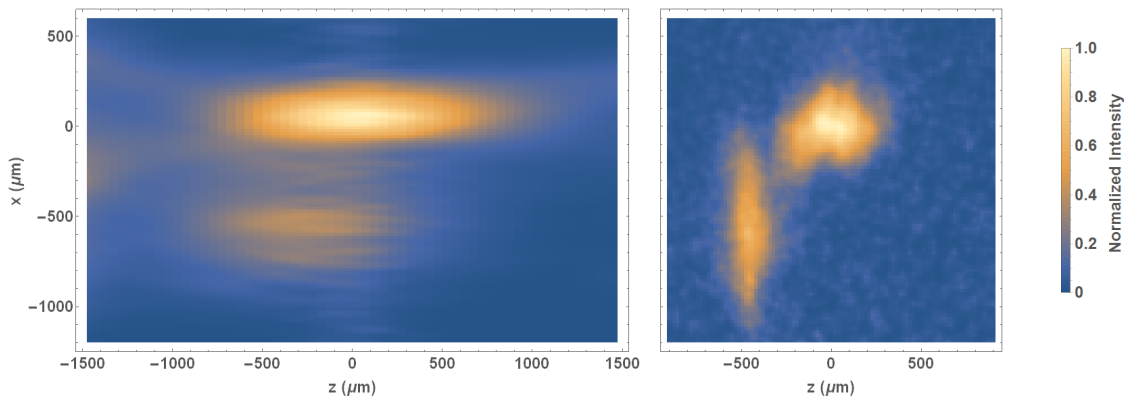


Figure 48. The projected image and the reference image for MOT Three. Both have been scaled and plotted over the same range for comparison. Translation shifts have not been removed.

## Bibliography

1. Adams, Charles S. “Atom optics”. *Contemporary Physics*, 35(1):1–19, 1994.
2. Adelson, Edward H and James R Bergen. “The plenoptic function and the elements of early vision”. *Vision and Modeling Group, Media Laboratory, Massachusetts Institute of Technology*, 1991.
3. Adelson, Edward H and John Y. A. Wang. “Single lens stereo with a plenoptic camera”. *IEEE Transactions on Pattern Analysis & Machine Intelligence*, (2):99–106, 1992.
4. Agard, David A, Yasushi Hiraoka, Peter Shaw, and John W Sedat. “Fluorescence microscopy in three dimensions”. *Methods in cell biology*, 30:353–377, 1989.
5. Anderson, Mike H, Jason R Ensher, Michael R Matthews, Carl E Wieman, and Eric A Cornell. “Observation of Bose-Einstein condensation in a dilute atomic vapor”. *science*, 269(5221):198–201, 1995.
6. Andrews, MR, M-O Mewes, NJ Van Druten, DS Durfee, DM Kurn, and W Ketterle. “Direct, nondestructive observation of a Bose condensate”. *Science*, 273(5271):84–87, 1996.
7. Barrett, B, PA Gominet, E Cantin, L Antoni-Micollier, A Bertoldi, B Battelier, P Bouyer, J Lautier, and A Landragin. “Proceedings of the International School of Physics Enrico Fermi, Course 188 Atom Interferometry,”. 2014.
8. Bayer, Bryce E. “Color imaging array”, July 20 1976. US Patent 3,971,065.
9. Bishop, Tom E and Paolo Favaro. “Plenoptic depth estimation from multiple aliased views”. *Computer Vision Workshops (ICCV Workshops), 2009 IEEE 12th International Conference on*, 1622–1629. IEEE, 2009.
10. Bishop, Tom E and Paolo Favaro. “The light field camera: Extended depth of field, aliasing, and superresolution”. *Pattern Analysis and Machine Intelligence, IEEE Transactions on*, 34(5):972–986, 2012.
11. Bishop, Tom E, Sara Zanetti, and Paolo Favaro. “Light field superresolution”. *Computational Photography (ICCP), 2009 IEEE International Conference on*, 1–9. IEEE, 2009.
12. Born, Max and Emil Wolf. *Principles of optics: electromagnetic theory of propagation, interference and diffraction of light*. Elsevier, 2013.
13. Bradski, Gary et al. “The opencv library”. *Doctor Dobbs Journal*, 25(11):120–126, 2000.

14. Broxton, Michael, Logan Grosenick, Samuel Yang, Noy Cohen, Aaron Andalman, Karl Deisseroth, and Marc Levoy. “Wave optics theory and 3-D deconvolution for the light field microscope”. *Optics express*, 21(21):25418–25439, 2013.
15. Burke, JHT, B Deissler, KJ Hughes, and CA Sackett. “Confinement effects in a guided-wave atom interferometer with millimeter-scale arm separation”. *Physical Review A*, 78(2):023619, 2008.
16. Burke, John Hughson. *Improvements and Applications of a Guided-Wave Bose Einstein Condensate Interferometer*. Ph.D. thesis, University of Virginia, 2010.
17. Canuel, B, F Leduc, D Holleville, A Gauguet, A Viridis, A Clairon, N Dimarcq, Ch J Borde, A Landragin, and P Bouyer. “Six-axis inertial sensor using cold-atom interferometry”. *Physical review letters*, 97(1):010402, 2006.
18. Cohen, Noy, Samuel Yang, Aaron Andalman, Michael Broxton, Logan Grosenick, Karl Deisseroth, Mark Horowitz, and Marc Levoy. “Enhancing the performance of the light field microscope using wavefront coding”. *Optics express*, 22(20):24817–24839, 2014.
19. Cronin, Alexander D, Jörg Schmiedmayer, and David E Pritchard. “Optics and interferometry with atoms and molecules”. *Reviews of Modern Physics*, 81(3):1051, 2009.
20. Crowther, RA, DJ DeRosier, and A Klug. “The reconstruction of a three-dimensional structure from projections and its application to electron microscopy”. *Proceedings of the Royal Society of London A: Mathematical, Physical and Engineering Sciences*, volume 317, 319–340. The Royal Society, 1970.
21. Dalfovo, Franco, Stefano Giorgini, Lev P Pitaevskii, and Sandro Stringari. “Theory of Bose-Einstein condensation in trapped gases”. *Reviews of Modern Physics*, 71(3):463, 1999.
22. Dansereau, Donald G. “Light Field Toolbox v0.4”. *MathWorks® File Exchange*. MathWorks® 2015.
23. Dansereau, Donald G, Oscar Pizarro, and Stefan B Williams. “Decoding, calibration and rectification for lenselet-based plenoptic cameras”. *Proceedings of the IEEE conference on computer vision and pattern recognition*, 1027–1034. 2013.
24. Davis, Kendall B, M-O Mewes, Michael R Andrews, NJ Van Druten, DS Durfee, DM Kurn, and Wolfgang Ketterle. “Bose-Einstein condensation in a gas of sodium atoms”. *Physical review letters*, 75(22):3969, 1995.
25. De Broglie, Louis. *Recherches sur la théorie des quanta*. Ph.D. thesis, Migration-université en cours d’affectation, 1924.

26. De Villiers, Mattieu. *Limited angle tomography*. Ph.D. thesis, University of Cape Town, 2004.
27. Deans, Stanley R. *The Radon transform and some of its applications*. Courier Corporation, 2007.
28. Dereniak, E.L. and Glenn D Boreman. *Infrared detectors and systems*. Wiley-Interscience, 1996.
29. Dickerson, Susannah M, Jason M Hogan, Alex Sugarbaker, David MS Johnson, and Mark A Kasevich. “Multiaxis inertial sensing with long-time point source atom interferometry”. *Physical review letters*, 111(8):083001, 2013.
30. Einstein, A and Quantentheorie des einatomigen idealen Gases. “Zweite Abhandlung”. *Sitzber. Kgl. Preuss. Akad. Wiss*, 3, 1925.
31. Eslami, Mohammed, Chensheng Wu, John Rzasa, and Christopher C Davis. “Using a plenoptic camera to measure distortions in wavefronts affected by atmospheric turbulence”. *SPIE Optical Engineering+ Applications*, 85170S–85170S, 2012.
32. Frikel, Jürgen and Eric Todd Quinto. “Characterization and reduction of artifacts in limited angle tomography”. *Inverse Problems*, 29(12):125007, 2013.
33. Georgiev, Todor and Andrew Lumsdaine. “Depth of field in plenoptic cameras”. *Proc. Eurographics*, volume 2009. 2009.
34. Georgiev, Todor, Zhan Yu, Andrew Lumsdaine, and Sergio Goma. “Lytro camera technology: theory, algorithms, performance analysis”. *IS&T/SPIE Electronic Imaging*, 86671J–86671J. International Society for Optics and Photonics, 2013.
35. Gershun, Andreĭ. “The light field”. *Journal of Mathematics and Physics*, 18(1):51–151, 1939.
36. Goodman, Joseph W. *Introduction to Fourier optics*. Roberts and Company Publishers, 2005.
37. Gu, Min. *Advanced optical imaging theory*, volume 75. Springer Science & Business Media, 2000.
38. Hänsel, Wolfgang, Peter Hommelhoff, TW Hänsch, and Jakob Reichel. “Bose–Einstein condensation on a microelectronic chip”. *Nature*, 413(6855):498–501, 2001.
39. Heavner, Thomas P, Elizabeth A Donley, Filippo Levi, Giovanni Costanzo, Thomas E Parker, Jon H Shirley, Neil Ashby, Stephan Barlow, and SR Jefferts. “First accuracy evaluation of NIST-F2”. *Metrologia*, 51(3):174, 2014.

40. Hecht, Eugene. “Optics, 4th”. *International edition, Addison-Wesley, San Francisco*, 3, 2002.
41. Hsieh, Jiang. *Computed tomography: principles, design, artifacts, and recent advances*, volume 114. SPIE press, 2003.
42. Kasch, Brian L. Personal communication. AFRL/RVBY.
43. Ketterle, W, DS Durfee, and DM Stamper-Kurn. “Making, probing and understanding Bose-Einstein condensates”. *arXiv preprint cond-mat/9904034*, 5, 1999.
44. Kowalski, Krzysztof, V Cao Long, K Dinh Xuan, M Głódź, B Nguyen Huy, and J Szonert. “Magneto-optical trap: fundamentals and realization”. *Comput. Meth. Sci. Technol. Special*, (115):129, 2010.
45. Levoy, Marc and Pat Hanrahan. “Light field rendering”. *Proceedings of the 23rd annual conference on Computer graphics and interactive techniques*, 31–42. ACM, 1996.
46. Levoy, Marc, Ren Ng, Andrew Adams, Matthew Footer, and Mark Horowitz. “Light field microscopy”. *ACM Transactions on Graphics (TOG)*, 25(3):924–934, 2006.
47. Levoy, Marc, Zhengyun Zhang, and Ian McDowall. “Recording and controlling the 4D light field in a microscope using microlens arrays”. *Journal of microscopy*, 235(2):144–162, 2009.
48. Lippmann, Gabriel. “Epreuves reversibles donnant la sensation du relief”. *J. Phys. Theor. Appl.*, 7(1):821–825, 1908.
49. Lott, Gordon E., Michael A. Marciniak, and John H. Burke. “Three Dimensional Imaging of Trapped Cold Atoms with a Light Field Microscope”. *Applied Optics*, 2017. Submitted.
50. Lumsdaine, Andrew and Todor Georgiev. “The focused plenoptic camera”. *Computational Photography (ICCP), 2009 IEEE International Conference on*, 1–8. IEEE, 2009.
51. Mignard-Debise, Lois and Ivo Ihrke. “Light-field microscopy with a consumer light-field camera”. *3D Vision (3DV), 2015 International Conference on*, 335–343. IEEE, 2015.
52. Nelson, Karl D, Xiao Li, and David S Weiss. “Imaging single atoms in a three-dimensional array”. *Nature Physics*, 3(8):556–560, 2007.
53. Ng, Ren. “Digital light field photography”. 2006.

54. Ng, Ren, Marc Levoy, Mathieu Brédif, Gene Duval, Mark Horowitz, and Pat Hanrahan. “Light field photography with a hand-held plenoptic camera”. *Computer Science Technical Report CSTR*, 2(11), 2005.
55. Phillips, William D. “Laser cooling and trapping of neutral atoms”. *Rev. Mod. Phys.*, 70(3):721, 1998.
56. Platt, Ben C and Roland Shack. “History and principles of Shack-Hartmann wavefront sensing”. *Journal of Refractive Surgery*, 17(5):S573–S577, 2001.
57. Raab, EL, M Prentiss, Alex Cable, Steven Chu, and David E Pritchard. “Trapping of neutral sodium atoms with radiation pressure”. *Physical Review Letters*, 59(23):2631, 1987.
58. Radermacher, Michael. “Three-dimensional reconstruction of single particles from random and nonrandom tilt series”. *Microscopy Research and Technique*, 9(4):359–394, 1988.
59. Raynor, Robert and Karl Walli. “Plenoptic camera range finding”. *Applied Imagery Pattern Recognition Workshop: Sensing for Control and Augmentation, 2013 IEEE (AIPR)*, 1–11. IEEE, 2013.
60. Raynor, Robert A. “Range Finding with a Plenoptic Camera”. *AIR FORCE INSTITUTE OF TECHNOLOGY WRIGHT-PATTERSON AFB OH GRADUATE SCHOOL OF ENGINEERING AND MANAGEMENT*, 2014.
61. Reeves, Jessica Mary. *An Atom Waveguide for Interferometry with a Bose-Einstein Condensate of 87Rb*. 2006.
62. Rushton, JA, Matthew Aldous, and MD Himsworth. “Contributed review: the feasibility of a fully miniaturized magneto-optical trap for portable ultracold quantum technology”. *Review of Scientific Instruments*, 85(12):121501, 2014.
63. Sagnac, Georges. “L'éther lumineux démontré par l'effet du vent relatif d'éther dans un interféromètre en rotation uniforme”. *CR Acad. Sci.*, 157:708–710, 1913.
64. Sakmann, Kaspar and Mark Kasevich. “Single-shot three-dimensional imaging of dilute atomic clouds”. *Optics Letters*, 39(18):5317–5320, 2014.
65. Schechner, Yoav Y and Nahum Kiryati. “The optimal axial interval in estimating depth from defocus”. *Computer Vision, 1999. The Proceedings of the Seventh IEEE International Conference on*, volume 2, 843–848. IEEE, 1999.
66. Schuldt, Thilo, Christian Schubert, Markus Krutzik, Lluís Gesa Bote, Naceur Gaaloul, Jonas Hartwig, Holger Ahlers, Waldemar Herr, Katerine Posso-Trujillo, Jan Rudolph, et al. “Design of a dual species atom interferometer for space”. *Experimental Astronomy*, 39(2):167–206, 2015.

67. Streibl, N. “Depth transfer by an imaging system”. *Journal of Modern Optics*, 31(11):1233–1241, 1984.
68. Swedlow, Jason R, John W Sedat, and David A Agard. “Deconvolution in optical microscopy”. *Deconvolution of images and spectra*, 285:284–309, 1997.
69. Townsend, CG, NH Edwards, CJ Cooper, KP Zetie, CJ Foot, AM Steane, P Szriftgiser, H Perrin, and J Dalibard. “Phase-space density in the magneto-optical trap”. *Physical Review A*, 52(2):1423, 1995.
70. Turner, Lincoln D, KFEM Domen, and Robert E Scholten. “Diffraction-contrast imaging of cold atoms”. *Physical Review A*, 72(3):031403, 2005.
71. Turner, Lincoln D, Karl P Weber, David Paganin, and Robert E Scholten. “Off-resonant defocus-contrast imaging of cold atoms”. *Optics letters*, 29(3):232–234, 2004.
72. Venkatakrisnan, Singanallur V, Charles A Bouman, and Brendt Wohlberg. “Plug-and-play priors for model based reconstruction”. *Global Conference on Signal and Information Processing (GlobalSIP), 2013 IEEE*, 945–948. IEEE, 2013.
73. Wildermuth, S, S Hofferberth, I Lesanovsky, S Groth, P Krüger, J Schmiedmayer, and I Bar-Joseph. “Sensing electric and magnetic fields with Bose-Einstein condensates”. *Applied physics letters*, 88(26):264103, 2006.
74. Wu, Chensheng and Christopher C Davis. “Modified plenoptic camera for phase and amplitude wavefront sensing”. *SPIE Optical Engineering+ Applications*, 88740I–88740I, 2013.
75. Wu, Chensheng, Jonathan Ko, and Christopher C Davis. “Determining the phase and amplitude distortion of a wavefront using a plenoptic sensor”. *JOSA A*, 32(5):964–978, 2015.
76. Wu, Chensheng, Jonathan Ko, William Nelson, and Christopher C Davis. “Phase and amplitude wave front sensing and reconstruction with a modified plenoptic camera”. *SPIE Optical Engineering+ Applications*, 92240G–92240G, 2014.

**REPORT DOCUMENTATION PAGE**

*Form Approved  
OMB No. 0704-0188*

The public reporting burden for this collection of information is estimated to average 1 hour per response, including the time for reviewing instructions, searching existing data sources, gathering and maintaining the data needed, and completing and reviewing the collection of information. Send comments regarding this burden estimate or any other aspect of this collection of information, including suggestions for reducing the burden, to Department of Defense, Washington Headquarters Services, Directorate for Information Operations and Reports (0704-0188), 1215 Jefferson Davis Highway, Suite 1204, Arlington, VA 22202-4302. Respondents should be aware that notwithstanding any other provision of law, no person shall be subject to any penalty for failing to comply with a collection of information if it does not display a currently valid OMB control number.

**PLEASE DO NOT RETURN YOUR FORM TO THE ABOVE ADDRESS.**

1. REPORT DATE (DD-MM-YYYY)		2. REPORT TYPE		3. DATES COVERED (From - To)	
4. TITLE AND SUBTITLE				5a. CONTRACT NUMBER	
				5b. GRANT NUMBER	
				5c. PROGRAM ELEMENT NUMBER	
6. AUTHOR(S)				5d. PROJECT NUMBER	
				5e. TASK NUMBER	
				5f. WORK UNIT NUMBER	
7. PERFORMING ORGANIZATION NAME(S) AND ADDRESS(ES)				8. PERFORMING ORGANIZATION REPORT NUMBER	
9. SPONSORING/MONITORING AGENCY NAME(S) AND ADDRESS(ES)				10. SPONSOR/MONITOR'S ACRONYM(S)	
				11. SPONSOR/MONITOR'S REPORT NUMBER(S)	
12. DISTRIBUTION/AVAILABILITY STATEMENT					
13. SUPPLEMENTARY NOTES					
14. ABSTRACT					
15. SUBJECT TERMS					
16. SECURITY CLASSIFICATION OF:			17. LIMITATION OF ABSTRACT	18. NUMBER OF PAGES	19a. NAME OF RESPONSIBLE PERSON
a. REPORT	b. ABSTRACT	c. THIS PAGE			19b. TELEPHONE NUMBER (Include area code)